Engineering three-dimensional extended arrays of densely packed nano particles for optical metamaterials using microfluidIque evaporation

Antonio Iazzolino

THÈSE

PRÉSENTÉE A

L'UNIVERSITÉ BORDEAUX 1

ÉCOLE DOCTORALE DES SCIENCES à renseigner

Par Antonio, IAZZOLINO

POUR OBTENIR LE GRADE DE

DOCTEUR

SPÉCIALITÉ : physico-chemie de la matière condensée

Engineering three-dimensional extended arrays of densely packed nano particles for optical metamaterials using microfluidque evaporation

Mise en en forme de réseaux 3D de nanoparticules par voie microfuidique et applications aux métamatériaux dans le domaine du visible

Directeurs de recherche : Jacques Leng et Jean Baptiste Salmon

Soutenue le : 19/12/2013
avec la mention : très honorable
Devant la commission d'examen formée de :
Rapporteurs :
M. GIOCONDO
M. THEODOLY OLIVIER

Membres de la jurie :
Mme Zakri Cécile President de la jurie
M. Barois Philippe
M. Leng Jacques
M. Salmon Jean Baptiste

Contents

1 Microevaporation **9**

1.1 Principles of microevaporation 10
1.1.1 Pervaporation 10
1.1.2 Evaporation-induced pumping 12
1.1.3 Evaporation-induced concentration of solute 14
1.2 Ideal microevaporators 16
1.2.1 Solute transport 16
1.2.2 Asymptotic regime 17
1.2.3 Transient regime 18
1.3 From dilute solution/dispersion up to dense states 20
1.3.1 Exploration of phase diagrams 21
1.3.2 Nucleation and growth of colloidal crystals 23
1.4 Fabrication and calibration of a microevaporator 26
1.4.1 Fabrication of a microevaporator 26
1.4.2 The principle of calibration 29
1.4.3 Results of calibration 29
1.4.4 Role of the evaporation length L_0 30
1.4.5 Role of the external humidity 32
1.5 Geometries of microevaporators 32

2 On-chip microspectrocopy **35**

2.1 Absorption spectroscopy: some general information 36
2.1.1 Visible spectrometry 36
2.1.2 Spectrophotometer architecture 37
2.2 Microspectroscopy 40
2.2.1 Spectroscopy on a microscope 40
2.2.2 Details of the device 41
2.3 Examples 47
2.3.1 Beer-Lambert law on chip 47
2.3.2 On-chip spatio-temporal microspectroscopy 52

3 Role of colloidal stability in the growth of micromaterials **55**
3.1 Material and methods 56
3.1.1 Plasmonic NPs 56
3.1.2 Microfluidic evaporation combined with on-chip spectroscopy 58
3.2 Kinetics of concentration: observed phenomenology 58
3.2.1 Phenomenology from video microscopy 58
3.2.2 Phenomenology from local absorbance measurements 60
3.3 Quantitative analysis of the concentration and growth processes 63
3.3.1 Model of A. Merlin *et al.* 63
3.3.2 Comparison with our measurements 64
3.4 A simple model for precipitation versus growth 67
3.4.1 Assumptions of the model 68
3.4.2 Concentration dynamics and destabilization 69
3.4.3 Different regimes of destabilization 70
3.4.4 Stability chart 73
3.5 Qualitative analysis of the structure of the material 74

4 Microfluidic-induced growth and shape-up of three-dimensional extended arrays of densely packed nanoparticles **77**

5 Bulk optical metamaterials assembled by microfluidic evaporation **93**
5.1 Design of a chip for ellipsometry 93
5.2 Measurement of refractive index 94
5.3 Materials 95
5.4 Perspectives 96

6 Conclusion **103**

Mise en en forme de réseaux 3D de nanoparticules par voie microfluidique et applications aux métamatériaux dans le domaine du visible

October 1, 2013

1 Introduction

Les métamatériaux sont définis comme étant des matériaux artificiels présentant des propriétés exotiques qui modifient la propagation des ondes électromagnétiques. À la fin des années 90, Pendry *et al.* démontrèrent théoriquement qu'il est possible de générer de tels métamatériaux, grâce à des structures particulières au sein du matériau (le fameux "split-ring resonator"). Les métamatériaux sont donc structurés à une échelle inférieure à la longueur d'onde incidente, et décrits par une permittivité et une perméabilité effective. En 2000, Smith *et al.* fabriquèrent le premier métamatériau mais dans la gamme micro-onde. Les perspectives dans le domaine de l'optique (300–800 nm) sont très prometteuses, mais le transfert des technologies utilisées en micro-ondes rencontre des obstacles.

Un des défis dans le domaine émergent des métamatériaux est d'assembler à grande échelle des nanoparticules NPs (10-50 nm) en des super-réseaux présentant des propriétés collectives. Des nanostructures tridimensionnelles de matériaux nobles, ayant de fortes réponses plasmoniques, peuvent en effet générer des matériaux aux nouvelles propriétés optiques.

Cette thèse fait partie du projet européen METACHEM, dont le but est de fabriquer des métamatériaux dans le domaine de l'infrarouge et du visible, en se basant sur l'utilisation de la nanochimie et de l'assemblage de matériaux. Plus précisément, ce travail de thèse se situe à l'interface entre les groupes de chimie qui synthétisent des nanoparticules en dispersion, et les groupes de caractérisation optique des matériaux. Dans ce travail de thèse, nous utilisons une technique originale *la microévaporation* [1] basée sur les outils microfluidiques, afin de générer de façon contrôlée des assemblées 3D de nanoparticules (dimensions typiques 1 mm$\times$10 μm$\times$ 50 μm).

2 Chapitre 1: microévaporation

Dans ce chapitre, nous présentons en détail la technique de microévaporation, ainsi que les travaux précédents effectués au laboratoire. Brièvement, cette technique est basée sur l'évaporation du solvant d'une suspension/solution contenue dans un canal microfluidique. L'évaporation concentre ainsi les solutés non-volatils, qui peuvent ainsi former des états denses confinés dans le canal microfluidique. La microévaporation est un outil puissant permettant de former des états denses dans des canaux de géométries bien définies. Dans ce chapitre, je décris en détail le principe de fonctionnement de ces microévaporateurs, en mettant particulièrement en évidence comment les paramètres géométriques du dispositif (longueur, largeur et hauteur des canaux) permettent de contrôler le taux de concentration d'un soluté non-volatil dans ces canaux. Je présente ensuite en détail un modèle simple 1D permettant de calculer le champ de concentration d'un soluté dans le canal, et j'illustre les résolutions numériques de ce modèle par des approximations analytiques précédemment publiées [2]. Le cas de la transition vers un état dense est ensuité illustré à travers différents travaux précédemment effectués au LOF (électrolytes, polymères,...).

Le cas des suspensions colloïdales précédemment étudié [3] est particulièrement discuté, notamment les bilans de masse qui permettent de modéliser la croissance de cristaux colloïdaux dans les canaux d'évaporation.

3 Chapitre 2: micro-spectroscopie sur puce microfluidique

Dans ce chapitre est présenté une technique expérimentale permettant de mesurer directement sur une puce microfluidique des spectres d'absorbance $A(\lambda)$. Ce montage est basé sur l'utilisation d'un microscope inversé et d'un spectromètre fibré. Nous discutons dans ce chapitre de la résolution temporelle et spatiale du montage.

Sans faire de modifications au microscope (c'est-à-dire en utilisant le condenseur du microscope, correctement réglé), il est possible de faire des mesures très focalisées (taille du spot 6 μm) mais sur des échantillons peu absorbants ($A < 0.8$). En effet, des mesures spatiales résolues sur des mires calibrées permettent de montrer que le volume sondé par le spectromètre fibré est constitué à 95% d'un microspot, mais aussi à 5% d'un champ plus large ($\approx$ 140 μm). Dans le cas de matériaux absorbants ($A > 0.8$) localisés dans des canaux microfluidiques de largeurs $w < 140$ μm, la fraction de lumière non focalisée (i.e. provenant du champ large de 140 μm) n'intersecte pas le canal et est collectée par le spectromètre. Il en résulte une absorbance *effective* plus faible que celle du matériau réel.

Nous montrons aussi qu'à l'aide de *masques découpés* précisément ou en modifiant le champ d'illumination grâce à un *trou calibré* de petite taille, il est possible de limiter le champ d'illumination et ainsi de pouvoir réellement effectuer des mesures microfocalisées. Nous montrons aussi que ce dispositif, couplé à une caméra et à la platine motorisée du microscope, permet de *scanner* en temps et en espace, les spectres d'absorption dans un canal microfluidique. Nous utilisons ce dispositif afin de sonder le processus de concentration de

NPs plasmoniques dans un micro-évaporateur.

4 Chapitre 3: rôle de la stabilité colloïdale lors de la croissance de matériaux

Dans ce chapitre sont présentés les résultats de concentration/croissance de matériaux en microévaporateurs à partir de dispersions diluées de particules *core-shell* $Ag@SiO_2$ (diamètre total 100 nm, diamètre du cœur d'argent 20 nm). Ces particules présentent en dispersion diluée des propriétés plasmoniques (résonance plasmon à environ 400 nm) conférant une couleur jaune à la dispersion.

Nous montrons qu'en fonction de la concentration de la dispersion, nous sommes capables ou non de faire croître un état dense de ces nanoparticules dans le canal de microévaporation. A haute concentration (fraction volumique $> 0.2\%$), un état dense nuclée et croît le long du microévaporateur. Pour de très faibles concentrations ($< 0.005\%$), nous n'observons pas d'état dense, et les NPs semblent précipiter et s'accumuler à une distance finie (≈ 1 mm) du bout du microévaporateur. Dans les gammes de concentration intermédiaire, nous observons le scénario suivant: croissance d'un état dense à partir du bout du canal, puis arrêt de la croissance suivie de l'accumulation à ≈ 1 mm de NPs qui précipitent.

Ces mêmes résultats sont corroborés grâce aux montage précédemment décrit, par des mesures locales d'absorbance. Ce même montage permet par ailleurs de mesurer les champs de concentration dans le canal microfluidique (tout du moins pour les faibles absorbances), ce qui nous a permis de valider expérimentalement les modèles de croissance colloïdales en microévaporation [3]. Nous proposons aussi par ce même dispositif une façon originale de vérifier la loi de Beer-Lambert, en mesurant l'absorbance le long du canal microfluidique, dans la zone où la convection domine le transport des particules (rampe hyperbolique).

Les observations de précipitation vs. croissance sont expliquées par la présence d'impuretés ioniques dans la solution initiale qui se concentrent dans le canal, tout comme les NPs. En fonction du ratio de concentration NPs sur impuretés, la concentration locale en impuretés peut franchir un seuil de stabilité colloïdale avant la nucléation et la croissance du matériau dense de NPs, ce qui explique nos observations. Nous présentons aussi un modèle ultra-simplifié basé sur des équations non-couplées de concentration par micro-évaporation des NPs et des impuretés, pour prédire théoriquement des critères permettant de conclure si il est possible de fabriquer un micro-matériaux par cette technique. Brièvement, nous montrons que notre technique permet à coup sûr de faire croître une assemblée 3D de NPs, dès lors que la dispersion diluée est suffisament concentrée, suffisament stable, et contient peu d'impuretés.

5 Chapitre 4: mise en forme de réseaux 3D de nanoparticules

Dans ce chapitre, nous utilisons l'outil microévaporateur pour mettre en forme différents matériaux à partir de diverses dispersions de nanoparticules. Nous avons ainsi réalisé avec succès des matériaux à partir de dispersions de nanoparticules d'or (cœur - couronne Au@PEG, nano-bâtonnets), de mélange de NPs SiO_2 et *core-shell* $Au@SiO_2$, et même à partir de particules *framboises* $SiO_2@Ag@SiO_2$. Ces dernières sont très prometteuses en terme de propriétés optiques nouvelles, car des travaux récents montrent qu'elles peuvent induire un magnétisme artificiel dans le domaine du visible [4]. Dans ce chapitre, nous montrons aussi une technique simple pour s'affranchir des problèmes de stabilité colloïdale discutés dans le chapitre précédent. Brièvement, on fait croître dans le microévaporateur sur plusieurs millimètres, un état dense à partir d'une dispersion concentrée connue (par exemple des latex). On concentre ensuite dans le même canal les NPs diluées d'intérêt. L'état dense au bout du canal agit alors comme un filtre, dans lequel les impuretés moléculaires se concentrent, mais qui retient les NPs d'intérêt qui peuvent alors se concentrer jusqu'à former un état dense sans précipiter.

6 Chapitre 5: mesures ellipsométriques d'assemblée 3D mises en forme par microévaporation

Dans ce dernier chapitre, j'illustre une collaboration au sein du groupe METACHEM qui nous a permis d'effectuer des mesures optiques sur les matériaux assemblés par notre technique. En effet, nous avons montré par microscopie électronique à haute résolution que les états denses concentrés dans les canaux microfluidiques présentent des facettes *lisses* à l'échelle optique. De tels matériaux sont donc très adaptés à des mesures d'ellipsométrie fine permettant de remonter aux valeurs de permittivité et perméabilité effectives du matériau. Nous avons effectué differentes mesures sur des matériaux divers: cubes d'argent (30 nm), core-shell $Ag@SiO_2$ (diamètre du cœur 50 nm, écorce de silice 25 nm), cœur-couronne Au@PEG (15 nm), core-shell $Ag@SiO_2$ (diamètre du cœur 15 nm, écorce de silice 8 nm). Les matériaux les plus prometteurs sont ceux qui contiennent le plus de métal (en fraction volumique). Les analyses éllipsométriques montrent en effet qu'il y a un *red-shift* de la résonance plasmon par rapport à la dispersion diluée, et un indice de réfraction grand dans le proche infrarouge.

References

[1] J. Leng, B. Lonetti, P. Tabeling, M. Joanicot, and A. Ajdari. Microevaporators for kinetic exploration of phase diagrams. *Phys. Rev. Lett.*, 96:084503, 2006.

[2] J.-B. Salmon and J. Leng. Application of microevaporators to dynamic exploration of the phase diagram. *J. Appl. Phys.*, 107:084905, 2010.

[3] A. Merlin, J.-B. Salmon, and J. Leng. Microfluidic-assisted growth of colloidal crystals. *Soft Matter*, 8:3526, 2012.

[4] S. N. Sheikholeslami, H. Alaeian, A. L. Koh, and J. A. Dionne. A metafluid exhibiting strong optical magnetism. *Nano Lett.*, 13:4137, 2013.

Introduction

The field of functional materials made of nanoobjects or nanoparticles (NPs) is florishing at the moment for several reasons. First, the chemical synthesis of NPs has reached a high level of maturity and chemists can provide tailor particles with a fine degree of control regarding their shape, structure, and new properties emerge from these highly sophisticated NPs [1]: strong and permanent fluorescence of quantum dots, tunable plasmonic features of metallic NPs, high conductivity and mechanical strength of carbon nanotubes, selective sites of catalytic nanoclusters, etc. Importantly, these nanomaterials are often processed in a solution way which is a challenging but promising route for industrial upscaling. Eventually, the collective properties emerging from the assembly of these NPs sometimes bring unprecedented features that are neither present at the nanoscale nor for natural materials. Here, we investigate how to produce materials made of NPs for a specific application, optical metamaterials.

Metamaterials are defined as engineered materials having exotic properties that alter the behavior of waves, and we will talk exclusively of electro-magnetic (EM) waves in the range of visible light although the concept applies equally to pressure waves (acoustics), heat propagation (thermodynamics), surface waves (hydrodynamics), shear waves (mechanics), etc. Metamaterials have been theoretically described first by Veselago in 1968 [2] where he postulated that a negative refractive index of light could well be possible assuming that both the permeability (μ) and the permittivity (ϵ) of the material are negative. In 1999-2000, Sir Pendry extended Veselago's idea [3,4], making it more formal and introducing the idea of perfect lens, a revolution for sub-wavelength imaging. He also introduced a structure (the split-ring resonator) that permits us to tune μ, and in 2000, the first material with a negative refractive index in the microwave range was fabricated [5] following his ideas. Such an artificial material incorporates in fact two components: a metallic wire serving as an antenna and providing a negative ϵ and a split-ring resonator which acts as an inductor and leads to a negative μ. The micro-structures have a dimension of order of a millimeter, much smaller than the wave-length of the microwave field ($\approx$ cm) so that the material appears homogeneous for the wave and is treated in the frame of effective media. The key innovation was here to introduce two components that tune independently the properties of the medium (ϵ and μ). These two structuring elements were fabricated by hand or with lost-cost procedures used for making printed-boards, placed on a dieletric supporting frame with a periodic arrangement; when 'shinning' the material with a microwave field, the 'light' did bend in the opposite direction as it would do for a standard material, thus

evidencing the negative refraction.

Such an approach opened the route to metamaterials and since then, scientists and engineers have worked at making the structures ever smaller, using lithography for instance, so that metamaterials that work near the visible region have been produced. However, for making an effective medium working in the visible range, the size a of the resonating feature should be much smaller than the wave length of light λ, thus $\lambda/a \gg 1$ imposes features in the range $a \approx 30 - 70\,\mathrm{nm}$. It is the limit where lithography becomes difficult. Also, materials produced using lithography are essentially two-dimensional. There is thus a challenge for making bulk (three-dimensional) materials with nanoscaled features.

The present work lies in this context, making bulk materials with engineered NPs, and is a small part of a large european consortium (METACHEM) funded in the FP7 program between 2009 and 2013 and coordinated by Dr Philippe Barois (CRPP, France). The goal of this project is to design, produce, and characterize metamaterials working in the visible range and which are produced using a *bottom-up approach*: nanoresonators (NPs) are produced in solution and assembled using physical-chemistry tools in order to create the desired material. The consortium gathers theorists than design the NPs to be assembled (Heslinki, Louvain, and Sienna groups), nanochemists that provide specific NPs (CRPP, ICMCB, Bari, Vigo groups), teams dedicated to the construction of materials (Collège de France, LOF, CRPP, Bari), and experts in optical characterization (Manchester, Cosenza). The materials considered in this project lie in 3 categories: i) planar structures obtained through molecular templates (so-called nano-fishnets) or by the Langmuir-Blodgett technique (1 to about 10 layers of NPs); ii) templated structures obtained with block copolymers; iii) bulk materials obtained with evaporation techniques, including microevaporation.

The resonators to be assembled are NPs with two main designs in order to control independently ϵ and μ. The control of ϵ should be provided by metallic NPs (gold or silver, in the size range $a = 10 - 100\,\mathrm{nm}$) that exhibit a localized surface plasmon resonance: the conduction electrons of the metal are excited by the electric field of light and oscillate, and a resonance occurs at a frequency that depends on the material, size, and environment of the NPs. At the resonance frequency, the NPs absorb light, which makes a solution of them look colored (red for gold, yellow for silver). When making a material out of these NPs, the refractive index ($n^2 = \epsilon\mu$) can be calculated thanks to theory of effective media (e.g., with Maxwell-Garnett theory) and is shown to fall below 0 just after the resonance frequency at high-enough concentration. The role of the order/disorder/cristallinity concerning the collective response of the materials is still under debate but several groups have shown that lattices of theses NPs should offer a precise control of ϵ. The control of μ is more complicated to achieve but Alù and Engheta [6] found a elegant way to do it: a circular array of plasmonic NPs forms a single sub-wavelength loop, in which a circulating displacement current due to the plasmonic resonance of the NPs generates the magnetic dipole moment, which eventually permits the control of μ. Later, Simovski and Tretyakov [7] calculated the ideal 3D structure that should display artificial magnetism excited with visible light: the so-called raspberry-like NP where a dielectric NP at the core is decorated on its surface with metallic NPs that can induce the current loop. Recently, experiments have demonstrated that solutions of these rapsberries exhibit a collective resonance which is likely

to be a magnetic response [8, 9]. Finally, if the raspeberry has a metallic core, it should combine the control of ϵ from the plasmon resonance of the core and the control of μ from the current loop. It is clear that making these NPs is certainely very difficult especially because strong constraints have been given as to their precise design (size of the core, number and spacing between satellites, etc.).

In the present work, I address exclusively the assembly of the nanoresonators, the latter being provided by partners of the METACHEM consortium and we use microevaporation in order to guide their self-assembly. Microevaporation is a microfluidic technique developped at LOF and which permits the concentration of solute in a nanoliter channel thanks to an extraction membrane. I will review in the first chapter of the thesis the main characteristics of the microfluidic device. In brief, a linear channel (height $\approx 10\,\mu$n, width $\approx 100\,\mu$m, length $\approx$mm–cm) is closed by one wall which is permeable to water only. By diffusion across this membrane, the water can escape and it induces a flow that refills the channel. The solute cannot escape and is driven by the flow to a place where it accumulates permanently: the concentration increases untill a dense phase nucleates and grows. This process has been used by A. Merlin for growing colloidal crystals and by J. Angly (also in the frame of METACHEM) for growing NP-based materials. Together with J. Angly, we developped a version of the microevaporator which is able to concentrate extremely dilute dispersions, as it is sometimes the case for dispersions of metallic NPs and the chapter 1 of the thesis shows how the microfluidic device must be designed for such a goal. In the second chapter of the thesis, I describe a new experimental setup I developped and which is based on microspectroscopy: we equipped a microscope with a UV-Vis spectrometer in order to measure directly in the microfluidic chip the extinction spectra during the concentration process of NPs. The corresponding chapter details the benefits and limits of the setup, in particuler the range of extinction we can measure and the spatial resolution of the microspectrometer (of order of a few microns in the best cases). Then, we make an intensive use of the setup to follow the concentration process of silica-coated silver NPs. Thanks to an automated stage to move the sample (the chip), and automated control of a camera together with the spectrometer, we collect large amount of data that combine video and spectroscopy. We evidence that the growth of NP-based materials is not always possible because sometimes, the NPs precipitate on the way to high concentration. We demonstrate it is due to the simultaneous concentration of ionic species and NPs that bring the dispersion close to colloidal stability. We build a simple model that accounts reasonably well for this two-specie concentration process and leads to a *stability chart* which tells when growth of a material is possible depending on the concentration ratio of salt and NPs present in the stock solution. Basically, when the dispersion is too dilute, it is not possible to concentrate the NPs because even impurities are sufficient to increase the ionic strength close to the colloidal stability limit. Yet, it also shows that it is possible to grow NP-based materials and we give a series of successfully built materials. We managed to grow dense arrays of NPs of several natures: core-shell NPs with either a gold or a silver core, core-corona NPs with either gold spherical cores of silver cubic cores, gold nanorods, and also mixtures of several types of NPs. In all these cases, we could extract the material and image it with SEM (highly resolution scaning electron microscopy), and we could also

perfom *in-situ* small-angle X-Ray scattering with a focused beam at ESRF and SOLEIL synchrotrons, in order to quantify the structure of the material. We found that the materials are made of dense arrays of NPs with a volume fraction of metal that varies between 5 and 40% depending on the nature of capping agent on the NPs. Importantly, the shape of the materials is given by that of the microfluidic channel in which they grew, meaning that the interfaces of the materials are very flat (roughness of order of the size of the NPs), thus with optical quality.

It turns out to be important for optical characterization: we performed it with A. Baron and K. Ehrhardt (CRPP) and also in collaboration with A. Grigorenko (Manchester) and in both cases, the technique used is microspot ellipsometry. We will describe it in the last chapter of the thesis with the constraints for making such measurements and the results that follow. The most interesting materials are the ones with a very high concentration of metal for which there is a red-shifted resonance as compared to the dispersion, and with a very high refraction index in the near-infrared region. Eventually, we also started to develop a new microfluidic technique, the microfiltration, for the case where NPs are not stable and permitted us to assemble the first generation of raspberry-like NPs into a dense material.

This work thus gives a contribution to the fabrication process of NP-based materials and demonstrates that the technique we use is not only relevant but also permits us to produce materials which are bulky (ratio thickness of sample over size of particles $\approx 10^2 - 10^3$) and for which we can perform a clear optical characterization.

Chapter 1

Microevaporation

Microfluidics is the branch of fluid mechanics dedicated to the study of flows in channels with dimensions between 1 micron and 100 microns. Channels can be fabricated using classical lithography techniques in various materials such as glass, silicon, or polydimethylsiloxane (PDMS). The latter material has a high permeability to water, and this property is the basics of functioning of "microevaporators" [10]. The object of this chapter is to illustrate the basic principles and possible applications of such microfluidic chips. In the first part of the chapter, we present a detailed description of the physics of microevaporators using analytical arguments, and we describe some applications. In the second part of the chapter, we present the experimental protocol of engineering of a microevaporator and different types of microfluidic devices.

1.1 Principles of microevaporation

1.1.1 Pervaporation

In the 90s, Favre *et al.* [11] and Watson *et al.* [12] studied the phenomenon of pervaporation of water through PDMS membranes. A decade later, Verneuil *et al.* [13] and Randall *et al.* [14]. studied the flow in a microfluidic channel molded in PDMS induced by the spontaneous pervaporation of water through the polymer matrix. Figure 1.1 shows a 3D view of a microfluidic channel molded in PDMS (typical dimensions length 1 cm, width 100 μm, height 10–30 μm). This channel is filled with water. PDMS is permeable to water, so there is a net flux J of water molecules leaving the microchannel, and diffusing into the PDMS matrix, up to the evaporation in air: this is the pervaporation process. From mass conservation, pervaporation induces a flow of water towards the end of the channel.

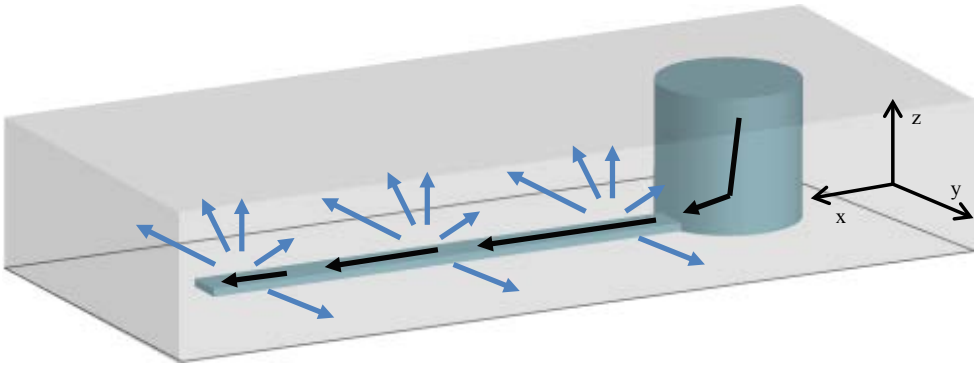

Figure 1.1: Basics of microevaporation: a microchannel filled with water in a PDMS matrix. Blue arrows indicate the pervaporation of water, and black arrows the corresponding flow.

Experimentally, Verneuil *et al.* followed the velocity of fluorescent beads in a channel with length of 1 cm, height 20 μm and a width ranging between 26 and 477 μm [13]. They showed that the flow velocity is linear along the channel, and it decreases when the channel width increases, see Fig. 1.2. Randall *et al.* studied in details permeation-driven flows and their applications [14]. They proposed a model for the mass transfer of water from the microchannel into the PDMS. This model explains the link between the flow-field into the channel and the geometrical parameters of microfluidic channel, see Fig. 1.3.

The mass transfer of water in PDMS is described by the Fick diffusion equation, where the diffusion coefficient of water is $D \simeq 10^{-9}$ m^2/s. On the length scale of the mass transfer, the channel width w is very small, so that the mass transfer has the geometry of radial diffusion. They also model the mass transfer of water into the PDMS matrix using a constant-D Fickian diffusion as follows:

$$\frac{\partial c}{\partial t} = \nabla \cdot J_D,$$

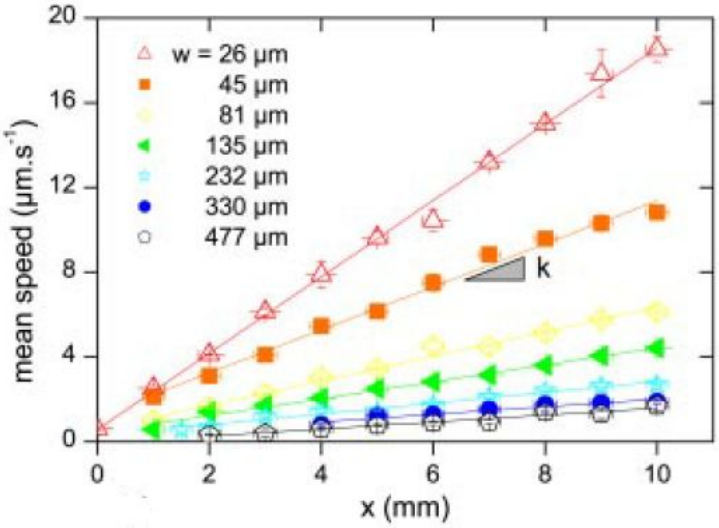

Figure 1.2: Pervaporation-induced velocity profiles in a straight microchannel along x. The different symbols correspond to different channel widths.

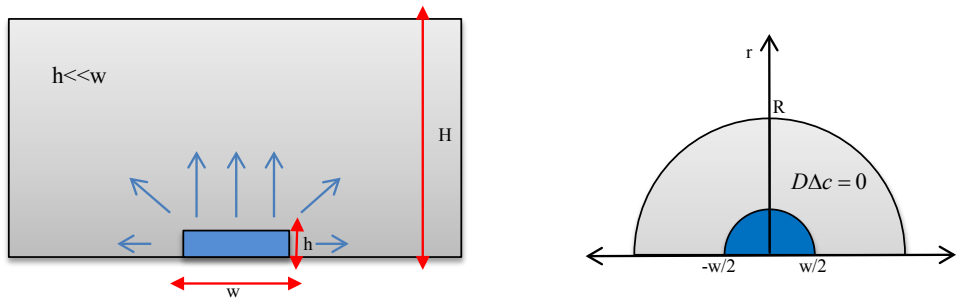

Figure 1.3: Left: geometry of the mass-transfer problem of water in a PDMS chip solved by Randall *et al.*. h and w are the height and width of the microchannel, $H \gg h$ is the typical dimension of the PDMS slab. Right: corresponding axis-symmetrical problem.

where $J_D = -D\nabla c$ is the flux of water molecules leaving the channel. The steady-state

equation for the flux J_D is:

$$\nabla^2 c = 0.$$

On the mass-transfer scale, $h \simeq 0$ so that the diffusion problem in PDMS reduces to diffusion from a thin 2D slab with a finite width w. If it is assumed that the outer PDMS boundary can be modeled as a cylindrical boundary of radius R and $c(R) = 0$ and the other boundary condition at the channel ceiling is: $c\left(-w/2 \ll y \ll w/2, z = 0\right) = c^*$, it is possible solve the steady-state equation in cylindrical coordinates (Fig. 1.3):

$$D\frac{\partial}{\partial r}\left(r\frac{\partial c}{\partial r}\right) = 0,$$

and Randall *et al.* calculated the expression of the flux J of water molecules leaving the channel:

$$J(r) = -\frac{\pi D c^*}{w \ln\left(\frac{w}{4R}\right)}.$$

The flux of water in the channel increases as the width w decreases as observed experimentally by Verneuil *et al.*, see Fig. 1.2.

1.1.2 Evaporation-induced pumping

The microevaporator was developed by Leng *et al.* [10]. For a better control of spatial and temporal evaporation, they joined a thin PDMS membrane on the microchannel, following the works on valves and micropumps made of PDMS of Quake *et al.* [15] and Goulpeau *et al.* [16]. Figure 1.4 shows a microevaporator developed by Leng *et al.*. A microfluidic channel with a width w, a height h and an evaporation length L_0 is molded into a PDMS matrix. The channel is closed by a thin PDMS membrane with thickness e. A portion of the channel is closed by a glass slide. From the end of the channel to the glass slide, the length of the channel defines the evaporation length L_0. Typical dimensions of microevaporators are $h \simeq$ 5-100 μm, $w \simeq$ 20-500 μm, $L_0 \simeq$ 0.5-10 cm. The thickness e of the membrane varies between 10 and 50 μm. Two areas appear in the channel: a non-pervaporation zone where the channel is closed by a glass slide and an evaporation zone only closed by a membrane. We will call "reservoir" the area without evaporation and "evaporator" the evaporation zone.

Let us consider the case where the microevaporator is filled with pure water. Water in the channel pervaporates through the thin membrane, which induces a compensating flow from the reservoir to the tip of the channel. Figure 1.5 shows the mass conservation in a microevaporator. In a box of size dx, the input flow in the channel $Q(x + dx)$ is the sum of flow $Q(x)$, and pervaporation rate q_e. q_e depends on the humidity of the ambient air and the thickness e of the PDMS membrane. We defined the evaporation velocity v_e as $q_e = wv_e$. Mass conservation implies:

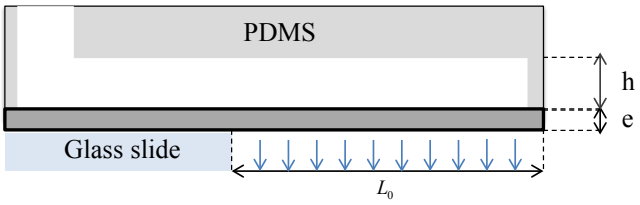

Figure 1.4: Sketch of a microevaporator as developed by Leng *et al.*, see text.

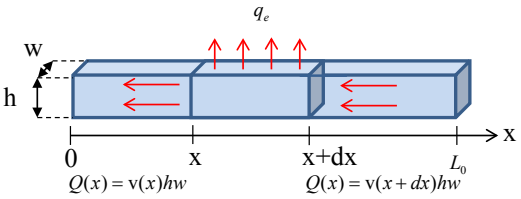

Figure 1.5: Mass conservation along the microevaporator.

$$Q(x+dx) - Q(x) = q_e, \tag{1.1}$$

where flows are given by:

$$\begin{aligned} Q(x) &= -V(x)hw, \\ Q(x+dx) &= -V(x+dx)hw, \end{aligned} \tag{1.2}$$

So we obtain:

$$hw\frac{\partial V}{\partial x} = -q_e(x) \tag{1.3}$$

where h, w are the transverse dimensions of the channel (Fig. 1.5) and L_0 is the evaporation length of the channel exposed to the membrane. In Eq. (1.3), $V(x)$ is the width and height-averaged volume velocity in the channel, x the long axis direction of the channel. So the velocity at the position x in the channel of microevaporator is given by:

$$V(x) = -\frac{q_e x}{hw} = -x\frac{v_e}{h} = -x/T_e. \tag{1.4}$$

The velocity is constant in the reservoir $V_0 = q_e L_0/wh$ while it decreases along the evaporator until it becomes zero at the end of the channel (Fig. 1.6). The velocity profile

is determined by three parameters: the pervaporation rate q_e and dimensions h and w. From the velocity profile, we can determine the velocity of the liquid in the reservoir V_0, the pervaporation rate q_e and the evaporation time $T_e = wh/q_e$ which corresponds the time needed to empty one volume of channel. For classical microevaporators, that consist of

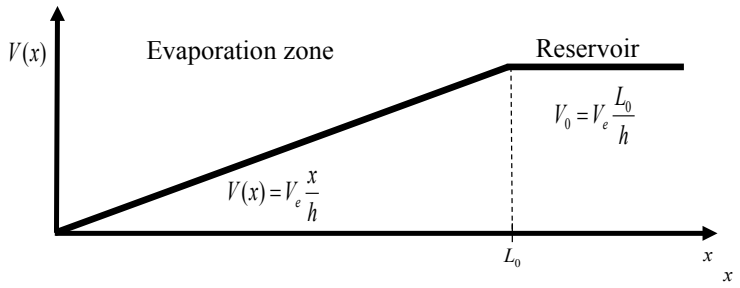

Figure 1.6: Pervaporation-induced velocity profile.

microchannels of size $w = 50-100$ μm, $h = 15-50$ μm, $L_0 = 1-5$ mm and $e = 20-50$ μm, one has $V_0 = 1 - 10$ μm/s and $T_e = 500 - 1000$ s. For such geometries, q_e depends on the transverse dimensions h and w of the channel, as demonstrated by Randall *et al.*, see above. In the geometrical limit of very flat channels ($h \ll w$) in contact with ultra-thin membranes ($e \ll w$), pervaporation proceeds across the membrane only so that v_e does not depend on w.

1.1.3 Evaporation-induced concentration of solute

The concentration of the solute occurs as a consequence of this evaporation-induced flow. Indeed, water evaporates through PDMS but the solute (non permeable in PDMS) is driven towards the tip of the channel where it accumulates. It was demonstrated that the microevaporator is capable to concentrate electrolyte solutions [10], polymers [17] [18], surfactants [19], as well as colloidal dispersions [20] or nanoparticles [21], up to dense states (see later). In the case of microevaporator as developed by Leng *et al.*, the solutes are convected up to the tip of the channel by the convective flow, j_c. The solute is concentred at the tip of channel creating a concentration gradient. This implies diffusion of the solute, j_d, which tends to homogenize the solutes in the channel. In the case of dilute solutions, the fluxes j_c and j_d are defined by:

$$\begin{aligned} j_c &= \phi(x)V(x), \\ j_d &= -D\partial_x\phi, \end{aligned} \tag{1.5}$$

where D is the diffusion coefficient of the solute, that describes the transport property of the dispersion/solution, and ϕ the concentration of solute along x. The convection and diffusion fluxes are shown schematically Fig. 1.7. In this model, we consider the

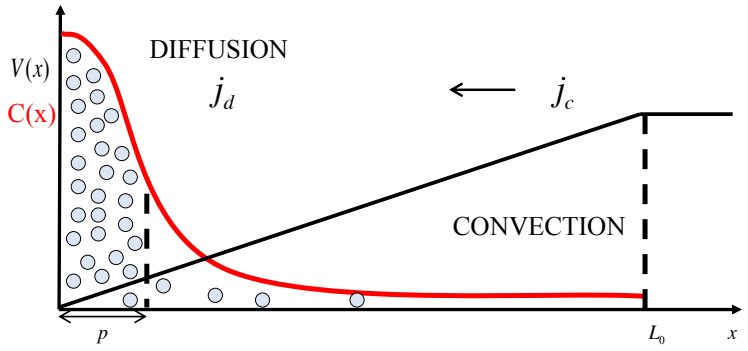

Figure 1.7: Skecth of the concentration process, $p = \sqrt{DT_e}$ is the size of the accumulation box.

case of homogeneous concentration field across the dimensions h and w. Convection and diffusion compete together, it is thus possible to separate the channel into two regions with a crossover at a distance $p = \sqrt{DT_e}$ defined by the balance of the two fluxes $j_d \simeq j_c$. p defines a characteristic length scale of a virtual accumulation box, where the solute accumulates. The size of this zone depends on the dimensions of the particles, through their diffusion coefficient and the parameters of the microevaporator. In Fig. 1.8, Leng *et al.* [10] have shown experimentally the dependence of the size of the accumulation box with the solute's mobility. This figure shows four microfluidic channels of dimensions

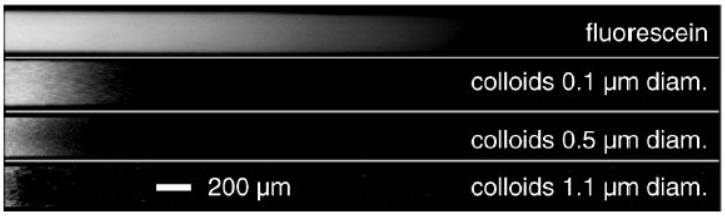

Figure 1.8: 4 identical microevaporators filled with 4 different fluorescent solutes ranging from the molecular scale up to large colloids. The size of the accumulation box decreases when the mobility of the solute decreases.

$h = 15$ μm, $w = 300$ μm, $L_0 = 5$ mm and $e = 25$ μm, in which different solutions

and dispersions concentrate. The mobility of the solute varies from the molecular scale to colloids of 1.1 μm. The accumulation zone decreases as the mobility of the species decreases, up to several microns for the case of the largest colloids.

The accumulation rate of the solute in the accumulation zone is estimated from the solute conservation. The convection zone serves as a pump which delivers solutes at a rate $(wh)j_0$, where j_0 is the incoming rate of solute $j_0 = \phi_0 v_0$. Concentration increases following:

$$pwh\Delta\phi \approx j_0 wh\Delta t; \tag{1.6}$$

So the rate of concentration in the accumulation zone is:

$$\frac{\Delta\phi}{\Delta t} \approx \frac{\phi_0 V_0}{p}; \tag{1.7}$$

This estimate shows that several factors affect the concentration rate. It is influenced by the nature of the solute (via its diffusion coefficient), the concentration in the reservoir ϕ_0, the geometry of the microevaporator (via V_0). In the following we will see that this relation allows us to estimate the time needed to concentrate a solute in a given microevaporator.

1.2 Ideal microevaporators

1.2.1 Solute transport

Salmon and Leng described the functioning of *ideal* microevaporators [22]. They considered that the dimensions of the channel, w and h are constant along the evaporator. The solutions used are also ideal, it means that the diffusion coefficient D of solute does not depend on the concentration and that activity, expressing how the evaporation is altered by presence of a solute, is constant and equal to 1. The solutes do not pervaporate through the PDMS and are not subject to chemical reactions. The viscosity and density of the solution is constant. For these dilute solutions of concentration ϕ_0, solute transport is described by the sum of two fluxes, j_c and j_d.

$$j(x) = -D\partial_x\phi + \phi(x)V(x). \tag{1.8}$$

Solute conservation equation $\partial_t\phi + \partial_x J = 0$ leads to:

$$\begin{aligned} \partial_t\phi &= D\partial_x^2\phi - \phi\partial_x v - v\partial_x\phi, \\ \partial_t\phi &= D\partial_x^2\phi + \phi/T_e - \frac{x}{T_e}\partial_x\phi \quad \text{for} \quad x < L_0, \\ \partial_t\phi &= D\partial_x^2\phi - V_0\partial_x\phi \quad \text{for} \quad x > L_0. \end{aligned} \tag{1.9}$$

The boundary conditions are defined by $j(x=0) = 0$ et $j(x \gg L_0) = j_0$, where j_0 is the input flux in reservoir.

We make the above model nondimensional using:

$$X = x/L_0, T = t/T_e \quad \text{and} \quad C = \phi/\phi_0 \tag{1.10}$$

The previous equations now read:

$$\begin{aligned} \partial_T C &= \frac{1}{Pe}\partial_X^2 C + X\partial_X C + C \ \text{ for } \ X < 1, \\ \partial_T C &= \frac{1}{Pe}\partial_X^2 C + \partial_X C \ \text{ for } \ X > 1, \end{aligned} \tag{1.11}$$

where the Peclet number is defined by:

$$Pe = \frac{V_0 L_0}{D} = \frac{L_0^2}{p^2}, \tag{1.12}$$

This number represents the ratio between the convection transfer and diffusion transfer. Two regimes appear. The first one is the stationary regime in which the microevaporator is first filled with a solution of concentration ϕ_0 and then this solution is replaced with pure water. In this case, all of the particles in the channel are convected up to the tip of the channel, where it remains due to the continuous water flow. It is thus possible to observe a steady concentration profile coming from the competition between the diffusion of the particles and the convection. The second regime is a continuous regime in which the solutes concentrate continuously in the microdevice, we give below some analytical approximations of the concentration process in that regime.

1.2.2 Asymptotic regime

As the pervaporation is still in progress, concentration profiles do not reach a stationary regime. So we can look for an asymptotic regime of concentration of solutes, after a transient time. The nondimensional particle flux is given by:

$$J(X) = -\frac{1}{Pe}\partial_X C - XC. \tag{1.13}$$

From this equation and the mass conservation $\partial_t C + \partial_x J = 0$,

$$\partial_T J = \frac{1}{Pe}\partial_X^2 J + X\partial_X J. \tag{1.14}$$

In the asymptotic regime, $\partial_T J = 0$. The solution of this equation is:

$$J(X) = \ \text{erf}\left(\sqrt{\frac{PeX}{2}}\right), \tag{1.15}$$

and concentration profiles follow:

$$\partial_t C(X) = \sqrt{\frac{2Pe}{\pi}}\exp\left(-\frac{1}{2}PeX^2\right). \tag{1.16}$$

After integration of this equation, the concentration profile in space and in time at long time scales is given by:

$$C(X,T) \approx \sqrt{\frac{2Pe}{\pi}} \exp\left(-\frac{1}{2}PeX^2\right) T + R(X), \tag{1.17}$$

where $R(X)$ is an integration constant. Again, we can define $P = p/L_0 = \sqrt{Pe}$, the size of the accumulation box normalized by the evaporation length.

For $X \gg P$, the flux of solute is predominantly dominated by convection, and follows:

$$\partial_T C = X\partial_X C + C = 0. \tag{1.18}$$

The steady solution of this equation is:

$$C(X) = R(X) = \frac{1}{X}. \tag{1.19}$$

So for $X \gg P$, concentration profiles collapse on an "hyperbolic ramp" in microevaporators. The concentration profile for long time is thus:

$$C(X,T) \approx \sqrt{\frac{2Pe}{\pi}} \exp\left(-\frac{1}{2}PeX^2\right) T \quad \text{for} \quad X \ll P, \tag{1.20}$$

$$C(X,T) = \frac{1}{X} \quad \text{for} \quad X \gg P. \tag{1.21}$$

These expressions indicate that the concentration field follows a Gaussian profile which increases linearly in time for $X \ll P$, and solutes follow a steady hyperbolic ramp for $X \gg P$.

Figure 1.9 displays the temporal evolution of such concentration profiles calculated using numerical resolution of Eqs. (1.11), for two different Peclet numbers. At long time scales, the previous analytical relations correctly fit those numerical resolutions.

1.2.3 Transient regime

The transient regime corresponds to the establishment of the stationary hyperbolic ramp. Figure 1.10 displays numerical resolutions of Eqs. (1.11), for two different Peclet numbers in the transient regime, i.e. at small time scales. For $P \ll X < 1$, the flow is predominantly dominated by convection because the concentration gradients are very low, and concentration field follows:

$$\partial_T C = X\partial_X C + C. \tag{1.22}$$

The establishment of the stationary hyperbolic ramp thus follows:

$$C(X,T) = \exp T \quad \text{for} \quad C(X,T) < 1/X, \tag{1.23}$$

$$C(X,T) = \frac{1}{X} \quad \text{for} \quad T > -\ln X.$$

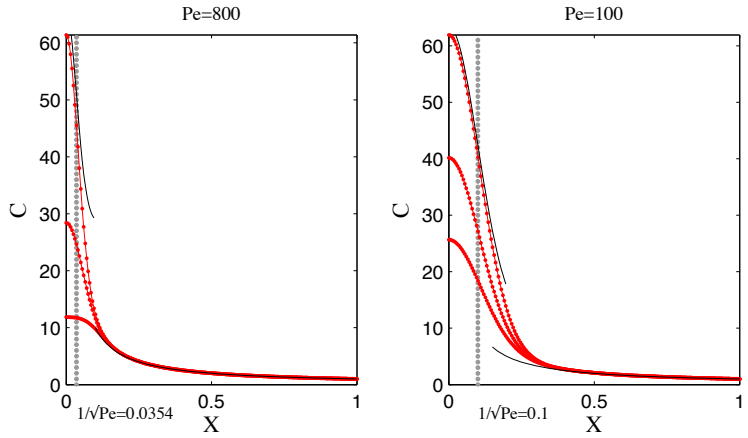

Figure 1.9: Asymptotic concentration profiles $C(X,T)$, for several times t and for two Peclet numbers ($Pe = 100$, $Pe = 800$) calculated using the numerical resolution of Eq. (1.11). Left: $Pe = 800$ for times $t = 2$, 3, 5. Right: $Pe = 100$ for times $t = 4$, 6, 9. The red dots correspond to the numerical computation and the grey dots correspond to the size of accumulation box, p. The dark lines are the approximations given by the hyperbolic ramp and Eq. (1.26) for the last times.

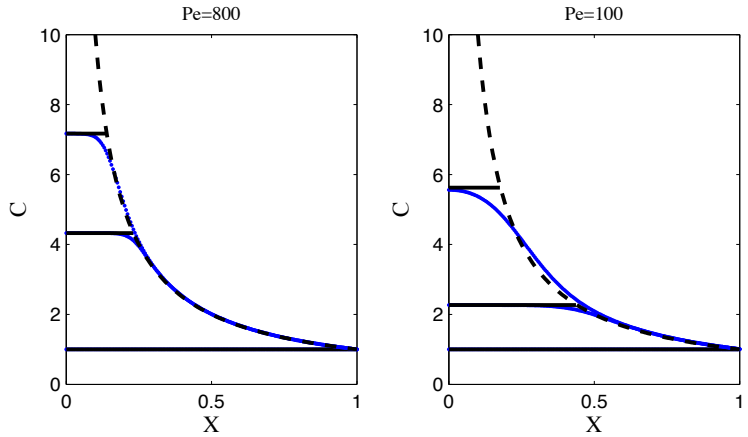

Figure 1.10: Concentration profiles $C(X,T)$, for several times and for two Péclet numbers ($Pe = 100$, $Pe = 800$). Left: $Pe = 800$ for times $t = 0.1$, 1.4, 1.9. Right: $P_e = 100$ for times $t = 0.1$, 0.8, 1.7. The blue dots are the numerical solution, the dashed line the hyperbolic ramp, and the dark lines the approximation of Eq. (1.23).

Equation (1.23) shows that at the beginning of the process of concentration, the profile increases exponentially along the microevaporator up to reach the hyperbolic ramp $C(X) = 1/X$. Equation (1.23) correctly fits the numerical resolution given in Fig. 1.10.

We can also define $T^\star$ the time scale to build the complete hyperbolic ramp up to $X = P$, where diffusion cannot be neglected anymore. This transient is given by:

$$C(P, T^\star) = \exp(T^\star) = \frac{1}{P} = \sqrt{Pe}. \tag{1.24}$$

The transient time is $t^\star = T_e T^\star$:

$$t^\star = \frac{T_e}{2} \ln Pe = \frac{T_e}{2} \ln \left(\frac{L_0}{p} \right). \tag{1.25}$$

Thanks to this transient time, we can modify the analytical expressions describing the asymptotic regime given above, see Eqs. (1.20), to take into account the concentration process during the transient:

$$C(X, T) \;=\; \sqrt{\frac{2Pe}{\pi}} \exp\left(-\frac{1}{2} Pe X^2 \right) (T - T^\star) + \sqrt{Pe}. \tag{1.26}$$

Figure 1.11 shows numerical solutions of Eqs. (1.11) for two different Peclet numbers and at $X = 0$. It corresponds to the temporal increase of concentration at the tip of the channel. The previous equations, Eq. (1.26) for the asymptotic regime, and $C(0, T) = \exp(T)$ for the transient, correctly fits the concentration rates.

In this section, we described the concentration of solutes in the case of dilute (ideal) solutions where we hypothesized that the activity of the solution and that the diffusion coefficient of the solutes are constant. In the following, we will analyze the more general case where these two parameters vary with the concentration.

1.3 From dilute solution/dispersion up to dense states

We have seen above that the microevaporator is a tool that allows to concentrate continuously chemical species in aqueous solutions. This process continues up to the formation of dense states for which the hypothesis of ideal solutions do not apply anymore.

When solutes are concentrated enough, the activity of the solution and the diffusion coefficient of the solute determine the shape of the concentration profile established in the microchannel. The model given by Ajdari and Schindler [23] allows to determine $\phi(x, t)$ and the corresponding permeation-induced velocity profile $v(x, t)$ in that concentrated case. The evolution of these two fields is governed by the conservation equations including the diffusion coefficient of solute $D(\phi)$ and the activity $a(\phi)$ of the solution, which both depends on the concentration ϕ. This model reads:

$$\partial_x v(x, t) \;=\; -\frac{a(\phi) - h_e}{T_e} \tag{1.27}$$

$$\partial_t \phi(x, t) \;=\; -\partial_x (\phi v(x) - D(\phi) \partial_x \phi) \tag{1.28}$$

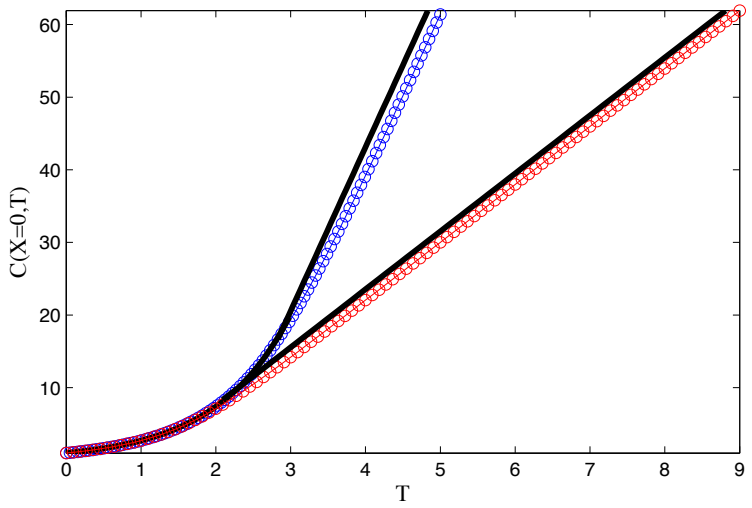

Figure 1.11: Concentration at $X = 0$ for two different Péclet numbers (blue circles $Pe = 800$ and red circles $Pe = 100$) calculated from numerical resolution of Eq. (1.11). The continuous lines are analytical approximations in the transient regime and in the asymptotic one.

where $a(\phi)$ is the activity of the dispersion, h_e humidity and $D(\phi)$ the mutual diffusion coefficient of dispersion.

At higher concentration, a dense state may appear, and we give below several examples of experiments that use microevaporators to explore phase diagrams from dilute solutions up to dense mixtures.

1.3.1 Exploration of phase diagrams

Figure 1.12(left) shows the extremity of 3 microvaporators with different lengths L_0, connected to the same reservoir and filled with a KCl dilute solution. The high concentration rate in the 7 longest channels led to the nucleation and growth of salt crystals at the time of the picture. The shortest channels have a lower concentration rate, and the concentration at the tip of the channel is not large enough to nucleate a crystal. Figure 1.12(right) displays the size x_f of such crystals in the microevaporators for different concentrations c_0 in the reservoir (37, 123, 372 mM) as a function of time. As shown in the corresponding work [10], these curves collapse when plotted against x/L_0c_0. The microevaporator thus allows the kinetic and qualitative exploration of a phase diagram of an aqueous solutions.

For the more general case of ternary solutions (water and 2 solutes), microevaporation leads to a new complexity since the concentration process depends on the mobility of each species (see above). It is thus difficult to use such devices to explore complex phase diagrams. However, Moreau *et al.* proposed an evolution in the design of microfluidic device as shown Fig. 1.13(left:top) [17]. At the tip of the channel, a "storage area" is

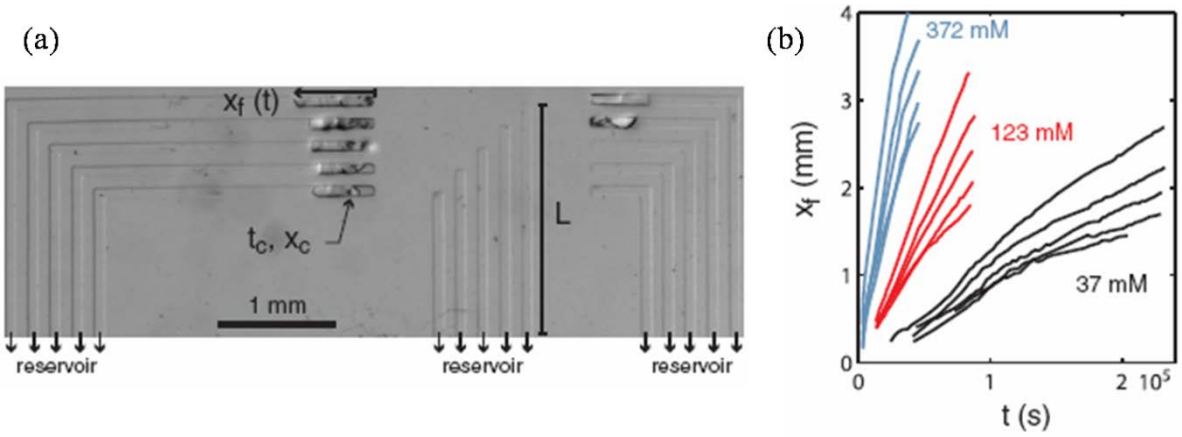

Figure 1.12: Left: view of the chip with 15 microchannels with different evaporation lengths L_0 (the bottom of the image is the end of the evaporation zone). In each channel, the evaporation-induced concentration leads to crystalization of KCl crystals that invade the channels at a rate $\dot{x}_f(t)$. Right: crystal fronts $x_f(t)$ for various evaporation lengths L_0 and initial concentrations $c_0 = 37$ mM (bottom), $c_0 = 123$ mM (middle), $c_0 = 372$ mM (top).

added where there is no evaporation of water. Only diffusion occurs in this zone. Moreau *et al.* demonstrated that such microfluidic devices (and for specific geometrical constraints of the storage area), lead to a concentration rate in the storage area that is independant os the solute mobility. It is thus possible to explore phase diagrams of two or more solutes, quantitatively.

Figure 1.13(left:bottom) evidences a series of phase transitions for the case of polymer and salt solutions, as observed in the storage area at different time scales. Starting from a homogeneous system, it takes a certain time (Figs. B and C) before a liquid-liquid transition takes place. After this transition, the system remains under evaporation and is still enriched with the solutes; the size of the two domains evolves (Figs. D-F), and crystallization of the salt phase occurs (Fig. G). Ultimately, we recognize the solidification of the polymer-rich zone (Fig. H).

Quantitatively and based on the time-concentration equivalence, is possible obtain the kinetic phase diagram as shown in Fig. 1.13(right) where the initial conditions are displayed as red dots at low concentrations. The calculated trajectories (thanks to simple mass conservations laws) end up at the times where the liquid/liquid transition is observed. Blue dots are data extracted from equilibrium measurements and agree very well with kinetic calculated results.

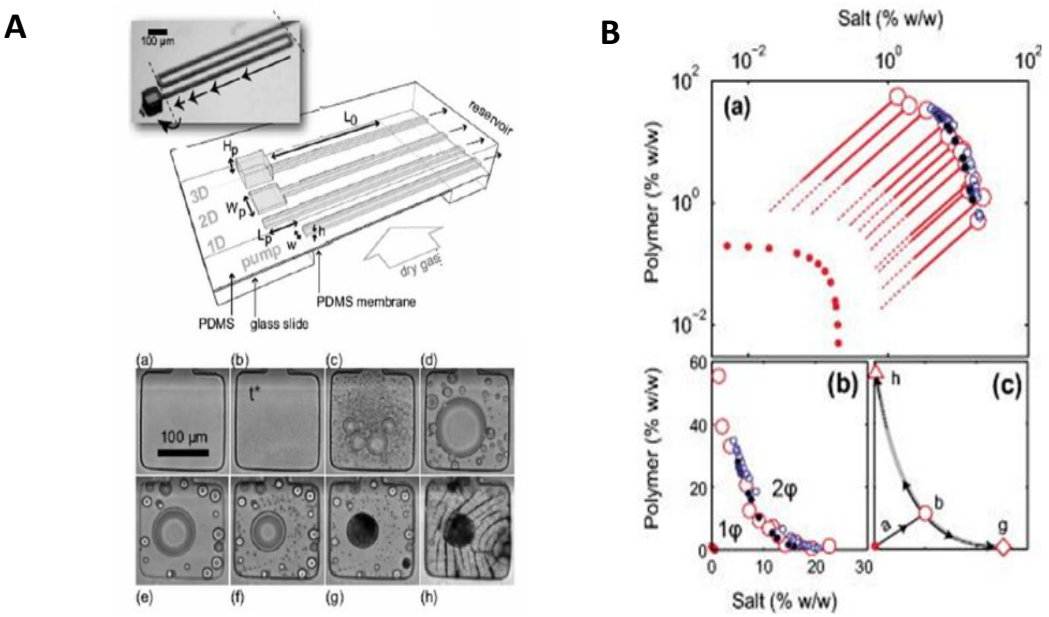

Figure 1.13: Left(top): sketch of the storage device which connects a solute pump (a linear evaporator in contact with a membrane) to a storage pool sheltered from evaporation, Left(bottom): Series of micrographs showing a sequence of events taking place in a 2D solute pool initially filled with a dilute aqueous solution of PEG and salt. As time passes, several transitions are visible. Right: phase diagram of the binary salt-PEG system.

1.3.2 Nucleation and growth of colloidal crystals

In the previous sections, we saw that the concentration profile of the solute results from the competition between convective flux, which tends to confine solutes at the tip of the channel, and diffusion flux. There is thus an accumulation box where diffusion dominates, and where solutes concentrate. In the asymptotic regime, this concentration continues until a dense state nucleate. This then begins to grow along the channel as continously fed by the evaporation flux. The formation of a dense state has been observed many times, for many different solutes, and often a dense material grows and invades the microevaporator. This has been observed for surfactants, salts, polymers, nanoparticles and colloids. We detail below the case of colloids only. A. Merlin studied the process of concentration of dilute dispersions of charged colloids (polystyrene 250 nm radius) using microevaporation [20, 24]. She followed by optical and confocal microscopy the growth of dense states of colloids in various microvaporators ($h = 5 - 30$ μm, $w = 20 - 100$ μm, $L_0 = 0.5 - 10$ cm and $e = 10 - 30$ μm). Figure 1.14 shows a series of pictures of the monitoring of the

concentration of colloidal particles, and the subsequent growth of the colloidal crystal at the tip of the channel. By manipulating the chip after complete invasion of the dense pack-

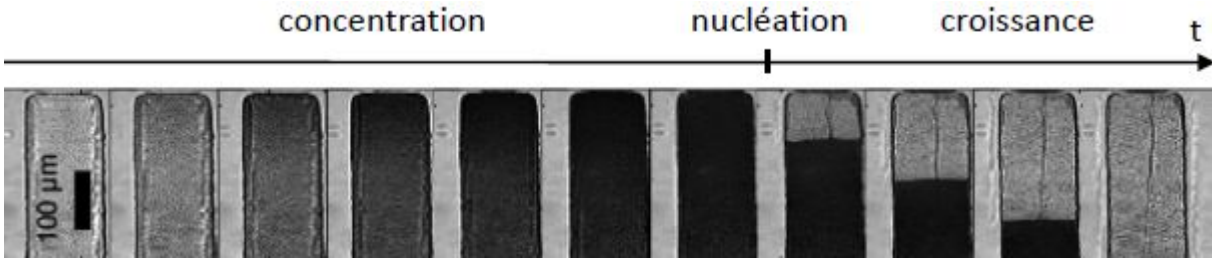

Figure 1.14: Series of snapshots at the tip of the channel ($w = 100$ μm) during the process of concentration of a colloidal dispersion of polystyrene beads ($R = 250$ nm and $\phi_0 = 0.3\%$). The time elapsed between two images is 15 minutes [20].

ing, under different incident white light, intense colors appear characteristics of colloidal crystals (Fig. 1.15(a)). The observations of the dense state is done using scanning electron microscope(SEM) after peeling of the membrane. SEM shows well-organized colloidal crystals, see Fig. 1.15(b, c)).

The front position (x_f) of the dense packing is also monitored during these experiments (Fig. 1.16). The growth at short times is fast and constant at long time scales. These observations were modeled by Merlin *et al.*. Colloids display a very low mobility, and corresponding Peclet numbers are thus extremely high. Because initial concentrations tested (ϕ_0, 0.5 to 4%) are large, nucleation of the dense colloidal packing occurs during the establishment of the hyperbolic ramp. In this model, concentration profiles are given by Eqs. (1.20), where diffusion is neglected, up to a critical value ϕ_d corresponding to the maximal packing fraction of colloids.

In this simple model, crystallization thus begins at $x_f = L_0(\phi_0/\phi_d)$ at time $t_N = t_e \ln(\phi_d/\phi_0)$. In this model $t_N < t^*$, so $\ln(\phi_d/\phi_0) < \ln\sqrt{Pe}$, valid for the case of an infinite Peclet number. Then, the velocity of the growing front is calculated using conservation of solutes, see Fig. 1.17. Mass conservation reads:

$$(\phi_d - \phi(x_d))v_f = j_0 = \phi_0 v_0$$

In front of the dense assembly of colloids, the concentration profile follows the steady hyperbolic ramp, and one has simply:

$$(\phi_d - \phi_0 L_0/x_d)v_f = j_0 = \phi_0 v_0.$$

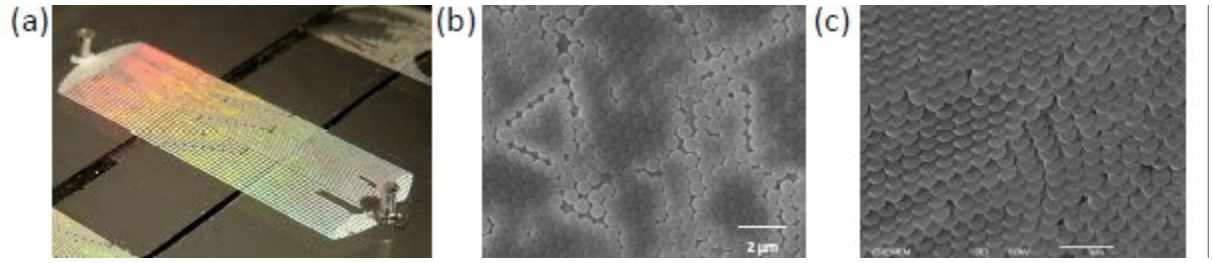

Figure 1.15: (a) Picture of two microfluidic evaporators filled with colloidal crystals, (b) and (c) SEM images of colloidal crystals [20].

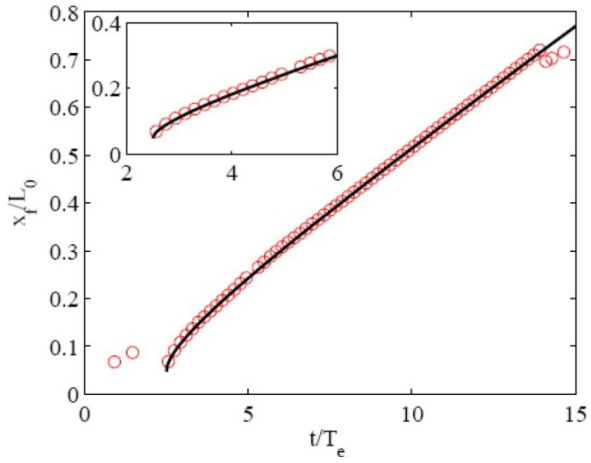

Figure 1.16: Temporal evolution of the position of the front x_f during the concentration of a colloidal dispersion of polystyrene beads ($R = 250$ nm and $\phi_0 = 0.3\%$). Inset: zoom on the growth at short times. The black solid line corresponds to a fit by a model [20].

which gives an implicit equation for x_f:

$$\frac{\phi_d}{\phi_0}\frac{x_f}{L_0} - 1 - \log\left(\frac{x_f}{L_0}\frac{\phi_d}{\phi_0}\right) = \frac{V_0}{L_0}(t - t_N). \tag{1.29}$$

Taking into account this conservation law, it is possible to fit the position of the front of the dense state (see Fig. 1.16) and to extract the dense phase volume fraction ϕ_d of the colloidal crystal. From different initial volume fractions ϕ_0, A. Merlin obtained $\phi_d \approx 65\%$ [20]. This model is valid whenever there is a continuous evaporation of water in the dense state, that

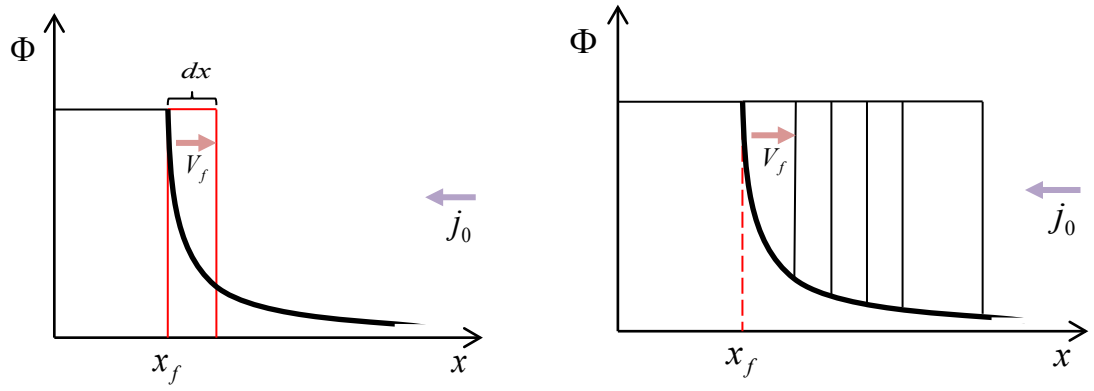

Figure 1.17: Left: schematic profile of the concentration during growth. The incident flux of particles j_0, induces the growth of the dense state at a velocity v_f. Right: invasion of the colloidal crystal.

is ensured in the case of colloids as the dense packing remains always full of water. Indeed, for colloids, even at high volume fractions, activity of the dispersion $a(\phi)$ remains always close to 1, as colloids have a larger volume compared to the volume of water molecules [18].

1.4 Fabrication and calibration of a microevaporator

1.4.1 Fabrication of a microevaporator

The microevaporators that we use, are made of networks of channels molded in a block of PDMS with a thickness between 0.5 to 1 cm, and closed by a membrane with thicknesses ranging between 10 to 50 μm. The microdevice is mounted on two glass slides, which define the evaporation zone. The protocol used to make microevaporators consists of three steps. The first step consists in drawing the wanted design on a mask. The second step is to make a mold with a fingerprint of the mask, using lithography. The third step is to mold the network of channels with PDMS. This well-known method is called "soft lithography" and was developed by Whitesides *et al.* [25].

Design of the mask

The pattern of the mask are drawn using a drawing software, in our case Clewin. Then the design is printed at high resolution (20000 dpi) on a transparent mask. We choose the width and length of our channels at this step. In general, multiple independent microevaporators are drawn on this mask (see Fig. 1.18).

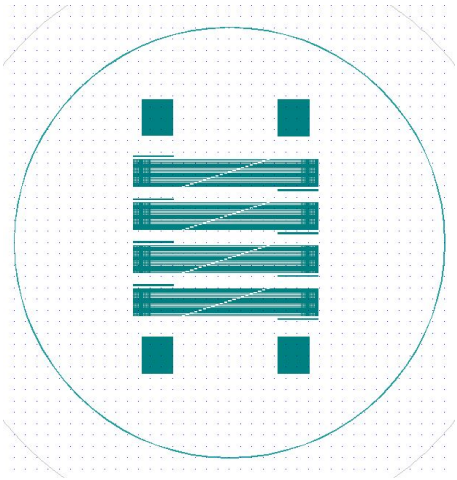

Figure 1.18: Example of design used during the thesis. The size of the circle correspond to the size of a silicon wafer of 3 inches. 8 independant systems containing 21 microevaporators are drawn.

Manufacturing of the mold

The mold is fabricated by photolithography. To fabricate the mold we use a negative photoresist (SU-8 MicroChem) which can reticulate under UV irradiation. Several types of resists exist with different viscosities. MicroChem has adequate protocols to obtain the desired height of the mold. We developed microdevices with different heights h ranging between 5 and 50μm. The basics of the protocol (see Fig. 1.19) is the same for each height, but the resist, the velocity and durations are different. A silicon wafer is first cleaned with plasma cleaner (Harrick plasma cleaner, model PDC-002) for 45 seconds. This step cleans the silicon wafer to facilitate the bonding of the resist. Then the resist is spread by spin-coating. The rotation speed controls the thickness of the resist. The resist is then heated to 95^{o}C C to evaporate the solvent, this step is called the "soft bake". The resist is then exposed to ultraviolet radiation through the mask. The resist is again heated at 95^{o}C ("post exposure bake") and developed thanks to (1,2-propanediol monomethyl ether acetate, PGMEA). Finally, the mold is cleaned with isopropanol. The final step is the silanization of the mold, to facilitate the subsequent release of the PDMS microdevice. The result is a thick mold (thickness h) containing two-dimensional networks of channels in relief on the silicon wafer (Fig. 1.20). The heights are measured using a mechanical

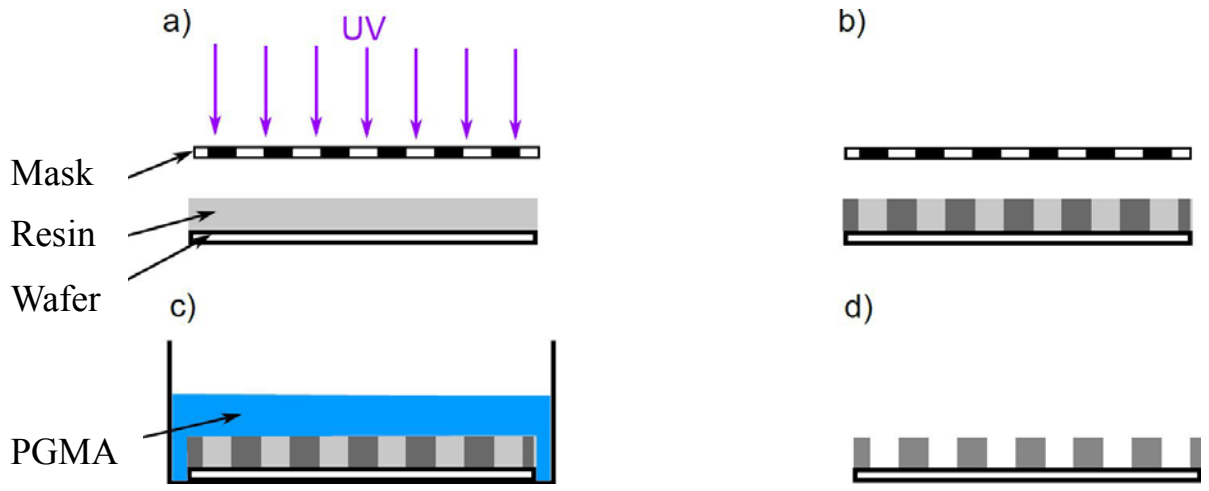

Figure 1.19: (a) The mask is positioned on the silicon wafer covered by a resist layer, and is irradiated by a UV lamp. (b) The UV-exposition causes the reticulation of the resist. (c) We reveal the design of the mask using PGMEA. (d) We obtain an engraving in negative of the microchannels. Their height is measured using a mechanical profilometer.

profilometer whose resolution is 100 nanometers. This mold can be used many times to make PDMS microdevices.

Fabrication of a PDMS microfluidic chip

With our mold it is possible to make a microevaporator. We first formulate a mixture of PDMS (Dow Corning Sylgard 184) and its curing agent with a mass fraction ratio 7:1. This mixture is then degassed to remove air bubbles. The mold is placed in a petri dish and covered by the PDMS mixture. The two are baked at 65^{o}C for 30 minutes. We prepare at the same time, a mixture of PDMS/curing agent with a mass fraction ratio 12:1, that we will use to make the permeation membrane of the microevaporator. We use the spin-coating method to form a membrane from the mixture 12:1 with a uniform thicknesses of about 30 μm on a silicon wafer. This wafer is then baked at 65^{o}C for 10 minutes. During this time the main PDMS microfluidic chip is peeled off the SU8 mold, and we punch holes with a large needle to make the reservoirs. The corresponding PDMS block is then deposited over the membrane and the system is left at 65^{o}C for two hours. The gradient of curing agent between the membrane and the block of PDMS allows to firmly bind the two PDMS layers [26]. The chip and the membrane are then peeled off the wafer carefully, and the final chip is placed on two glass slides. A typical example is shown Fig. 1.21.

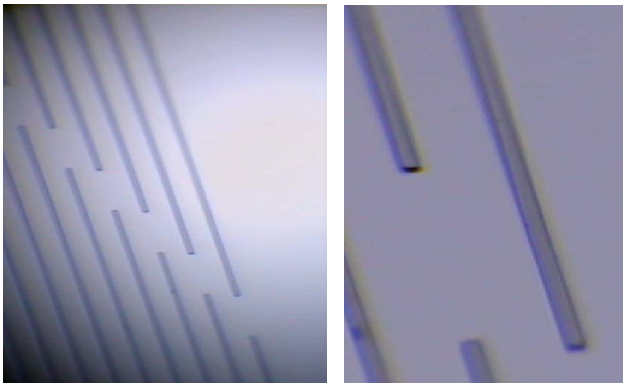

Figure 1.20: Examples of molds fabricated during the thesis (channel dimensions: $h = 10$ μm, $w = 40$ μm). The pictures were taken by reflection optical microscopy.

1.4.2 The principle of calibration

Calibration is an important step to use the microevaporator. It allows us to determine three characteristic parameters: the evaporation velocity V_e, the evaporation time T_e, and the incoming velocity in the reservoir V_0, see Fig. 1.6 that displays the velocity profile along the evaporator. We recall that the velocity field is given by:

$$\begin{aligned} V(x) &= -\frac{x}{T_e} \text{ for } x \leq L_0 \\ V(x) &= -V_0 \text{ for } x > L_0 \end{aligned} \tag{1.30}$$

Before each experiments, the characteristic parameters of the microevaporator are measured. The method of calibration is the following: the device is placed under a binocular microscope which is connected to a CCD camera. The channel is filled with pure water, and we dry out the reservoir. As water pervaporates through the PDMS membrane, an air/water meniscus invades the channel starting from the reservoir. The monitoring of the air/water meniscus in the area without pervaporation (i.e. above the glass slides) allows us to determine V_0. We thus acquire a movie with a typical acquisition time of about 1 s between two successive images. Image analysis of the movie is made thanks to a Matlab code. Briefly, we subtract the image captured at time $t + dt$ and that captured at time t. The resulting image is black except at the meniscus position (provided that dt is not too large). Then we look for the position of the maximum of the image, and we represent the corresponding position of the meniscus versus time. The pixel conversion length is determined by a reference ruler.

1.4.3 Results of calibration

We detail here a typical example of a calibration. The chip used consists of 21 parallel channels of height $h = 10$ μm, width $w = 40$ μm, and evaporation length $L_0 =$ ranging

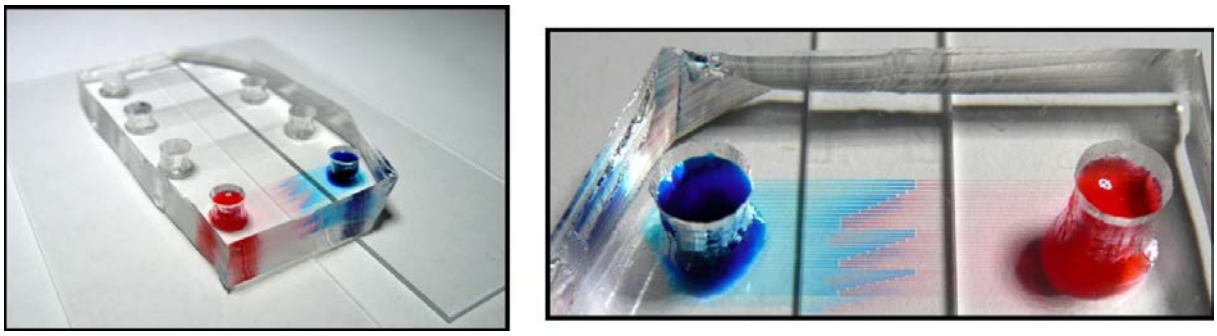

Figure 1.21: Left: example of a PDMS microfluidic evaporator. This system consists of 7 independant systems of 30 microevaporators. Two reservoirs are filled with colored dyes. Right: zone on the two systems filled with dyes. Concentration gradients of dyes indicate the concentration process. All microevaporators connected to the same reservoir have a different length L_0.

between 0.7 and 12 mm. The membrane thickness is $e = 30$ μm. Figure 1.22 shows the position of the meniscus in the reservoir for one channel with $L_0 = 5175$ μm. Its evolution is linear in time and thus V_0 is given by the slope of the line, $V_0 = 30$ μm/s in that case. We can then deduce the pervaporation velocity and the evaporation time, $V_e = V_0 h/L_0$ =50 nm/s and $T_e = h/V_e = L_0/V_0$=245 s.

1.4.4 Role of the evaporation length L_0

Figure 1.22 shows the different measured values of V_0 in the reservoir for different evaporation length L_0 (0.7–12 mm). Velocities range from 5 μm/s up to 80 μm/s for the longest channel. These velocities correspond to evaporation time that are roughly 245 s. It means that the time scale to empty one volume of each microevaporator is about 4 minutes. The corresponding flow rates Q_0 are about 70 nL/hr for the longest channel.

Moreover, we observe that V_0 obeys an affine law as a function of L_0. T_e is thus not constant for all the channels, and decreases particularly for the smallest one. This is not expected from the description of the function of microevaporators given at the beginning of the present chapter, see Eq. (1.4). We find indeed more precisely

$$V_0 = \alpha L_0 + V_l,$$

with $V_l = 1.4$ μm/s. This velocity V_l correspond to a "leakage" velocity indicating that evaporation also occurs at the tip of the channel at $x = 0$. This leakage velocity has been observed many times in the previous works concerning microevaporation, and it may play a role that we have not studied in details in the present manuscript. In the following, we

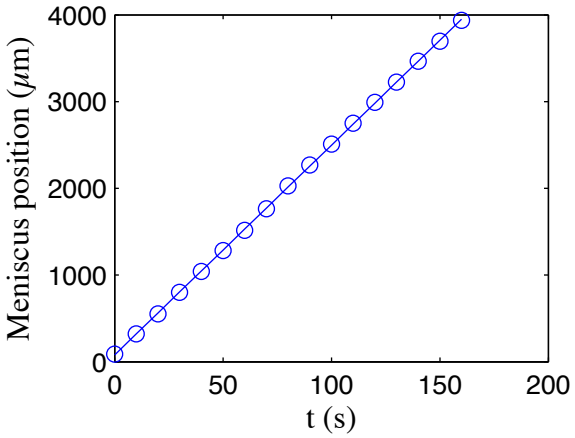

Figure 1.22: Position of the air/water meniscus against time obtained by an automatic detection during calibration; evaporation length $L_0 = 5$mm, width $w = 40$ μm and height $h = 10$ μm. The thickness of the membrane is $e = 30$ μm. The continuous line is an affine fit, whose slope is V_0.

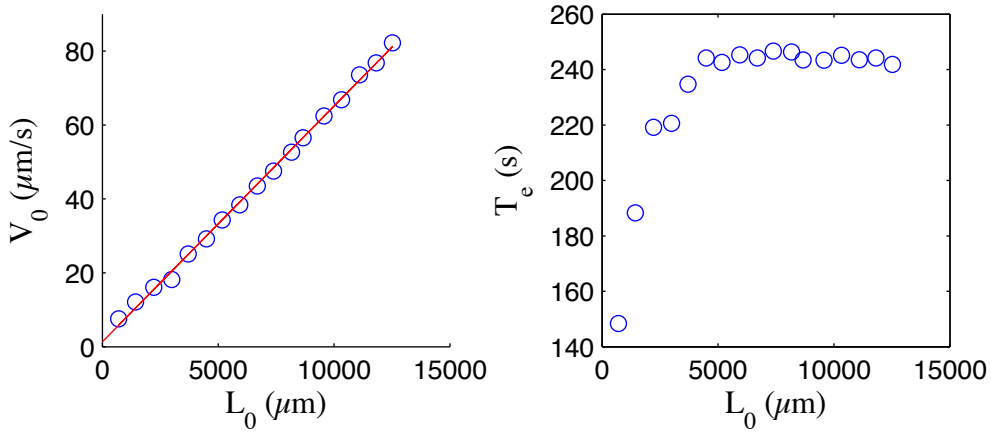

Figure 1.23: Right: velocity in the reservoir V_0 as a function of evaporation lengths L_0. The red line is an affine fit of the data. Left: evaporation time (T_e) as a function of evaporation lengths L_0. Note that $V_0(L_0 \to 0) \neq 0$, which shows a leak at the tip of the evaporator, better evidenced when plotting $t_e = L_0/V_0$.

will always assume that V_0 is proportional to L_0 to use the analytical approximations given above.

1.4.5 Role of the external humidity

Figure 1.24 shows the different values of velocity V_0 in the reservoir for the different evaporation length measured at different values of the external humidity R.H (humidity related to saturated atmosphere). As expected the measurements of V_0 depend of the external humidity. All the curves collapse when the velocities are rescaled with R.H. For all the

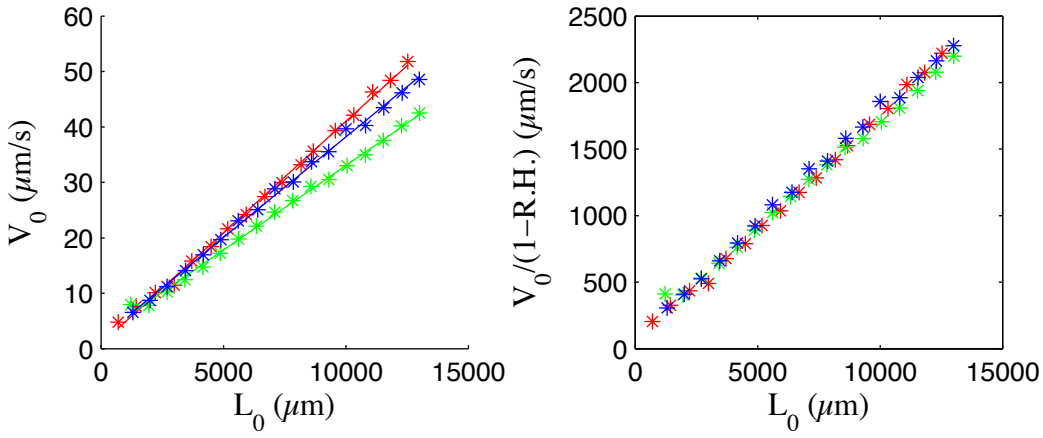

Figure 1.24: Right: velocity in the reservoir V_0 as a function of evaporation lengths L_0 for three different values of external humidity R.H., red dots $R.H.$ =0.37, blue dots $R.H.$ =0.36, green dots $R.H.$ =0.47. Left: rescaling of the velocities by the humidity, against L_0.

experiments performed during the thesis, we measured the external humidity of each experiment (that varies typically from 0.35 to 0.55), and we rescale all the characteristic parameters of the microevaporator from fluctuations of R.H. for comparison between several experiments.

1.5 Geometries of microevaporators

The aim of my thesis is to assemble metallic nanoparticles (NPs). They can indeed act as locally resonant structures, due to their plasmonic response. My strategy is to assemble them in order to create a "superlattice" thanks to the microfluidic evaporation. We worked with aqueous dispersions of metallic (mostly silver) NPs that we assemble by removing the solvent in order to increase their concentration. We worked with extremely dilute suspensions ($\phi_0 \simeq 10^{-5} - 10^{-2}$). This condition imposes strong constraints to design the microevaporator. Indeed, the classical microfluidic evaporation device (h =15 μm, w=50 μm, $L_0 = 0.5$ cm and $e = 50$ μm) needs approximatively 12 days (calculated using Eq. (1.7)) to concentrate a dilute dispersion ($\phi_0 \simeq 10^{-5}$) up to $\phi_d \approx 1$. It is clear that we have to minimize the duration of such experiments. We thus play with the parameters

of Eq. (1.7) to obtain a typical duration of an experiment of several hours, knowing the volume fraction of our dilute dispersion.

We know that the concentration process is efficient only for $p \ll L_0$, that is for a Peclet number $P_e = L_0 V_0/D = (L/p)^2 \gg 1$. For suspended nanoobject (size $>$ 10 nm) and for typical microevaporators, one has $p \simeq$ 100 μm which sets the minimal size of the microchannels. But we want to minimize the duration, $\Delta t \simeq (pt_e)/(\phi_0 L_0)$, so we maximize the length L_0 up to several centimeters, we can also scale down the product $pt_e \sim t_e^{3/2}$ by using thin devices ($h \approx 10$ μm) and thin membranes ($e \approx 30$ μm).

It is also necessary to respect the aspect ratio between the height h and width w of the channel. Indeed aspect ratios of PDMS microfluidic channels have to be lower than 1:20 (h/w), because the structures that do not respect this limit are prone to collapse (see Fig. 1.25). As a conclusion, the typically values used during this thesis are $e \simeq 30$ μm,

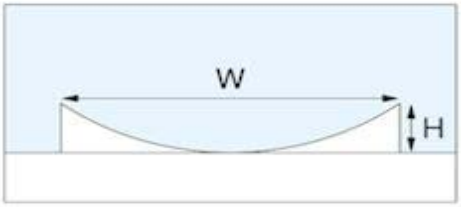

Figure 1.25: Collapse of the channel caused by a too large aspect ratio.

$h \simeq$ 10μm, $w = 40$ μm, leading to an approximate evaporation $t_e \simeq$ 250 s. Thanks to this optimization, the experimental time to concentrate a dilute dispersion ($\phi_0 \approx 10^{-5}$) up to a dense assembly ($\phi_d \sim 1$) decreases down to only 12 hrs. We also used two different geometries depending on the goal of our experiments.

Screening chip

The geometry of our screening chips consists of a group of 21 parallel of microevaporators, all of different lengths L_0, and which are all connected to the same reservoir (Fig. 1.26). The typical dimensions are: $h = 10$ μm and $w = 40$ μm. This microfluidic chip allows us to screen many different concentration conditions in a single experiment, thanks to the variation of the evaporation length.

Ellipsometry chip

This specific chip geometry was developed in order to perform ellipsometric measurements on dense materials, that grew in the microchannels. The width of the laser beam used

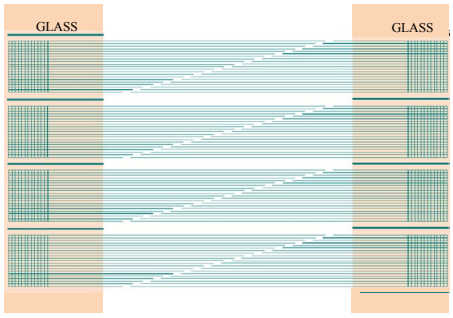

Figure 1.26: Top view of the screening geometry with 21 channels of different lengths L_0 (0.5-1.5 cm) all connected to the same reservoir.

in such experiment is typically 70 μm, and its length of the order of a few hundreds of micrometers. We thus modified the geometry of the chip to perform such experiments. The width of the channels is $w = 100$ μm, and this implies to increase the height of the channels up to $h = 15$ μm to prevent the collapse of the channel. L_0 was thus increased to reduce the duration of the experiment ($L_0 = 11$ cm, see Fig. 1.27).

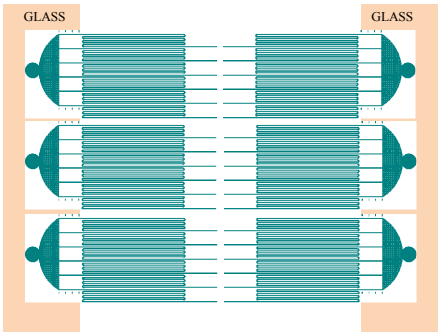

Figure 1.27: Top view of the chip used for ellipsometry experiments. The geometry consists of 6 independant blocks of 6 channels with a same length $L_0 =$ 11 cm, and all connected to the same reservoir.

Chapter 2

On-chip microspectrocopy

The object of this chapter is to illustrate a method to measure absorption spectra during the process of growth of our materials in our microfluidic tools. This method of measurements, based on the absorption spectroscopy, provides access to extinction spectra locally. The aim is to make an optical characterization of our micro-materials and to carry-out a spatio-temporal study of the kinetic properties of our dispersions under study. This instrumental chapter presents the theoretical basis of the method we used. The main experimental features of the instrument are described in the following sections.

2.1 Absorption spectroscopy: some general information

2.1.1 Visible spectrometry

Spectroscopy is the study of the interaction between radiation and matter as a function of wavelength (λ). Historically, spectroscopy referred to the use of visible light dispersed according to its wavelength, e.g. by a prism. Later the concept is expanded greatly to any measurements of a quantity as function of either wavelength or frequency. Thus it also can refer to a response to an alternating field or varying frequency (ν). A plot of the response as a function of wavelength or frequency is referred to as a spectrum. At the molecular level, one can relate the wavelength of the light to the photon energy using $E = h\nu$, and make a link between absorption spectroscopy and quantum mechanisms of light absorption by molecules (h is the Planck constant).

Spectrometry is the spectroscopic technique used to measure the concentration of given species (often in solution). In this case, the instrument that performs such measurements is a called a spectrometer or a spectrograph. Spectrometry is often used in physical and analytical chemistry for the identification of substances through the emitted spectrum or absorbed one. Spectrometry is also heavily used in astronomy and remote sensing. Most large telescopes display spectrometers, which are used to measure the chemical composition and physical properties of astronomical objects.

Absorption spectroscopy is a technique in which the intensity of a beam of light is measured before and after interaction with a sample. From a technical point of view, to obtain such a measurement, it is necessary to pass the light through the sample and to measure how much of light is transmitted. Actually, as we will see later in more details, we compare the intensity of the light transmitted across a solution or a dispersion (I_t) to the one transmitted across the pure solvent (I_r). Then, the transmittance is given by $T = \frac{I_t}{I_r}$ and the absorbance by $A = \log \frac{I_r}{I_t}$ (here log stands for the log in base 10), or some other relevant values can be calculated.

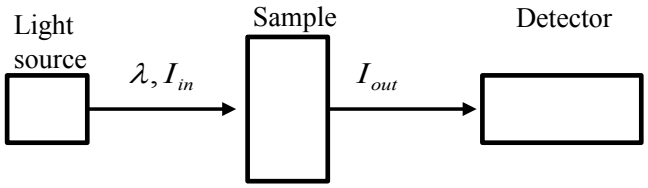

Figure 2.1: Measurement of the absorption of a sample. The light source produces a beam at the wavelength λ and with intensity I_{in}. The beam intensity after the sample is I_{out}, and absorbance is given by $A = \log(I_{in}/I_{out})$

The setup required to build a spectrometer is rather simple. It requires a source of light, for example a tungsten-halogen lamp which actually sets the range wavelength under

investigation. Optical elements such as fibers and lenses permit us to shine the sample and send the light to the spectrometer. The latter is made of a separator (a prism or a grating) and of a detector, typically an array photodetector which measures the whole spectrum at once.

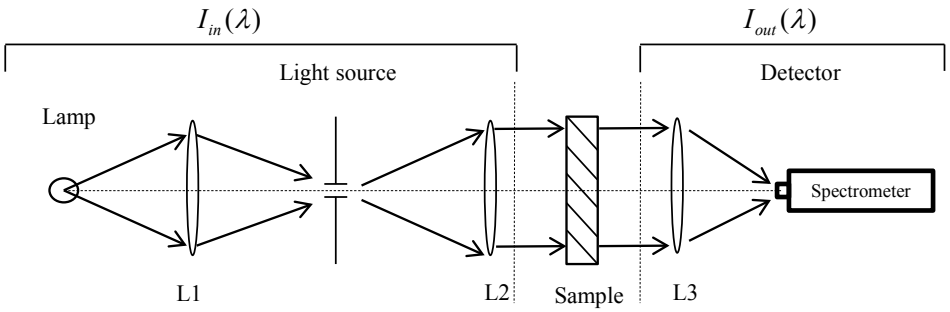

Figure 2.2: Shematical figure of a simple optical spectrophotometer. The lamp emission is collected by the lens L_1 and focused on the slit. The lens L_2 collects the light output slit and forms the monitoring beam. After the sample the light is collected by the lens L_3 and focused on the detector, the signal is decomposed by a spectrometer and is transmitted on the computer.

2.1.2 Spectrophotometer architecture

In a benchtop spectrophometer, there are actually two paths, one for the cuvette filled with the solvent only, and one for the same cuvette filled with the solution. In our case, we have a portable spectrometer in which there is only one path (Fig. 2.2), and therefore the measurements must be done twice: (i) once with a cuvette filled with the solvent which yields $I_r(\lambda)$, the reference intensity against the wavelength, and (ii) once with the sample in the same cuvette and for the same solvent to obtain $I_t(\lambda)$. The ratio of these two values gives the transmittance.

Some optical limitations arise. First, normal lenses, e.g. quartz lenses, display dispersion (i.e. a refractive index that depends on the wavelength). Therefore, they introduce chromatic aberrations (the focal length is different at different wavelengths). There exist achromatic lenses, which can reduce the chromatic aberrations but cannot avoid the problem completely in a wide spectrum range. The possible solution for this problem is to replace all the lenses by mirrors.

Then, some simplifying assumptions are needed to easily extract the transmittance. If we go more into the details of the path of light, we can write the intensities as a function of the incoming intensity (I_0) and material properties. The incoming light is first partially reflected on the first wall of the cuvette and attenuated in the wall of the cuvette ($I_1 = I_0 T_{AC} 10^{-A_C}$ where T_{AC} is transmission coefficient at the air/cuvette interface and A_C is the absorbance of the wall of the cuvette). Then, reflection occurs at the cuvette/liquid

interface and the beam is attenuated while flying in the liquid ($I_2 = I_1 T_{CL} 10^{-A_L}$ where T_{CL} is transmission coefficient at the cuvette/liquid interface and A_L is the absorbance in liquid). Same events occur while passing across the second wall of the cuvette ($I_3 = I_2 T_{LC} 10^{-A_C} T_{CA}$). Thus:

$$I_3 = I_0 T_{AC} T_{CA} T_{CL} T_{LC} 10^{-2A_C} 10^{-A_L}. \tag{2.1}$$

We call I_r the case where the liquid is the pure solvent and I_t the one with the solution or dispersion. Note that the transmission coefficients T_{CL} and T_{LC} are actually function of the refractive index of the medium which is different in principle for the solvent and for the solution. In most cases, one works with dilute solutions for which the refractive index is close to that of the solvent, and we can safely neglect this complexity: transmission coefficients are identical for the solvent and the solution.

Then, to get a more precise estimate of the transmitted light, we account for the noise of the detector, called dark intensity I_d, which is collected without light. Thus the exact expression for the transmittance now reads:

$$T = \frac{I_t - I_d}{I_r - I_d}. \tag{2.2}$$

It is clear from above that no obvious simplification exists in principle. If we assume that the actual intensities I_r and I_t are much larger that the dark intensity, we indeed obtain that $T = I_t/I_r$ at the first order in $I_d^2/(I_t I_r)$. All above assumptions are valid in the dilute regime. Additionally, we make the difference between absorption and extinction, the latter taking into account the scattering of light which may occur in the case of dispersions.

Example of spectroscopic measurements in solution

Figure 2.4 shows an example of measurements which were performed in a cuvette. The

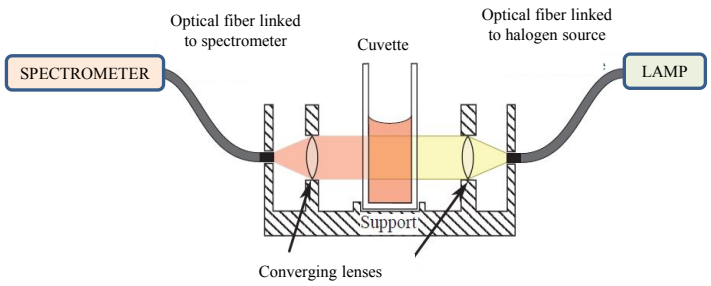

Figure 2.3: Experimental setup for the spectroscopic measurements done in cuvette.

spectrophotometer we used is sketched Fig. 2.3: a support for the cuvette is connected

to the inlet and the output of the optical fiber. This fiber is connected to a light source and to a spectrometer. Importantly, two converging lenses are integrated into the support for the cuvette. The first one provides a parallel beam passing through the solution to analyze. This is necessary to reduce the sensitivity of the mounting position of the cuvette (mechanical uncertainty in the support for the cuvette). The second collects the maximum power in the output fiber. The details of the spectroscopy configuration are:

- for illumination, a halogen light source (AvaLight-DH-S, 400-2500 nm) is used with a black body radiation at 3200 K;
- for the collection: USB Avantes, AvaSpec-3648 spectrometer. Its spectral detection range is 200 nm to 720 nm;
- two optical fibers with a core diameter of 200 microns;

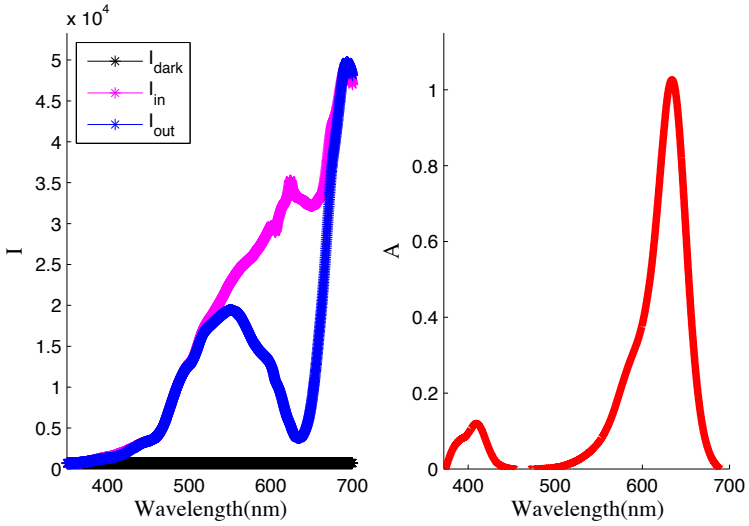

Figure 2.4: Intensity of light of reference, $I_{in}(\lambda)$, intensity of light of noise, $I_{dark}(\lambda)$ and intensity of ligth after the interaction, $I_{out}(\lambda)$, (left) and absorbance, A, (right) spectra of the sample: Brilliant Blue FCF solution.

The molecule of interest (Brilliant Blue FCF) is dispersed in water to get a blue solution that absorbs at around 600 nm. It displays the comparison between the reference, transmitted and dark spectra, and the resulting absorption. It shows the way we will always analyse the spectra acquired during this work. To summarize, this experimental setup allows us the characterization of highly diluted solutions over a spectral range which extends from 400 nm to 720 nm. Additionally, we will study next in details the sensititvy of the setup.

2.2 Microspectroscopy

The goal of my thesis is to engineer dense solids made of nanoparticles (NPs) for optical metamaterials. The targeted properties rely on the plasmonic properties of the NPs. The ones we used are mostly made of a metal core (Au or Ag) protected with a dielectric shell (in most case a silica shell or a polymeric corona). The material is built using a microevaporator that permits us to grow and shape-up solids, superlattices, extended and thick arrays of nanoparticles. The typical sizes of the materials we obtained are between 40 and 100 μm in width and several millimeters long. One of the technique to study the optical properties of such materials is the microspectrophotometry. The setup we present next is a modified microscope that can measure the absorption spectrum of a very small area inside a cell, typically a few microns. However, we will see that we are not able to measure transmission across these materials: even though the materials are thin ($\approx 1 - 10\,\mu$m), they are so concentrated that they absorb virtually all the light. We are thus left with the dilute regime and will see that our microspectrophotometer is capable at quantifying the kinetics of NP concentration in microchannels. We will also see that we develop a simple method for establishing the Beer-Lambert law with nanoliters of solution only. The main advantage of the technique remains a direct and non-intrusive approach for delivering quantitative analysis, quite useful in the field of microfluidic technologies and nanosciences.

2.2.1 Spectroscopy on a microscope

The goal of this experimental setup is to obtain space-time measurements of the absorption spectra in a microfluidic channel in order to study the kinetic process of fabrication of our material. It can also apply possibly to chemical or biochemical reactions, e.g. by the production of colored reactants. In our work, we will take advantage of the colored aspect of NPs in solution due to their plasmonic response.

We developed a microspectroscopy experimental setup mounted on a commercial microscope to study the optical behavior of plasmonic microstructures, fabricated by our microfluidic device. It seemed convenient because a microscope is a powerful and accurate optical bench, is a standard environment for microfluidic experiments, and makes the technique transportable to other labs. The experimental system must be able to resolve the dimension of typical microfluidic channels with a width in the range 40–200μm. The sample is illuminated using the light coming from an halogen lamp of the microscope, equipped with different colored filters. This filtered light is then focused on the sample thanks to the condenser of the microscope. It is also necessary to be able to shine and collect the light on a restricted area with an adjustable size. Then, the spectroscopy is achieved by moving pointwise the microfluidic device thanks to a motorized and automated stage, with a displacement accuracy of 1 μm. (Fig. 2.5).

The transmitted light is collected through the objective. 80% of the light is sent to an optical fiber that connects the detector to the microscope. The other 20% of the transmitted light is sent to a CCD camera (Hamamatsu C9100 digital camera) to monitor

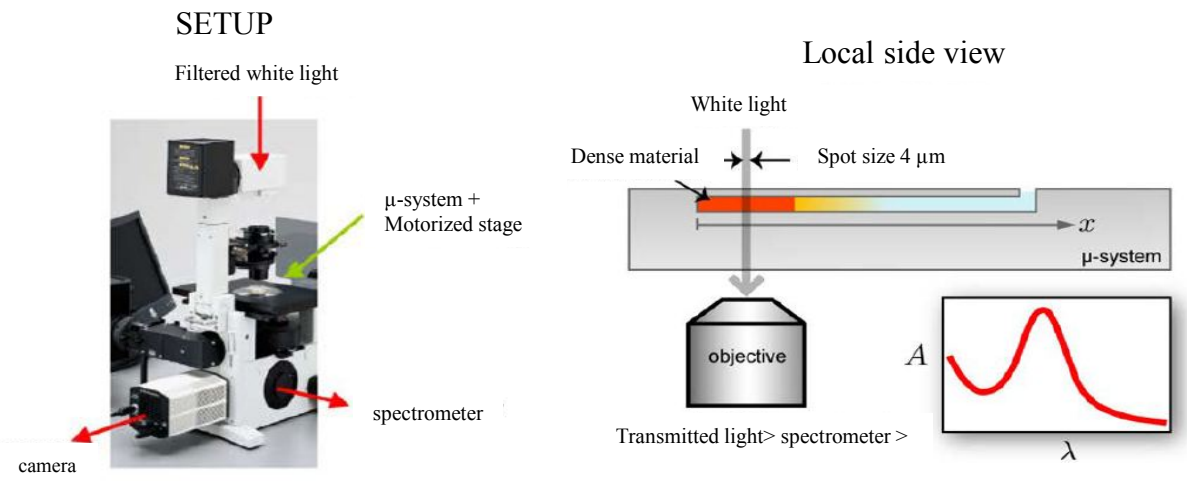

Figure 2.5: Experimental setup. Left: view of the inverted microscope with light coming from above and splitted after the sample between the camera and the spectrometer. Right: the sample is a microfluidic chip in which we measure absorption spectra (absrobance against wavelength) locally.

the evolution of the microfluidic evaporator (Fig. 2.6).

2.2.2 Details of the device

The experimental setup, illustrated in Fig. 2.5, is made using a microscope OLYMPUS IX71 (inverted research microscope). It is composed of the following elements.

Illumination

The illumination system of the optical microscope consists of a light source, here a halogen incandescent lamp, and a condenser (Fig. 2.6).

To obtain the absorbance spectrum of the sample in the microfluidic channel only (typical width 10–100 μm), it is necessary to respect the following conditions: the size of the focused incident beam must be lower than the width of the channel, and its divergence must be small to avoid light that crosses the sample non-normally. To obtain these conditions, we use the following optical configuration. The aperture diaphragm (just above the condenser) is set to its minimum size in order to get an almost parallel incident light (the numerical aperture of the condenser is thus very small). Then, the field diaphragm is also set to its minimal size to focus the light on a small illuminated field (see later for a discussion on the spatial resolution of our setup).

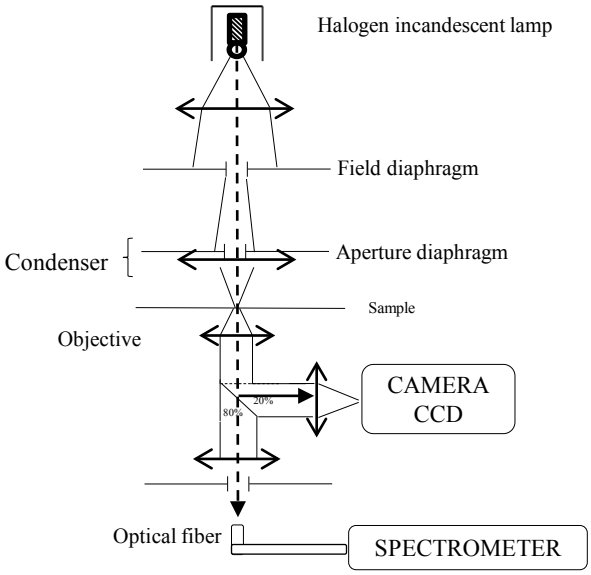

Figure 2.6: Optical configuration of the light transmission in the microscope.

Filter box

A set of filters is added in front of the halogen lamp to obtain the maximum intensity of the incoming light on the system under study in a given range of wavelength. The selection of chosen filters is related to the optical properties of the NPs under investigation. Most of the NPs used in the present work are silver NPs whose plasmon resonance is peaked around 400 nm. Fig. 2.7 (left) shows the intensity of the raw incident light, Fig. 2.7 (right) shows how two specific filters used alone modify the spectral intensity of the incident light. The combination of these two filters allows us to peak the spectral range of the incident beam around λ= 500 nm, which is much better than the raw light.

Sensitivity and absorption range

The spectrometer we used displays a range of detection between 200 and 720 nm. We discuss here the limits of the detectable absorbances. Many parameters are essential for the detection of a very low absorbance, for example the reproducibility of the measurements, the noise, the photometric stability. We show below that the maximum and minimum absorbance are totally dictated by the ratio of signal over noise. The latter is detector dependent.

Let us first estimate the minimum absorbance A_{min} we can measure. We assume that the sample does not absorb much, or $I_t = I_r - \epsilon$ where ϵ is small. Assuming also that the reference intensity is large compared to the dark one, we obtain that $A_{min} \approx \epsilon / I_r$.

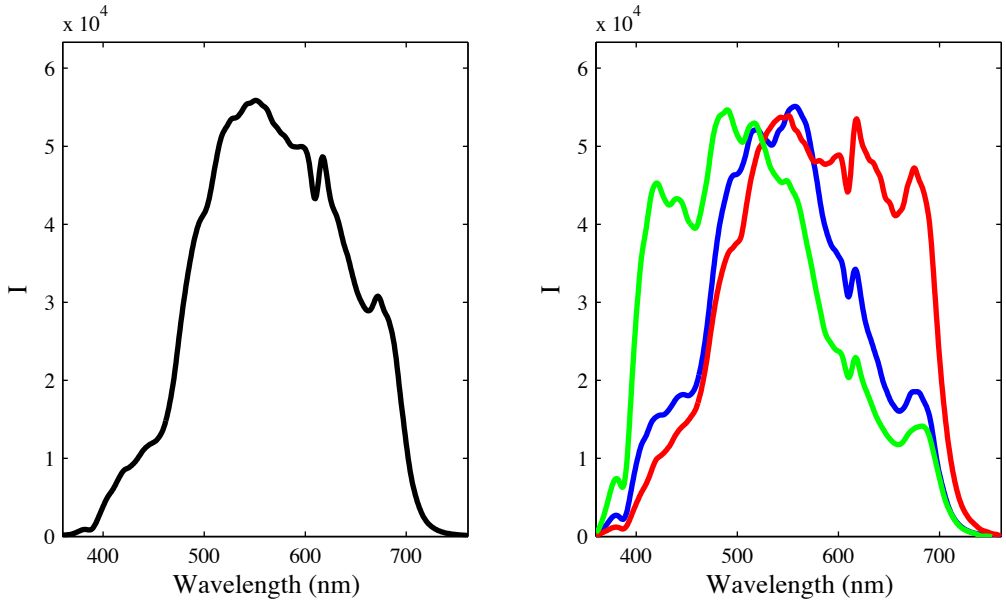

Figure 2.7: Left: spectrum of our halogen lamp. Right: lamp+blue filter (blue spectrum); white filter+lamp (red spectrum), and lamp+white+blue filters (green spectrum).

Moreover, the intrinsic error on A is given by

$$\Delta A = 2\frac{\Delta I}{I}, \tag{2.3}$$

where we assumed that both I_r and I_t are of the same order of magnitude and ΔI is the error on the intensity. In order to be able to measure A, one should have $A \gg A_{min} \approx \Delta A$. Assuming that $\Delta I \approx I_d$ it follows than the minimal absorption reads $A_{min} \approx 2I_d/I_r$. From a pragmatic point of view, the dark intensity of the spectrometer we used is $I_d \approx 30$ counts/s while the maximum value is $I = 2^{14}$ counts/s. Thus, $A_{min} \approx 0.004$ with our setup, but pratically the condition $A \gg A_{min}$ leads to detectable values around 0.04 only.

To obtain the maximum intensity, we follow the same idea. The sample absorbs a lot of light, thus I_t is small, but it needs to be larger than I_d. We assume that the limit is reached for $I_t \approx 10I_d$ and if the reference is much larger than the dark ($I_r \gg I_d$), we obtain $A_{max} \approx \log(I_r/Id) - \log 9 = 1.8$ with the values given above. Of course, the criterion is not so strict but clearly, higher absorptions at not measurable with our spectrometer. We are thus limited to 'small' absorbance and if one requires to measure a higher absorbance, it is possible to equip the spectrometer with a very sensitive detector (e.g. $A_{max} \approx 3.2$ for $I_r = 2^{16}$ counts/s and $I_d = 5$ counts/s).

The above argument is only valid for a given wavelength. To illustrate the sensitivity of our spectrometric measurements to the high absorbance value, as a function of λ, we plot the following curves in Fig. 2.8. More precisely, Fig. 2.8 left, shows the raw spectra of the halogen lamp I_0 (filtered with the filters mentioned above), dark blue curve. We also plot

different transmitted spectra that are calculated thanks to $I_0\,10^{-A}$ to illustrate the range of accessible A. To calculate the theoretical limit of the absorbance measurements, we

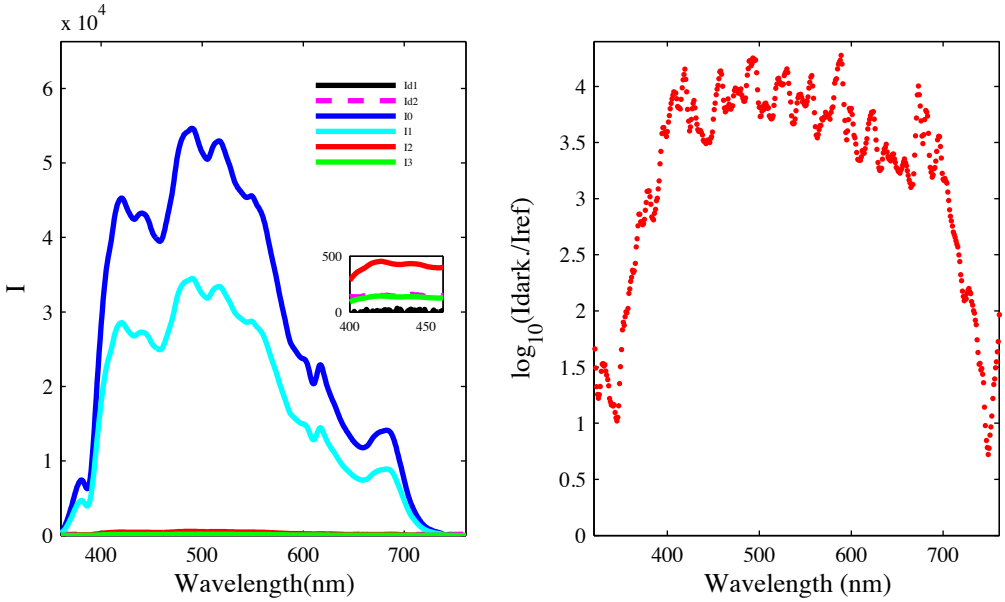

Figure 2.8: Left: spectrum of our halogen lamp filtered with the two colored filters discussed above I_0 (dark blue curve). We also plot $I_1 = I_0 10^{-0.2}$ blue curve, $I_2 = I_0 10^{-2.0}$ red curve, and $I_3 = I_0 10^{-2.5}$ green curve. See the insert for the low values. I_{dark} black curve, is the dark spectrum, and the magenta curve is $I_{dark} + \sigma$, where σ is the standard deviation of I_{dark}. Right: maximal detectable absorbance estimated from the reference spectra I_0 and the dark spectra (see text).

also plot in Fig. 2.8 right, $\log_{10}(I_{dark}/I_0)$. We remind that such values are too optimistic, and that a reasonable range of measurable A is $\log_{10}(I_{dark}/I_0) - 1.8$. Nevertheless, this plot shows that the maximal absorbance depends on the spectral range, it is small for $\lambda < 350$ nm, but roughly constant for 420–650 nm.

Spatial resolution

In our optical configuration, the spatial resolution of the measurements is set by a combination between the collection optics (an optical fiber and the microscope objective) and the spatial extent of the illumination zone; the latter is, in principle, set by the field diaphragm of the microscope. In order to image the zone where the objective collects the light, we use the principle of light reciprocity: we connect a halogen lamp to the fiber that normally collects the light. The reciprocity principle in optics tells us that the path of a photon remains the same if the direction of light propagation changes. Therefore, by injecting a stream of light at the output, the position of the collection zone is directly visible on the surface of the sample (a simple glass slide). By looking with the naked eyes, we see a well

defined circular and homogeneous spot of a few tens of micrometers (it depends of course of the magnification of the objective, but we keep it constant here and we use always a 20× magnification in order to collect sharp images of the video microscopy). We now demonstrate how the spectrometer permits us to give a much finer view on the collection zone.

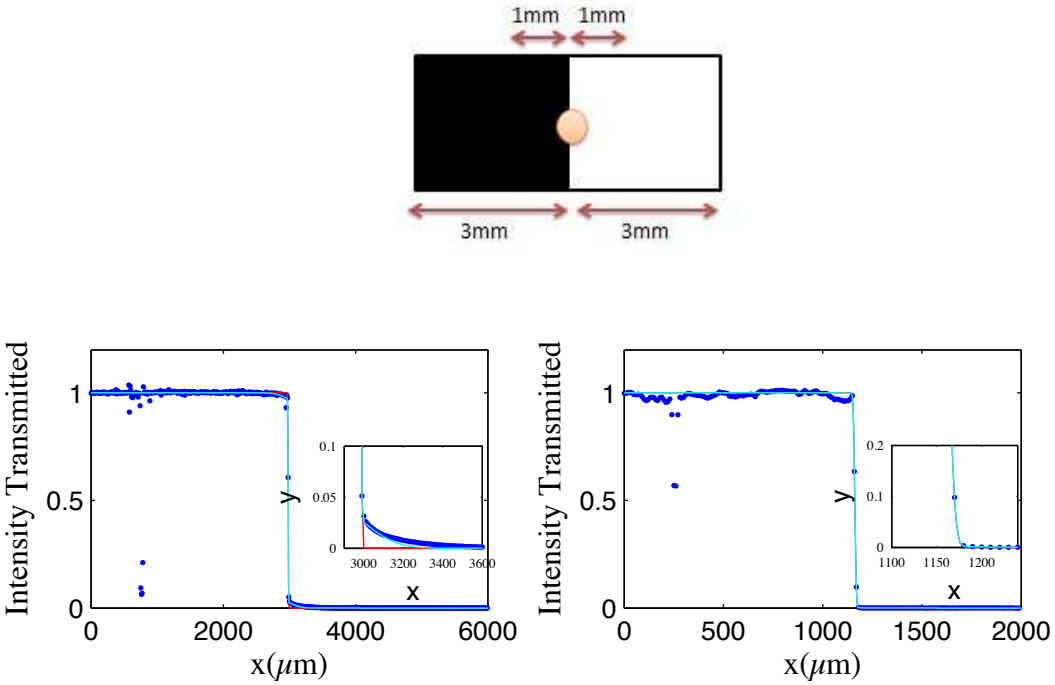

Figure 2.9: Top: schematic drawing of the opaque-to-transparent slide used to monitor the spatial extent of the collection zone in the setup. Bottom: transmission across the slide when it is move step by step with (left) standard illumination, (right) restricted illumination.

To precisely measure the size of the sampled volume, we use the following experimental protocol. We switch back to the direct setup with the spectrometer connected to the output and shine the sample with two different configurations detailed below. The sample is a glass slide with displays two different zones (see Fig. 2.9, top), a transparent one and an opaque one with a sharp transition ($< \mu$m, Edmund Optics). Using a motorized stage, we displace the glass slide with a fixed step (which ranges between 1 and 10 μm) in one direction in order to probe the transition from transparent to opaque regions, and we use the spectrometer to measure the transmission. We actually integrate spectra collected at each positions and eventually normalize them between 0 (no transmission) and 1 (transparent zone). Fig. 2.9, bottom left, shows a typical result with the transmission against space, which indeed features a sharp transition between transparency to opacity. In a first approximation, such a transition can be described using an error function as expected from the integration of a

Gaussian profile for the collected intensity:

$$I_t = \frac{1}{2}\left[1 - \mathrm{erf}\left(-\frac{x - x_0}{\sqrt{2}\sigma_1}\right)\right], \tag{2.4}$$

where x_0 is the position of the transition and σ_1 is the width of the collection zone, the quantity we are interested in (see the fit with the red line in Fig. 2.9, bottom left). Here, the illumination was set with the standard condenser and we find that $\sigma_1 \approx 30\,\mu$m. However, a magnification around the transition zone (inset of Fig. 2.9, bottom left) actually evidences that the transition has actually a larger spatial extent with a tail not well described by a single error function. Using a sum of two error functions:

$$I_t = \frac{1}{2}\left[1 - (1-\alpha)\mathrm{erf}\left(-\frac{x - x_0}{\sqrt{2}\sigma_1}\right) - \alpha\mathrm{erf}\left(-\frac{x - x_0}{\sqrt{2}\sigma_2}\right)\right], \tag{2.5}$$

(with α the ratio of two error functions and the σ_i their respective sizes) gives a much better agreement with the experiment (cyan line in Fig. 2.9, bottom left). We now obtain $\sigma_1 \approx 4$ μm, and $\sigma_2 \approx 140$ μm, and $\alpha = 5\%$. This indicates that the illumination zone is made of a spot with a size of few μm and small contribution of a larger spot with a size of about 140 μm. The latter is deleterious to the spatial resolution we can achieve (larger than the width of typical microfluidic channels).

We cannot reduce the collection zone because it is set by the objective of the microscope. But we can play with the illumination zone, and we strongly decrease the illumination field by adding a small aperture (75 μm diameter) just after the field diaphragm. In principle, it permits to shine light only in the principal collection zone of the objective. The resulting transmission curve is shown in Fig. 2.9, bottom right, with again a magnification of the transition zone in the inset of the same figure. We can now fit the curve *with a single* error function that leads to $\sigma_1 \approx 6$ μm.

The best optical configuration we can obtain is thus an optical microspot with a size of about 6 μm only when we use a pinhole placed against the field diaphragm. Unfortunately, in this configuration, the optical alignment is really difficult to achieve (recall we are not working on an optical bench). Beside, chromatic aberrations due to diffraction are observed and produce a colored spot at the level of the sample; thus illumination is not homogeneous in terms of wavelength, which makes it impossible to use. The ideal configuration would therefore be a compromise between a larger aperture of the field not to have diffraction and small enough one to fit into a microfluidic channel.

We will see later in the text that in the case of small absorbance, the size of the illumination beam is actually not an issue. Therefore, most of the results presented in this work were acquired using the simplest optical configuration (no additional pinhole or diaphragm at the level of the field diaphragm). We recall it leads to an axi-symmetrical illumination with a sum of two Gaussians, i.e. a microspot of about 4 μm and a larger contribution (140 μm) amounting for about 5 % of the total intensity.

Detection and signal acquisition

The light is collected using standard objectives made of special glass. It thus limits the wavelength sensitivity above about 350 nm. The light is then divided with a beam splitter and passed to the spectrometer (80% of the intensity) and to a CCD camera (Hamamatsu C9100 digital camera, 20% of the intensity). The latter is used to collect images during the experiments for video-microscopy. We thus obtain spectroscopy *and* video at the same time.

Temporal resolution

The spectrometer we used is linear, meaning that the intensity collected is proportional to the acquisition time. We chose it in order to minimize ΔA (see above), generally between 100 ms and 1 s. As we are studying slow processes (the growth of the materials within the channel is around 10 hours), we are not limited by this quantity.

2.3 Examples

Our goal is to perform spectroscopy on chip. We illustrate here that the setup is indeed functional but also has significant limits, especially when working with very absorbing media and also because of the peculiar form of the collected intensity (sum of two Gaussians).

The experimental protocol to measure an absorbance spectrum on chip is quite standard: (i) we acquire *a single* reference spectrum, (ii) we acquire *a single* dark spectrum, (iii) we acquire as many spectra of a given specimen as desired. Several points have to be mentioned: the thickness of the sampled volume must remain unchanged. It seems obvious but it is well known that PDMS is an elastomer and may get deformed under pressure or because of swelling; this issue is therefore not granted. Then, the reference intensity should be in principle collected at the same position as the specimen with solvent only; however, it is not always possible to flush the microsystem with solvent before or after use (especially for microevaporators which are single-use microsystems) to get the reference. We chose to measure the reference in PDMS just beside the channel. In principle, this approach is not valid but we checked the reference intensity in PDMS or in a channel filled with water is the same (within the accuracy ΔI mentioned above), which stems from the fact that reflection at the PDMS/channel filled with water are negligible: the intensity crossing twice an PDMS/water interface is reduced by 0.17% only ($I_t = (1-R)^2 I_0$ with $R = 0.08\%$ the corresponding Fresnel coefficient) which is of order of the relative accuracy we can detect ($\Delta I/I \approx 0.2\%$, see above).

2.3.1 Beer-Lambert law on chip

In this section the limits and possibilities of the experimental setup are analyzed and investigated in details. We first want to validate the setup with the-Beer Lambert law which relates the absorption of light to the properties of a given material through which

light travels. The law states a logarithmic dependence between the transmitance T of light through a substance and the product of the absorption coefficient of the specimen, α, and the light path in the material l. The absorption coefficient can be written as a product of either a molar absorption (extinction coefficient) of the absorber, ϵ and the molar concentration c of absorbing species in the material:

$$T = \frac{I_t}{I_r} = 10^{-\alpha l} = 10^{-\epsilon c l}. \tag{2.6}$$

The transmission is expressed in terms of an absorbance is defined as:

$$A = -\log(T). \tag{2.7}$$

This implies that the absorbance becomes linear with the concentration according to:

$$A = \epsilon c l. \tag{2.8}$$

Here, we perform a microfluidic chip made of a simple linear channel (1 cm long) molded in PDMS of height $h = 60\,\mu$m and width $w = 200\,\mu$m. We inject at very low pressure (not to deform the channel) a solution of molecular dye (Brilliant Blue FCF, Fig. 2.4) dissolved in water at known concentration, and we measure the absorbance. To start with, we use the simplest configuration with no pinhole (collection zone composed of two Gaussians of $4\,\mu$m and $140\,\mu$m). We first locate the spot in the middle of the channel and measure the absorbance for 5 concentrations ($c_1 = 0.16, 0.5, 1, 1.6$ and 2.1 mM). According to Beer-Lambert law, A/c should produce always the same spectrum.

Fig. 2.10 right shows A/c for the five concentrations. It is clear that the spectra do not all superimpose. At low concentration the rescaling is satisfying but becomes less and less good as the concentration is increased. More importantly, we observe that the shape of the spectra degrade at higher concentration and eventually become flat. Fig. 2.10 left shows the maximum absorbance against the concentration which is linear at low concentration, as expected, but plateaus at high concentration.

To explain this experimental result, we assume it comes from the fact that the collection zone is larger than the channel ($2\sigma_2 > w$). The light passing outside the channel and being collected by the larger spot is not attenuated by the dye in the channel and 5% of the intensity at least are never altered by the presence of dye in the channel. At very high concentration of dye, the smallest spot is totally attenuated but some intensity is still collected by the objective of the microscope: we thus estimate that this light contributes to make the absorbance smaller than it should be by a value $-\log(0.05) \approx 1.3$. It is indeed the plateau value we observe in Fig. 2.10, left.

We test this idea by reducing the illumination zone down to the size of the channel. To do this, we fabricate a series of linear masks of width W where the line is transparent and the rest is opaque. The masks are cut into an opaque slide using an automated cutter which can precisely cut designed shapes of sizes down to about $100\,\mu$m. By placing the mask just above the channel, we can test the influence of the illumination zone on A. We thus repeated the previous acquisitions (A vs c) for three masks ($W = 200, 500, 1000\,\mu$m).

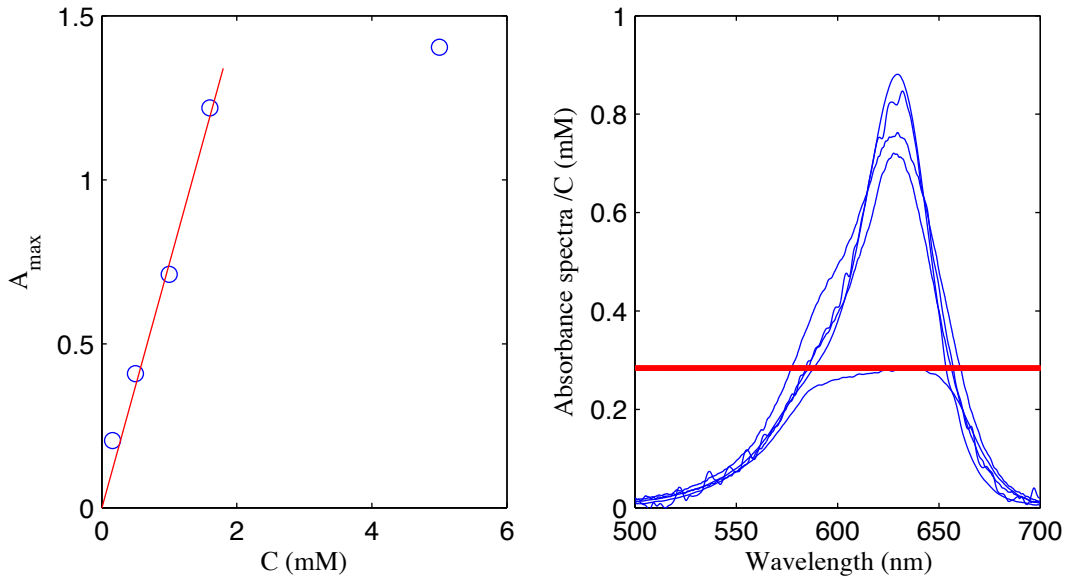

Figure 2.10: Beer-Lambert on a 200 μm wide chip. Right: rescaled absorbance A/c where c is the concentration of the molecular dye in the solution. Left: maximum absorbance against concentration. The red curve shows the flat part of the spectrum measured at high concentration.

The results are shown in Fig. 2.11. The right figure shows the absorbance spectra for 5 different concentrations in two experimental configurations: the red curves are the spectra measured with a mask ($W = 200\,\mu$m) that has the same size as the channel ($w = 200\,\mu$m), and the blue curves are the spectra measured without the mask. The results are spectacularly different, and highlight the influence of light transmitted through the PDMS outside the channel (in case of no mask) on the measurements. The figure on the left shows the maximum values of the absorbance against concentration for 4 different experimental configurations. We clearly observe that we can reach a much higher absorbance when the illumination zone is decreased. It confirms that even though only 5% of the intensity are collected outside the channel, they become predominant when the medium in the channel becomes more and more opaque.

We now present a simple calculation that quantitatively accounts for these results. From the previous measurements, we assume that the collected light can be described as the sum of two Gaussians normalized to one so that the total intensity integrated over space is 1:

$$I_t(x,y) = (1-r)G_1(x,y) + rG_2(x,y), \tag{2.9}$$

where $G_i(x,y) = (2\pi\sigma_i^2)^{-1} \exp\left(-\frac{x^2+x^2}{2\pi\sigma_i^2}\right)$ and r the intensity ratio of the two contributions. Here, we suppose that the spot is centered in $x = y = 0$. We then position a 'channel' with absorbing material, so that the intensity is locally altered with $I_t = TI_r$ where $T = 1$

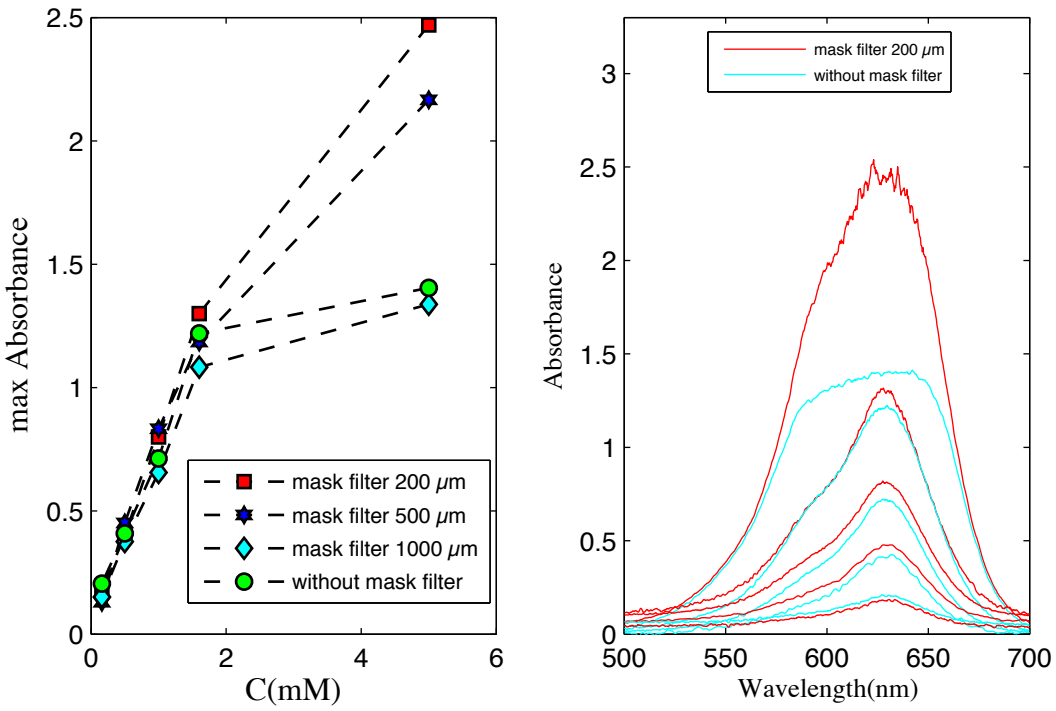

Figure 2.11: Left: experimental measurements of absorbance on chip in 4 different experimental configurations: (1) without mask filter, (2) with mask filter of 200 μm, (3) with mask filter of 500 μm, (4) with mask filter of 1000 μm. Right: absorbance spectra for different concentrations in two different experimental configurations with mask filter of 200 μm and without mask.

outside the channel and $T = T_0$ inside; T_0 is chosen arbitrarily and we will match it with the Beer-Lambert law of the dye we studied. Eventually, we integrate the total intensity passing across this composite system. There is an analytical solution of this problem and we also solve it numerically.

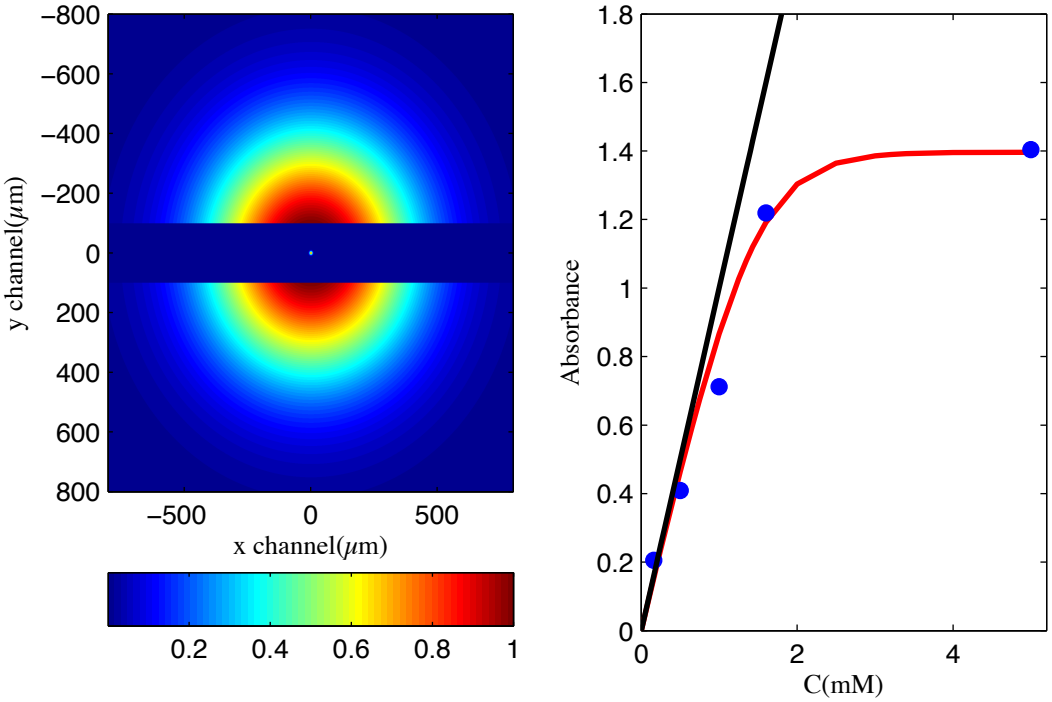

Figure 2.12: Left: composite image showing the 2-Gaussian collection zone and a channel. Right: experimental data of absorbance (blue points), previously plotted in Fig. 2.10. The dark line is the Beer-Lambert law, the red curve is the theoretical calculation using the two-Gaussian profile, see text.

Fig. 2.12, left, shows the composite image (actually the transmittance) with the illuminated area and the channel, here a totally opaque one for the sake of the example. We first see that the longest Gaussian decay is indeed very large; we also see the smallest spot (to scale) in the middle of the image. Fig. 2.12, right shows the absorbance calculated numerically on the basis of the Beer-Lambert law of the blue molecular in the channel. The agreement is good between experiments and theory, and confirms the origin of the saturation of the absorbance.

In conclusion, we have shown the limit of measurements of the instrument we developed: with standard microscope objectives, the light is collected non-homogeneously from the sample and it is difficult to really have a microspot. Some of the light comes from very far from the center of the collection zone and may contribute significantly to the measurement. This is important to know in at least two cases: when using microchannels which have a size smaller than the spatial extent of the spot (several hundreds of micrometers), and also

with large specimens which may exhibits local heterogeneities. In theses two conditions, to get a more precise measurement, it is necessary to restrict the illumination zone below the large-spot size. We achieved this using either a small field diaphragm, but it turns out to be hard to manipulate, and with masks which are placed just above the sample. The latter configuration is easy to implement but decreases the field that we can observe with videomicroscopy. In any case, there are a few advantages: the setup is straightforward to implement on any type of microscope, the spotsize is fairly $(100 - 200\,\mu\text{m})$ and it is not very costly. Eventually and importanly, in the case of small-to-moderate absorbance (say < 0.8), the large spot has no significant effect on the measurement because 95% of the intensity goes to the smallest spot and is barely attenuated. In such a case, the present setup is a real microspectrometer with a resolution of a few μm.

2.3.2 On-chip spatio-temporal microspectroscopy

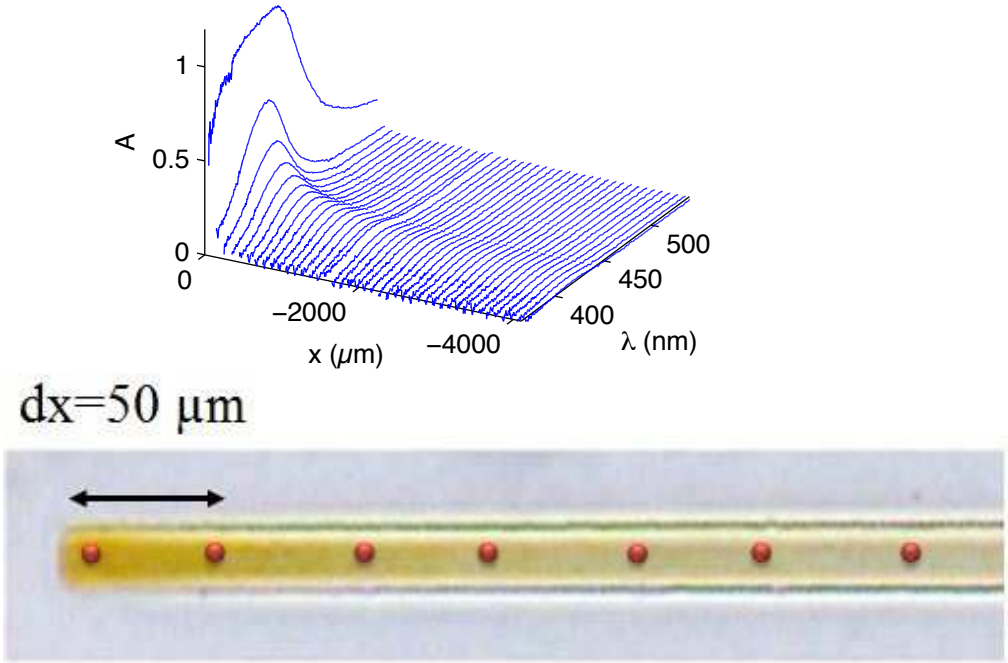

Figure 2.13: Top: 3D plot of the absorbance against space and wavelength acquired pointwise in the channel, here at a single time. Bottom: reconstructed image (at a single time) of the channel where the dots illustrate where the absorbance spectra were collected.

We illustrate the typical experiments we are going to describe in details in the next chapter. The main idea is that because microevaporation experiments are out-of-equilibrium processes, they require a screening over space and time of the process in the channel. So

far at LOF, several analytical tools have been used for this purpose: Raman microspectroscopy to extract chemical composition in time and space [27, 28], X-Ray small angle scattering to extract structural informations [21, 29]. Here, we add another tool which is simple and relevant in case of colored solutions or dispersion, such as metallic NPs.

In order to maximize the benefits of our experimental setup we have completely automated the setup: the spectrometer, the camera, and the translation stage are all controlled with a computer and a Matlab code permits us to run systematic experiments. We first choose all the parameters for the relevant parts of the setup: integration time and averaging for the spectrometer, exposure time of the camera, displacement step and range for the stage. We then run the experiment: the channel is screened over its length and the operation is iterated over time in order to build basically two main maps: absorbance and micrographs over space and time. At the end of the experiment, we run a specific Matlab routine that permits us to reconstruct the data. It is a challenging step because we generate a large quantity of data. Fig. 2.13 shows the result *at a single time* of acquisition during the process of the assembly of silver NPs. We have here a reconstructed image of the channel (the objective gives only a limited field of view of the channel) and a 3D plot of the absorbance versus wavelength and time. In the next chapter, we will make use of this setup and will evidence that the growth of materials made of NPs is not always possible. Thanks to combined videomicroscopy and microspectroscopy, we will be able to find the origin of the limiting steps in the growth of materials.

Chapter 3

Role of colloidal stability in the growth of micromaterials

We use combined microspectroscopy and videomicroscopy to follow the nucleation and growth of materials made of core-shell $Ag@SiO_2$ NPs in microevaporators. We evidence that the growth is actually not always possible, and instead, precipitation may occur during the concentration process. This event is chiefly governed by the concentration of the dispersion in the reservoir, and we assume that its origin comes from ionic species (e.g. impurities or traces of salts) that are concentrated altogether with the NPs and may alter the colloidal stability en route towards high concentration. Based on our observations, we develop a simple model that captures these phenomena and offers a stability chart that helps us in the design of a successful growth experiment.

3.1 Material and methods

3.1.1 Plasmonic NPs

Core-shell silver@SiO_2 NPs were synthetized by P. Massé in Mona Treguer's group at ICMCB, see Ref. [30] for details concerning the synthesis. TEM pictures (see Fig. 3.1) show the core-shell structure with an inner silver core of diameter (20 ± 2) nm, and a total diameter of (101 ± 5) nm, as analyzed by image processing on about 50 particles, see Fig. 3.2 for the corresponding histograms. The concentration of the initial dispersion

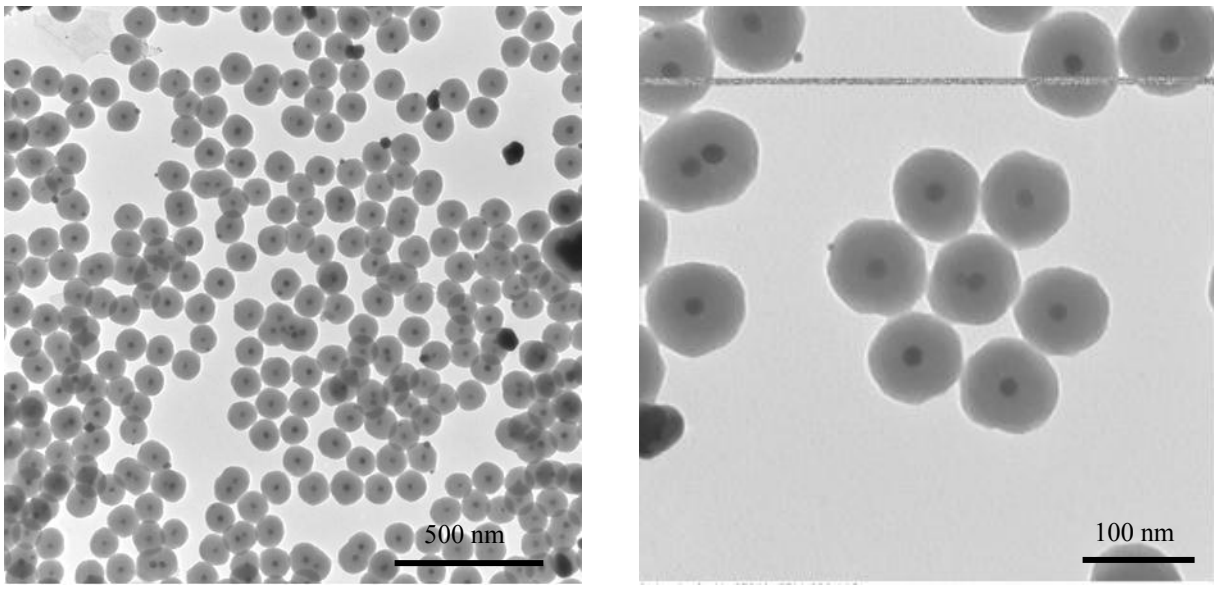

Figure 3.1: Snapshots TEM of Ag@SiO_2 NPs syntesized by P. Massé.

is relatively large, about $n = 2.15\,10^{19}$ particles/m^3, corresponding to a volume fraction $\phi_0 = nv_p \approx 1.16\%$, where v_p is the volume of a single particle as measured with the analysis of the TEM images. This value is estimated from the analysis of the TEM images, knowing the amount of chemical species used in the chemical reaction, and using bulk values for the density of silver and silica [30].

These NPs display an specific optical signature (surface plasmon resonance) that gives a sharp absorption peak in the visible range at around $\lambda = 400$ nm in water. We display in Fig. 3.3 the plasmon band measured with UV-Vis spectroscopy in a standard cuvette (1 cm), and the corresponding Beer-Lambert law. Actually, the silica shell shields the metallic core from the influence of the solvent, making them very little sensitive to the refractive index of the medium [31]. It turns out to be very convenient in order to use absorption to measure their concentration.

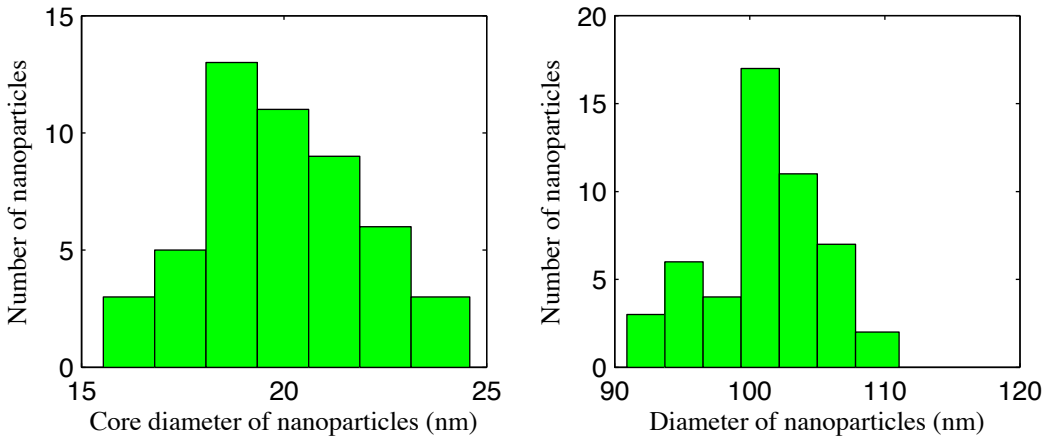

Figure 3.2: Histograms of size of Ag@SiO_2 NPs analyzed from TEM images on about 50 particles. Left: histogram for the silver core diameter ($d_{silver} = 20 \pm 2$ nm). Right: histogram for the total diameter of NPs ($D_{NPs} = 101 \pm 5$ nm).

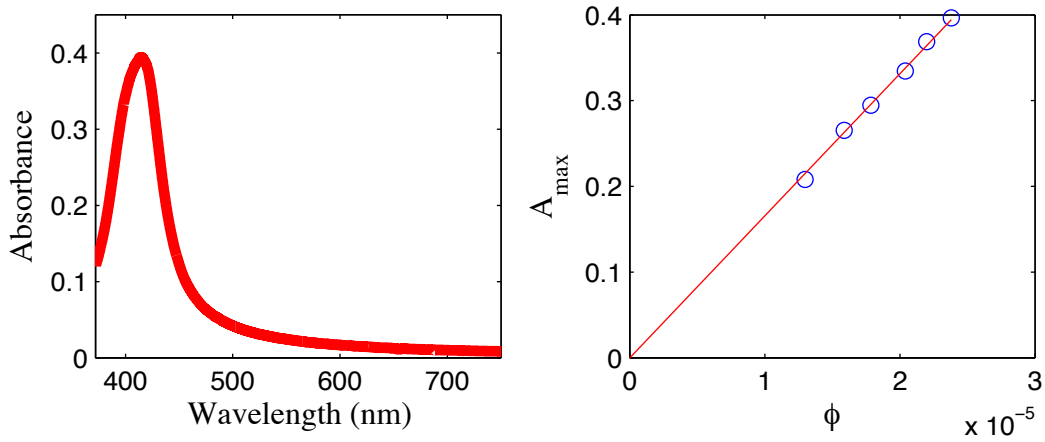

Figure 3.3: Left: UV-Visible experimental absorbance spectrum of Ag@SiO_2 NPs measured in a standard cuvette (1 cm). Right: Beer-Lambert law in the same cuvette for 5 different volume fractions (ϕ =0.0024, 0.0020, 0.0018, 0.0016, 0.0013 %)

3.1.2 Microfluidic evaporation combined with on-chip spectroscopy

We use microfluidic evaporators as shown in Fig. 1.18, page 27, that consists of 21 microchannels of different lengths L_0 connected to a reservoir of about 50 μL. The dimensions of the channels are $w = 40$ μm, $h = 10$ μm, and L_0 ranging between 0.7 and 12 mm. For such devices, evaporation times are of the order of 240 s (see Fig. 1.23, page 31). We fill the microfluidic device with the dilute dispersion at an initial time t_0. For each experiments presented in the following, we measure precisely L_0, the external humidity of the room, and we performed a calibration of the microfluidic evaporators to extract precisely the parameters T_e and V_0.

We then use the setup described in the previous chapter with a standard illumination, i.e. without any pinhole and any mask, to monitor over time and space the optical absorption during the concentration kinetics of the NPs in the microchannel. More precisely, we move the motorized stage with spatial steps of 50 μm on a specific channel of length $L_0 \approx 5$ mm, and we measure locally *both* absorbance spectra and video images on about 100 points to cover the given channel. The corresponding temporal resolution is relatively reasonable as the acquisition time of the series of spectra (integration time of the spectrometer ≈ 150 ms) over the length of the channel is of the order of 2 to 3 minutes, which remains small compared to the overall kinetics which lasts several hours. Therefore, we assume that a series of measurements along the microchannel is acquired at a single time. We repeat such a process as long as necessary.

Using the standard illumination, we remind that we can only measure locally the absorbance up to relatively small values (see Fig. 2.11, page 50). Such an experiment is thus especially meaningful in the dilute regime, but we will see that we can nevertheless and unambiguously evidence the growth kinetics which concerns, by nature, the concentrated regime. The next section illustrates typical results for the growth process.

3.2 Kinetics of concentration: observed phenomenology

3.2.1 Phenomenology from video microscopy

We first detail the experimental observations for several experiments at different initiation concentrations in the reservoir. We identified three cases depending on the initial volume fraction: (1) linear growth for high volume fractions, (2) linear growth with precipitation for intermediate volume fractions, and (3) arrested growth limited by precipitation for low volume fractions.

Linear growth

For relatively large initial volume fractions ($\phi_0 \approx 1.16\%$), we observe the following phenomenology (see the snapshots of Fig. 3.4). At the tip of the microevaporator, concentration of NPs increases as easily evidenced on the video images (the tip becomes darker and darker). At a given time, $t_N \approx 10$ min, a front separating a dense array from the

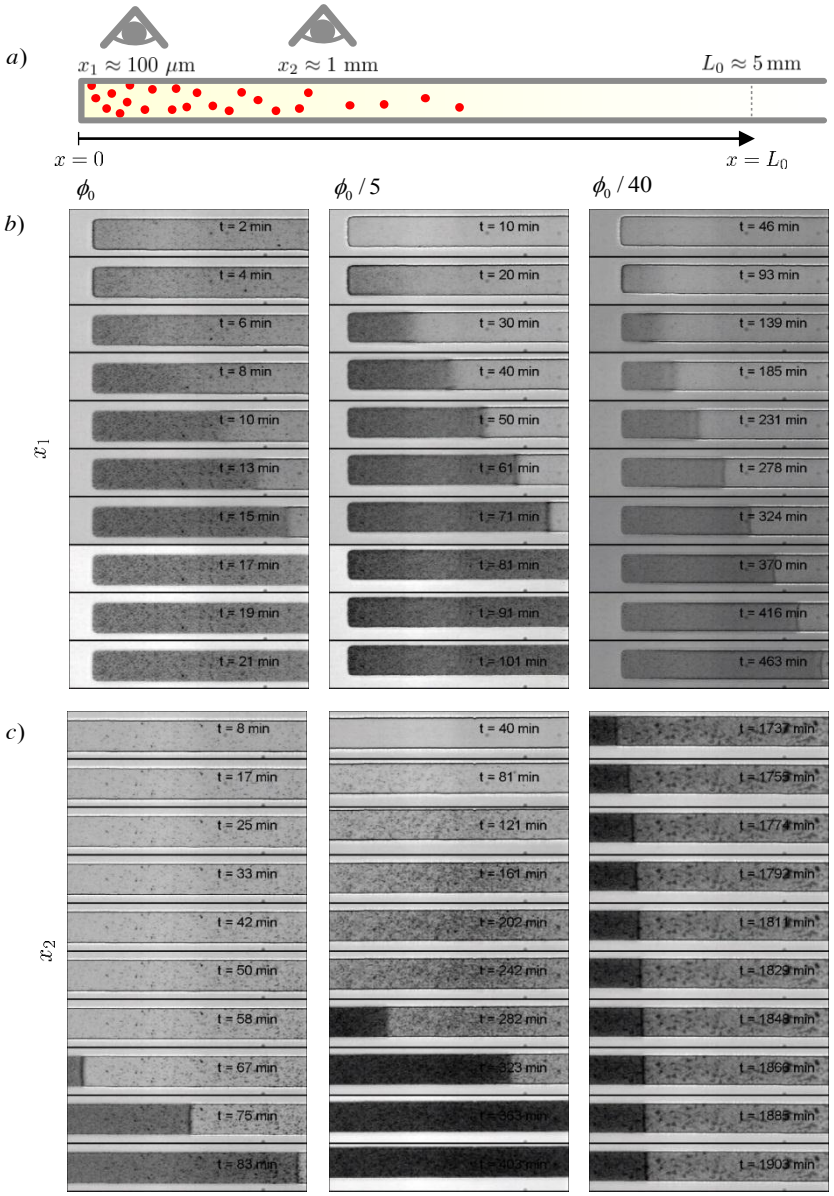

Figure 3.4: Series of images of a microevaporator (width 40 μm, $L_0 = 5$ mm) during the concentration kinetics of the Ag@SiO_2 NPs for 3 different volume fractions ($\phi_0 = 1.16\%$, $\phi_0/5 = 0.23\%$, $\phi_0/40 = 0.029\%$). a) Sketch of the microfluidic channel and the two positions x_1=100 μm and x_2=1 mm corresponding to the following snapshots. b) Snapshots at x_1 for the 3 volume fractions. c) Snapshots at x_2. For ϕ_0 we observe the nucleation/growth of a dense array. For $\phi_0/5$ we observe the precipitation of NPs at x_2 but the growth of the dense array is not stopped. For $\phi_0/40$ we observe the precipitation of NPs at x_2 that even stops the growth of the material.

dilute dispersion invades the microevaporator at a controlled pace. At later times, the growth still continues as evidenced on the snapshots taken at $x_2 \approx 1$ mm, see Fig. 3.4. These observations are very similar to the results obtained by Merlin *et al.* [20], detailed page 23, i.e. the nucleation and growth of a dense array of colloids. The texture of the dense material is quite homogeneous, and the latter displays a yellow color. We will detail below structural measurements of this dense material.

Linear growth with precipitation

For intermediate initial volume fractions ($\phi_0/5 \approx 0.23\%$), we also observe the growth of the same material, but the nucleation time is quite longer $t_N \approx 20$ min, and the growth rate of the material is considerably smaller. This is again expected from the classical conservation laws (see below for a detailed characterization) [20]. However, a new phenomena occurs. At $x_2 = 1$ mm from the tip of the channel (see the snapshots of Fig. 3.4), one can observe the formation of large aggregates that scatter efficiently light and that probably stick to the PDMS walls of the channel. This probably correspond to a localized precipitation of the incoming NPs as we will suggest below. Nevertheless, this new phenomena does not hinder the growth of the dense array for even larger size ($x > 1$ mm).

Arrested growth and precipitation

For a smaller initial volume fraction ($\phi_0/40 \approx 0.029\%$), we still observe the formation of a dense array at the tip of the channel, but for longer nucleation times, $t_N \approx 100$ min. However, precipitation of the NPs at the position x_2 becomes more and more pronounced (the images display the presence of more and more aggregates). Ultimately, the growth of the material stops, and it seems that all the incoming nanoparticles precipitate at $x \approx x_2$, and therefore did not *feed* the growth of the dense array.

Note that for more diluted initial dispersion (data not shown), we do not even observe the formation of a dense array of NPs at the tip of the channel. In this regime, it seems that all the incoming NPs precipitate at the position $x_2 = 1$ mm. For very long observation times (typically one or two days), we also observe sometimes the formation and growth of a dense and homogeneous array but starting from the position x_2 (data not shown). It seems that the continuous precipitation of the NPs at x_2 leads to a *wall* of aggregates, leading to a smaller *virtual* microevaporator with a *porous* tip at $x = x_2$. We will explain these strinking observations later in this chapter.

3.2.2 Phenomenology from local absorbance measurements

We measured 3D plots A vs. λ vs. x at different times t of the concentration process (see Fig. 2.13, page 52 for an example), with a temporal resolution of about 2-3 minutes. To exploit this large amount of data, Fig. 3.5 displays the spatial evolution of the absorbance A at two different wavelengths λ only, and for three specific times t for each initial concentration. We chose to plot the absorbance at $\lambda_p = 400$ nm corresponding to the resonance of

the surface plasmon of the core-shell NPs, and at $\lambda_s = 600$ nm where no optical signature is expected for Ag@SiO_2. Any signal measured at $\lambda_s = 600$ nm may thus reveal the strong scattering of the aggregates shown in Fig. 3.4.

Linear growth

The absorbance at the surface plasmon resonance, $A(\lambda_p)$, is a priori sensitive to the local concentration (Beer-Lambert law), at least for low values (see Sec. 2.3.1, page 47). The corresponding data $A(\lambda_p)$ vs. x. data evidences two domains for small volume fractions ($\phi_0 = 1.16\%$), i.e. in the growth regime. For large x, one observes a steady hyperbolic profile $A(\lambda_p) \sim L_0/x$ as shown by the red fits. For smaller x, one observes the saturation of the measurement at the plateau value $A = 1$ corresponding to the dense array of NPs. This saturated domain then invades the channel at longer times scales: it corresponds to the growth of the dense material along the microfluidic channel. We remind again that this saturated value comes from our optical setup that cannot measure locally high values of absorbance. A then saturates at a value close to 1, as a small portion of the illumination field is larger that the channel width (see Fig. 2.12, page 51). The absorbance at 600 nm, $A(\lambda_s)$, remains small during the initial stage of the nucleation and growth of the dense array of NPs. We observe a slight increase associated to the plateau value at 400 nm, that probably corresponds to the scattering of the dense material.

Linear growth with precipitation

For intermediate volume fractions, the observations are quite similar for $A(\lambda_p)$ except again the fact that the nucleation time is longer and the growth rate of the saturated plateau is smaller. However, a *hump* develops for $A(\lambda_s)$ in a narrow spatial range $x = 1000$–1500 μm. This hump of absorbance reveals the strong scattering (and absorption) of the large aggregates seen on the video images, see Fig. 3.4. Again, this precipitation does not hinder the growth of the dense material along the channel. We also observe that for the dense array of NPs, i.e. in the liquid dispersion, $A(\lambda_p)$ again follows a hyperbolic profile $A(\lambda_p) \sim L_0/x$.

Arrested growth and precipitation

For smaller volume fractions ($\phi_0/40 = 0.029\%$), the hump at $x = 1000$–1500 μm for $A(\lambda_s)$ becomes more and more pronounced, even during the initial stage of the nucleation and growth of the dense array at $x = 0$. For longer time scales, one observe the nucleation and growth of a saturated domain for $A(\lambda_p)$ that ultimately stops to grow in the channel. At longer times scales, the hump $A(\lambda_p)$ vs. x still continues to increase. We again observe at large x a steady hyperbolic profile (not easily evidenced using the scale of Fig. 3.5), i.e. $A(\lambda_p) \sim L_0/x$

Before we draw a scenario to explain the above results, based on the competition between the concentration process of the colloids and that of ionic impurities initially

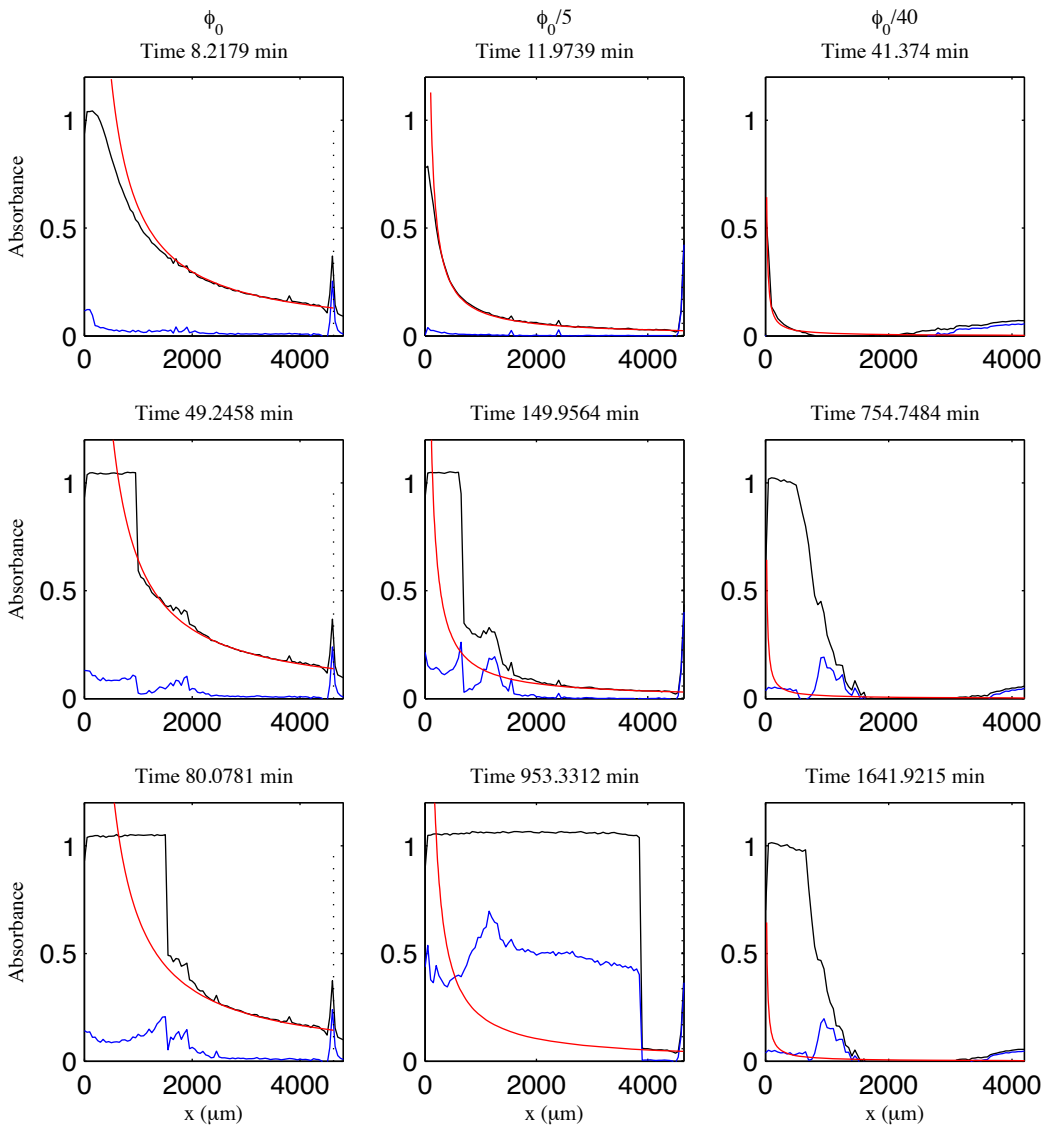

Figure 3.5: Series of measurements of absorbance during the growth of a dense state, for 3 different volume fractions ($\phi_0 = 1.16\%$, $\phi_0/5 = 0.23\%$, $\phi_0/40 = 0.029\%$) and at three different times. The black line is the absorbance measured at $\lambda_p = 400$ nm (at the surface plasmon resonance), the blue line is the absorbance measured at $\lambda_s = 600$ nm (where no optical signature is expected for Ag@SiO_2); the red line is the hyperbolic ramp ($= \alpha L_0/x$) used to fit experimental data.

dissolved in the dispersion, we detail quantitatively the growth rate and the absorbance profiles shown in Fig. 3.5.

3.3 Quantitative analysis of the concentration and growth processes

3.3.1 Model of A. Merlin *et al.*

Aurore Merlin provided during her thesis a complete description for the concentration of colloids during microevaporation, and the consequent growth of colloidal crystal, see Sec. 1.3.2, page 23 and Refs. [20, 24]. We recall briefly this model here, and we apply it to our results on Ag@SiO_2 NPs. Obviously, as this model takes into account only the colloids, and is only based on simple conservation equations, it cannot predict or explain the observed precipitation.

In the experiments shown above, $L_0 \approx 5$ mm, and the evaporation time is $T_e = 240$ s. The colloids Ag@SiO_2 have a mean diameter of 100 nm, and their Stokes-Eisntein diffusivity is about $D_c \approx 2\ \mu\text{m}^2/\text{s}$. The Péclet number of the experiment shown above is thus $\text{Pe}_c = L_0^2/(D_c T_e) \approx 5\,10^4$ and therefore very large. One can thus consider as done by A. Merlin, that diffusion is indeed negligible and that colloids are only convected in the channel. Concentration profiles before the nucleation of the dense array, thus follow (see Sec. 1.2.3, page 18):

$$\begin{aligned} \phi(x,t) &= \phi_0 \exp(t/T_e) \quad \text{for} \quad \phi(x,t) < \phi_0 L_0/x, \\ \phi(x,t) &= \phi_0 \frac{L_0}{x} \quad \text{for} \quad t > -T_e \ln(x/L_0). \end{aligned} \tag{3.1}$$

This continuous increase at the tip of the channel stops when $\phi(x,t) = \phi_d$ where ϕ_d is the maximal compaction of the colloids. This occurs at a time t_N and for a position x_N given by $x_N = L_0(\phi_0/\phi_d)$, $t_N = T_e \ln(\phi_d/\phi_0)$. Later, the dense array invades the channel and the growth rate is given by the conservation of solute. A. Merlin suggested (and verified experimentally on the growth process of colloidal crystals made of polystyrene beads) that evaporation of water still continues in the dense colloidal array, i.e. the dense array is *porous enough* to permit flows inside it. In that case, concentration profiles are given by:

$$\phi(x,t) = \phi_d \quad \text{for} \quad x < x_d, \tag{3.2}$$

$$\phi(x,t) = \phi_0 \frac{L_0}{x} \quad \text{for} \quad x > x_d\,, \tag{3.3}$$

where x_d is the position of the dense array in the channel. Solute conservation implies in that case:

$$\frac{\phi_d}{\phi_0}\frac{x_d}{L_0} - 1 - \log\left(\frac{x_d}{L_0}\frac{\phi_d}{\phi_0}\right) = \frac{V_0}{L_0}(t - t_N). \tag{3.4}$$

see page 25 for a more complete demonstration. For $\phi_0 \ll \phi_d$, the growth is linear and simply given by:

$$\frac{\phi_d}{\phi_0}\frac{x_d}{L_0} \approx \frac{t - t_N}{T_e}. \tag{3.5}$$

3.3.2 Comparison with our measurements

Nucleation and steady hyperbolic profile

In the model of model of A. Merlin *et al.*, the nucleation time does not depend strongly on the initial concentration $t_N = T_e \ln(\phi_d/\phi_0)$. In our experiments, we measure approximatively $t_N \approx 10$ min for $\phi_0 \approx 1\%$, $t_N \approx 20$ min for $\phi_0/5$ and $t_N \approx 100$ min for $\phi_0/40$ (with large uncertainties, see Fig. 3.4). The model predicts for $\phi_d = 0.64$ (random close-packed monodisperse spheres): $t_N \approx 16$ min, $t_N \approx 22$ min, and $t_N \approx 30$ min for the same initial volume fractions. The agreement is not perfect, but we remind again that the initial volume fraction of our dispersion is not perfectly known (only measured using TEM images and knowning the mass of chemical species used in the synthesis [30]). The discrepancy may also come from the fact that the microevaporators are not ideal, as a "'leakage velocity"' is measured at $x = 0$, and corresponding to the pervaporation of water at the tip of the channel in the bulk PDMS matrix, see Fig. 1.23, page 31.

Nevertheless, our absorbance measurements provide a new proof for this model because we measure spatially-resolved concentration profiles along the microfluidic channel. Indeed, Fig. 3.5 clearly shows that the absorbance measurements in front of the dense array, follows a steady hyperbolic profile $A \sim 1/x$, as in the above equations.

Figure 3.6 shows a typical measurement (before the nucleation of the dense material) and the fit by $A = A_0 L_0/x$. The wavelength λ for such measurements correspond to $\lambda_p = 400$ nm, the surface plasmon resonance. The agreement is correct, especially for large x, i.e. for moderate values of A as expected since our illumination prevents us to measure large absorbance. Figure 3.6(bottom) shows the same measurements, but with A against L_0/x. This is a *microfluidic equivalent* of the Beer-Lambert law. Indeed, if the initial volume fraction is perfectly known, this curve gives the absorbance as a function of the concentration, and thus the extinction coefficient (for a known height of the microfluidic channel).

In our measurements done for several initial volume fraction $\phi = \phi_0/d$ with $d = 1$, 5, and 40, we fit in each case the hyperbolic profile by $A_0 L_0/x$. Figure 3.6 right, displays A_0 vs. $1/d$ i.e. the concentration in the reservoir. The linear correlation indicates again that our measurements provide a way to measure the Beer-Lambert law from the steady hyperbolic profile in a microevaporator.

Growth of the dense array

From our spatio-temporal measurements of the absorption spectra, it is straightforward to extract images of the growth process. Figure 3.7 shows 2D images x vs. t of the absorbance

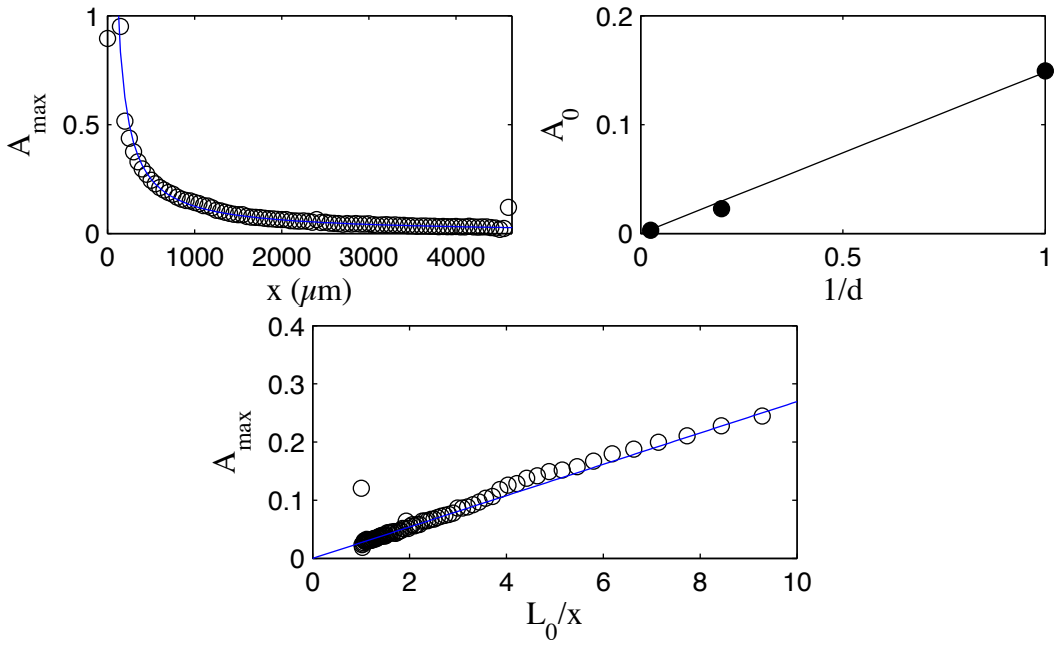

Figure 3.6: Top: (left) Absorbance measured in the channel (width 40 μm, $L_0 \approx 5$ mm) for $\phi_0/5 = 0.23\%$, black circles are the experimental measurements and the blue curve is the hyperbolic ramp $A_0 L_0/x$, $A_{\max}$ is the absorbance at $\lambda_p = 400$ nm. (right) Absorbance A_0 measured using the fit of the hyperbolic profiles against 4 dilutions d of the initial volume fraction. Bottom: same data as top, left but plotted against L_0/x, it corresponds to the Beer-Lambert law measured on the chip.

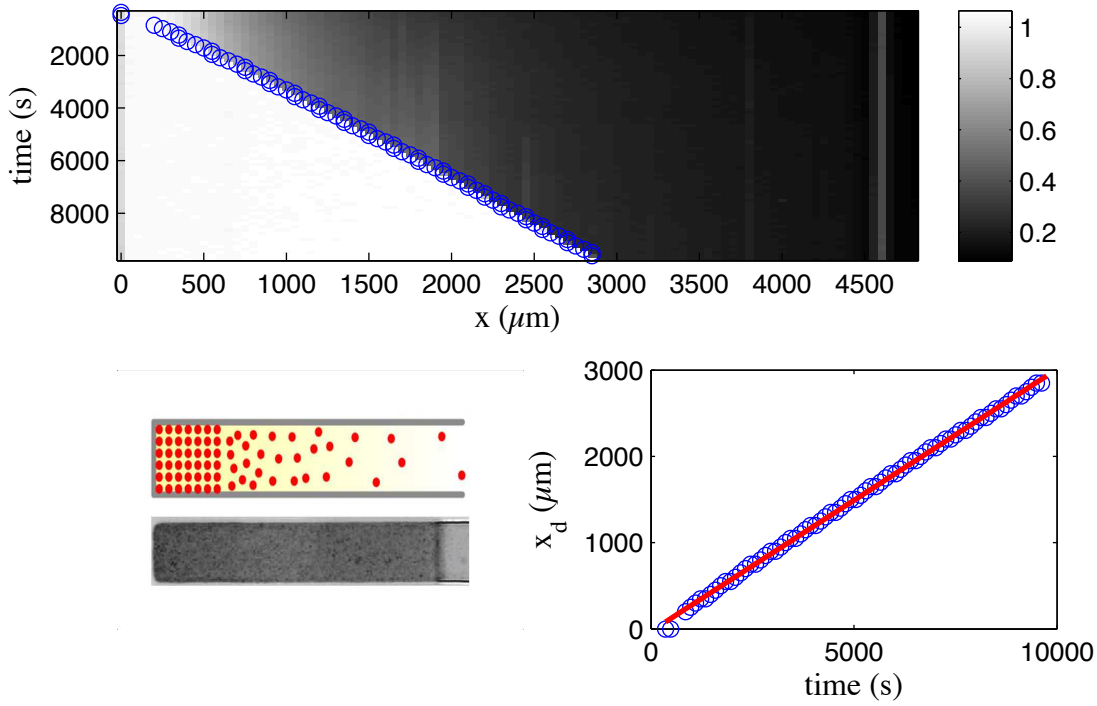

Figure 3.7: Growth of the dense material in the channel (width 40 μm, length $L_0 = 5$ mm) for ϕ_0 =1.16%. Top: space-time plot of absorbance $A(\lambda_p)$. Bottom: measured position of the front x_d against time t (blue circle), the red line is a linear fit to evaluate the velocity of dense front. Bottom left: sketch of the formation of a porous dense array, and corresponding video image.

$A(\lambda_p)$ measured at the surface plasmon resonance for a given experiment (ϕ_0 =1.16%). This 2D image reveals thanks to the saturated domain ($A \approx 1$), the position of the front of the dense array x_d vs. t.

The same figure (bottom) shows x_d vs. t, and evidences a linear growth of the solid region, as expected from the solute conservation Eq. (3.5), in the case of $\phi_0 \ll \phi_d$. Figure 3.8 shows the same measurement but for 4 different dilutions (1, 5, 20 and 40). Note that for the largest dilution, the growth of the dense array stops due to the precipitation of NPs at $x \approx x_2$ and we limit our analysis in this case to the first 600 μm of growth.

The same figure shows the same results but rescaled by t/T_e and $x_d/(\phi_0 L_0)$ as suggested by the natural variables of Eq. (3.5). This plot clearly shows the collapse of all the data, and thus the validity of Eq. (3.5). Note that the nucleation time does not seem to play a significant role, and this is probably due to the large dilutions investigated combined with the long time scales probed (t/T_e up to 200). We also observe that the curve for the highest dilution deviates significantly from the 3 other curves. This may be due to the reproducibility of our measurements, and/or to the fact that in this dilute case, the growth rate is probably perturbed by the precipitation pheneomena (see above). The linear fit of such data a priori leads to the value ϕ_d, see Eq. (3.5), page 64. In our case, such a fit leads to the unrealistic value $\phi_d = 1.8 \pm 0.2$. We believe that this discrepancy mainly come the value ϕ_0 which is a priori not known precisely. We can even claim that for $\phi_d \approx 0.64$, which is a good estimate as shown below thanks to our structural measurements see Fig. 3.12, the initial concentration of the dispersion is probably more diluted than expected and $\phi_0 \approx 0.4\%$.

The inset of Fig. 3.7 shows the velocity of the front v_d, i.e. the growth rate of the dense material against the dilution of the initial dispersion. For the highest concentration, the growth rate is of the order of 300 nm/s. We also tested similar measurements for different lengths L_0 of channels (thanks to the device shown Fig. 1.18, page 27, L_0 = 0.7–12 mm) and we verify that the growth rate is indeed proportionnal to L_0 (data not shown). For the highest concentration, and the longest channel $v_d \approx 0.7$ μm/s.

3.4 A simple model for precipitation versus growth

We have shown that our microevaporators can increase the concentration of colloidal species in a controlled way, up to the formation and growth of a dense array of nanoparticles within the microfluidic channel. This scenario holds only if no "accident" such as precipitation or aggregation occurs en route toward high concentration of colloids (see Fig. 3.4, page 59). The theoretical scenario provided by A. Merlin *et al.* concerned pure binary systems (water + colloids), which is unrealistic because most of the colloidal dispersions contains pollutants solubilized in water which may play the role of destabilizing agent. As we are working with dilute dispersions of NPs (0.001–1%), what matters is how much pollutant is present in the initial dispersion because even traces might play a significant role upon concentration. Indeed, our evaporation-based device leads to an increase of the concentration of all species (although at different rates), and the localized increase of pollutant may well induce the

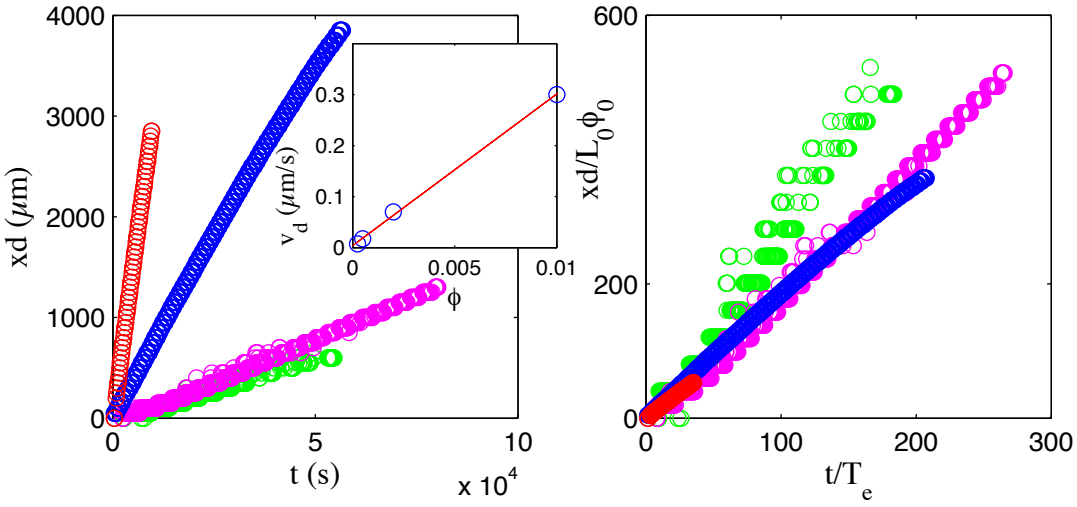

Figure 3.8: Left: different series of growth kinetics collected on the same microchannel for 4 different volume fraction ($\phi_0 = 1.16\%$, $\phi_0/5 = 0.23\%$, $\phi_0/20 = 0.08\%$ and $\phi_0/40 = 0.029\%$). Right: rescaling of the front position $x_d/(L_0\phi 0)$ against reduced time t/t_e. Inset: velocity of front v_d (blue circle) against the 4 different volume fractions, the red line is a linear fit.

aggregation of the dispersion.

Actually, our aqueous Ag@SiO_2 dispersion contains probably dissolved ionic species, such as traces of salts. Microevaporation concentrates both colloids and ions, thus leading to a possible electrostatic destabilization of the dispersion during the concentration process. However, the general theoretical description of the concentration process of such a ternary system probably needs complex theoretical derivations that are far beyond the scope of the present thesis. Because our aim is explain only *qualitatively* the above results, we make use of several simplifying assumptions described below.

Note that the following section has been published in the Supporting Information of Ref. [32] which is presented in the next chapter.

3.4.1 Assumptions of the model

Uncoupled dynamics

First, we assume that there are no couplings between the dynamics of concentration of the colloids and that of the ionic species, except of course for the possible destabilization of the dispersion at a critical salt concentration. Actually, we do not refer to ions that define the ionic cloud around the particles, and which is bound to particles but the excess of ions that define the ionic strength of the medium.

Pervaporation-Induced Flow

Then, we assume that the permeation-induced flow is not altered by the presence of the NPs. This is largely the case for colloidal dispersions, even at high concentration as the dense porous array always contains a *lot of space* for the water molecules. In other words, the large difference of volumes between a water molecule and a NP prevents the colloids to decrease significantly the chemical potential of water, and thus to slow down the evaporation rate [33].

Moreover, we also assume that the local increase of ionic species does not slow down the evaporation rate which actually remains only valid up to a moderate ionic concentration. In our experiments, it translates into a duration as ions are continuously concentrated in the microevaporator. This regime is however often encountered in the experiments, as it requires a high salt concentration to decrease significantly the water activity (e.g, the water activity of a 50 mM NaCl solution is about 0.9) [34].

3.4.2 Concentration dynamics and destabilization

We use dimensionless variables to describe the concentration process where the linear dimension of the evaporator is normalized with its total length L_0, the time by the evaporation time T_e, and the concentrations by the ones in the reservoir: volume fraction ϕ_0 for colloids, concentration c_0 for the salts.

The concentration dynamics of the colloids is mainly dominated by convection (infite Péclet number) and follows the two steps described previously by Eqs. (3.1)–(3.5), page 64 (model of A. Merlin *et al.*).

The dynamics of concentration of the ionic species follows a different kinetics because diffusion plays a more important role. We assume a constant diffusion coefficient $D_s \approx 2\,10^3\ \mu\mathrm{m}^2/\mathrm{s}$, leading to moderate Péclet numbers Pe in the 250–1000 range. Note that for the experiment detailed above, the accumulation box for the salt is $p = \sqrt{DTe} \approx 0.7$ mm. This new scale corresponds, as shown below, to the position $x_2 \approx 1$ mm, see Fig. 3.4, page 59, where we observe the precipitation of the incoming NPs.

In the continuous concentration regime (see Eq. (1.26), page 20), the concentration field of salts follows for $X < 1/\sqrt{\mathrm{Pe}}$ [22]:

$$C(X,T)/C_0 = \sqrt{\frac{2\mathrm{Pe}}{\pi}} \exp\left(-\frac{\mathrm{Pe}X^2}{2}\right)(T-\tau^\star) + \sqrt{\mathrm{Pe}}\,, \tag{3.6}$$

and

$$C(X,T)/C_0 = 1/X \quad \text{for} \quad X > 1/\sqrt{\mathrm{Pe}}\,. \tag{3.7}$$

These relations give correct approximations of the concentration process, and are valid only after a transient regime i.e. for $T > \tau^\star = \log(\mathrm{Pe})/2$, see page 20 for more details and Ref. [22].

Note also that the typical size involved in the dynamical concentration gradient is given by $\sqrt{DT_e}$ and is therefore quite larger for salt than for colloids, which explains why they do not get concentrated at the same rate.

We now introduce a key ingredient to explain our experimental observations. We assume that when the salt concentration locally reaches a critical concentration $C^\star$ during a microevaporation experiment, the convected colloids loose their stability, stick on the PDMS wall of the channel and accumulate at this position as continuously fed from the pervaporation-induced flow. Note that this critical concentration may correspond to the stability threshold observed for the bulk dispersion, or to the stability of the colloids against the PDMS wall. Again, this simple assumption hides a large complexity, that of the destabilization of *convected* colloids in a *confined* geometry, but as seen below it helps us to give simple guides to engineer micromaterials and rationalize our observations.

3.4.3 Different regimes of destabilization

Different regimes may now be rationalized from the competition between the concentration process of the colloids and that of the ionic species. Colloids are mainly convected up to the tip of the microevaporator following Eq. (3.1), and then a dense assembly may grow and invade the microevaporator [see Eq. (3.4)]. This expected regime may not occur due to the continuous increase of the ions following Eq. (3.6) in a box of size $1/\sqrt{\mathrm{Pe}}$. We can now classify the different regimes, that depend on the Péclet number of the ions, and importantly on the relative concentrations ϕ_0/ϕ_d and $C_0/C^\star$.

En route destabilization

The first regime corresponds to the destabilization of the convected colloidal dispersion before the nucleation and growth of the dense state. This regime thus occurs in case where the concentration of ions increases at the tip of the microevaporator beyond $C^\star$ before the nucleation time τ_N of the dense assembly. This leads to the following criteria to observe this regime $C(X=0,\tau_N) > C_s$, yielding more precisely the relation:

$$\sqrt{\frac{2\mathrm{Pe}}{\pi}}\left(\log\frac{\phi_d}{\phi_0} - \frac{\log \mathrm{Pe}}{2}\right) + \sqrt{\mathrm{Pe}} > \frac{C^\star}{C_0}\,, \tag{3.8}$$

When this condition is fulfilled, the salt concentration increases beyond $C^\star$ before the nucleation of the dense assembly. The colloids first precipitate at the tip of the microevaporator (where the salt concentration is higher), then as the gaussian concentration profile of salts still linearly increases in time [Eq. (3.6)], colloids now accumulate due to their precipitation at a position which is roughly given by $X \sim 1/\sqrt{\mathrm{Pe}}$. In our work, precipitation is observed at a position $x_2 \approx$ 1–1.5 mm, which compares correctly to the size of the accumulation box $p \sim \sqrt{DTe} \approx 0.7$ mm.

This exact scenario is observed in some experimental cases investigated in the present work, especially for very low dilutions ($\approx 1/200\%$, data not shown), and mostly when the ratio $C^\star/C_0$ is low and for long microevaporators (the above relation indeed depends weakly

on ϕ_0). This regime is illustrated in Fig. 3.9 thanks to a combined numerical resolution of the microevaporation equation for the salt, and its superposition with the analytical approximations given by Eqs. (3.1) and (3.7).

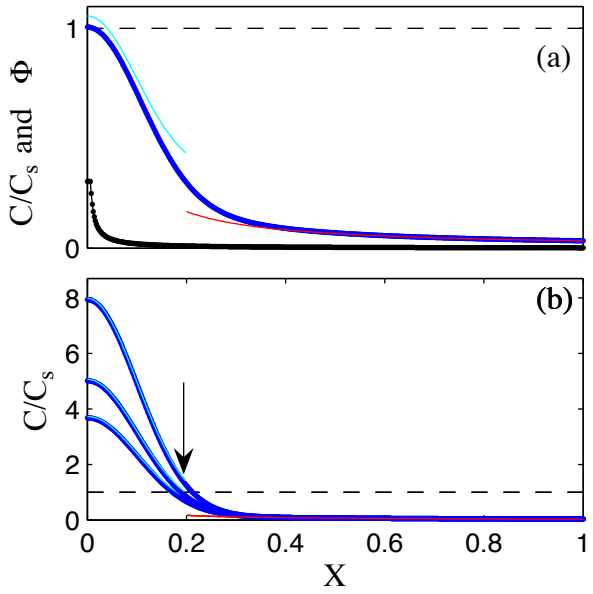

Figure 3.9: (a) Sketch of the first regime, thanks to combined numerical resolution of the microevaporation equation for the ions (blue dots), and the theoretical concentration profiles for the colloids [black dots, Eq. (3.1)]. The red curve is the approximate hyberbolic branch Eq. (3.7), and the cyan curve the gaussian approximation Eq. (3.6). In that case, $T = 5$, Pe $= 100$, $C^\star = 30\,C_0$, $\phi_0/\phi_d = 0.002$ and $\phi_d = 1$. The concentration of salt reaches $C^\star$ at the tip of the channel, before the nucleation of a dense assembly. (b) Further concentration profiles for the ionic species, the black arrow indicates the position where the convected colloids accumulate ($T = 15$, 20 and 35).

Favorable conditions of nucleation and growth

In this regime, which is highly expected for the manufacturing of our materials, the convected colloids never encounter locally a salty environment above $C^\star$. The previous condition is thus not fulfilled, and a dense assembly grows from the tip of the microevaporator in a small salt concentration environment $C(X,T) < C^\star$. Then the growth pace of the material is given by Eq. (3.4) except when the salt concentration increases up to $C^\star$.

Fortunately, and this is one of the most key issue of our experiments, the salt concentration profile always increases in time, except for positions $X > 1\sqrt{\text{Pe}}$ where convection also dominates the ions, and prevent their accumulation [steady hyperbolic branch, see Eq. (3.7)]. The condition for a favorable nucleation/growth/invasion of a dense assembly is thus only fulfilled when the salt concentration at $X \sim 1/\sqrt{\text{Pe}}$ does not reach $C^\star$ before

the dense front reaches the same position $X_d(T_d) = 1/\sqrt{\mathrm{Pe}}$ see Fig. 3.10 for a schematic view of this regime.

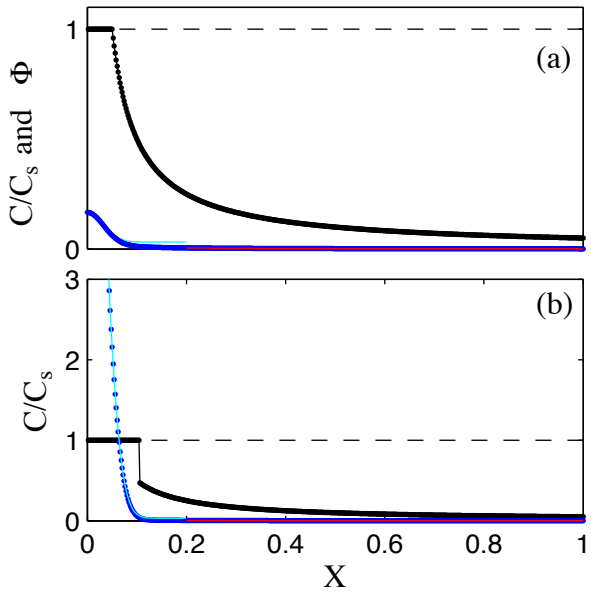

Figure 3.10: Sketch of the second regime, thanks to combined numerical resolution of the microevaporation equation for the ions (blue dots), and the theoretical concentration profiles for the colloids [black dots, Eqs. (3.2)–(3.4)]. The red curve is the approximate hyperbolic branch Eq. (3.7), and the cyan curve the gaussian approximation Eq. (3.6). In that case, $\mathrm{Pe} = 1000$, $C^\star = 1000\, C_0$, $\phi_0/\phi_d = 0.05$ and $\phi_d = 1$. (a) $T = 3\tau_N$ the dense assembly nucleates in a low salt environment. (b) $T = 100\tau_N$: the dense assembly invades the microevaporator always in a low salt environment, note that the concentration of ions still increases but only at the tip inside the permeable colloidal assembly.

This time scale is given by:

$$T_d = \frac{\log(\mathrm{Pe})}{2} + \frac{\phi_d}{\phi_0\sqrt{\mathrm{Pe}}} - 1\,. \tag{3.9}$$

and the condition reads:

$$\sqrt{\frac{2\mathrm{Pe}}{\pi}}\exp\left(-\frac{1}{2}\right)\left(\frac{\phi_d}{\phi_0\sqrt{\mathrm{Pe}}} - 1\right) + \sqrt{\mathrm{Pe}} \ll \frac{C^\star}{C_0}\,, \tag{3.10}$$

In most experimental cases investigated in the present work, $\mathrm{Pe} = 250$–1000, $\phi_d \approx 1$, and the dispersions are very diluted so that $\phi_0 \ll \sqrt{\mathrm{Pe}}$. The previous relation thus now leads to the simple condition:

$$\frac{C_0}{C^\star} \ll \phi_0\,. \tag{3.11}$$

Importantly, this condition does not depend on the length of the microevaporator, but only on the relative concentrations of salt and colloids in the reservoir, as compared to the stability threshold $C^\star$. When dispersions are too dilute (small ϕ_0), and/or when they contain too much ions (high C_0) and/or when they are easily destabilized (low $C^\star$), classical microevaporation may not lead to the formation of a dense assembly that invades the microevaporator.

Intermediate regime

When the condition (3.8) is fulfilled, a dense assembly nucleates at the tip of the microchannel, in a low salt environment (below the destabilization threshold $C^\star$). This colloidal assembly only invades the length of the microevaporator when the condition (3.11) is fulfilled. If not the case, colloids start to accumulate at a position $X \sim 1/\sqrt{\mathrm{Pe}}$ as the salt concentration profile increases up to $C^\star$ and the growth of the dense assembly stops. This regime has been evidenced experimentally in our experiments, see Fig. 3.4 for the case $\phi \approx 0.029\%$. Sometimes, as the colloids accumulate at $X \sim 1/\sqrt{\mathrm{Pe}}$, they form a porous aggregate and a dense assembly can nucleate and invade the microchannel from this position, in a low salt environment as ions are still convected through the colloidal network.

3.4.4 Stability chart

We can summarize the above calculations thanks to a stability chart, displayed Fig. 3.11. This figure delineates the two limiting cases (en route destabilization vs. growth and invasion) as a function of the volume fraction ϕ_0 of of the dispersion and the concentration of salt c_0 in the reservoir. All the three regimes have been observed experimentally, see Fig. 3.4, page 59. To compute this stability chart, we use the arbitrary values $Cs = 20$ mM and $\phi_d \approx 0.64$.

Importantly, the growth-only upper boundary does not depend on the Péclet number of colloids and reads:

$$\frac{C_0}{C^\star} \ll \phi_0 \,, \tag{3.12}$$

where C_0 and ϕ_0 are the respective concentrations of ionic species and NPs, and C_s the concentration at which the dispersion becomes unstable. For typical charge-stabilized systems, $C_s \approx$ 10–100 mM, and thus this simple rule gives an estimate of the minimal volume fraction to fabricate easily a material with our technique. For instance, when $\phi_0 \approx 1\%$, the amount of ionic impurites should not exceed 0.1–1 mM. For very dilute dispersions, e.g. $\phi_0 \approx 0.01\%$ this leads to the drastic condition $C_0 <$ 1–10 μM.

As an intermediate conclusion, we point out the crucial importance of the presence of salts in most of the colloidal dispersions, that can lead to unwanted precipitation phenomena, as soon as the local concentrations are increased by the evaporation of the solvent. This is a common situation in the wide field of drying of colloidal dispersions (sessile droplets [35], unidirectional drying [36]...), and we believe it can play an important role.

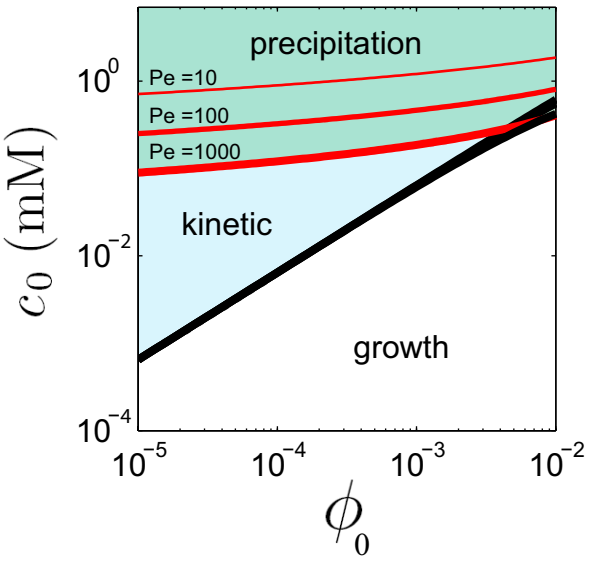

Figure 3.11: stability chart giving the outcome of the concentration process (growth of a solid, precipitation of NPs) depending on the volume fraction of NPs and the concentration c_0 of ion species in the reservoir. The present chart is calculated for charge-stabilized NPs, which become unstable above a critical salt concentration $C_s = 20$ mM; Pe in the figure stands for the Péclet number of the salt, the one of NPs being considered nearly infinite.

3.5 Qualitative analysis of the structure of the material

We perform simple qualitative measurements of the structure of the dense material enginereed, using Scanning Electron Microscopy SEM. Note that we performed such analysis on the dry material, i.e. after complete evaporation of the water from the microfluidic channel. The corresponding structure is probably affected by this final stage of drying, and we recall that in the experiments detailed above, the dense array remains wet. We proceed more precisely as follows. First, we peel off the membrane of the microfluidic evaporators using claws (as the ones typically used for SEM/TEM analysis). We then stamp the micromaterials onto a conductive tape previously stuck on a metallic pin for SEM. This transfer process is very efficient, but also intrusive since the final material sometimes breaks in small pieces. We then image the material using high-resolution SEM.

A typical example at different magnifications is displayed Fig. 3.12. The linear structures (Fig. 3.12a) that resulted from the microevaporation process could be recognized, yet cracks evidence that the material was degraded during the transfer. A closer SEM view (Fig. 3.12b) shows that the structure was indeed 3D, finely replicating the shape of the microfluidic channel. An even closer view from the top surface of the dense structure (Fig. 3.12c) highlights the high degree of nanoparticle packing with a surface roughness of the same order as that of the nanoparticle size. A further magnification of the top plane in back scattering (Fig. 3.12d, top) mode evidenced the location of the silver cores while

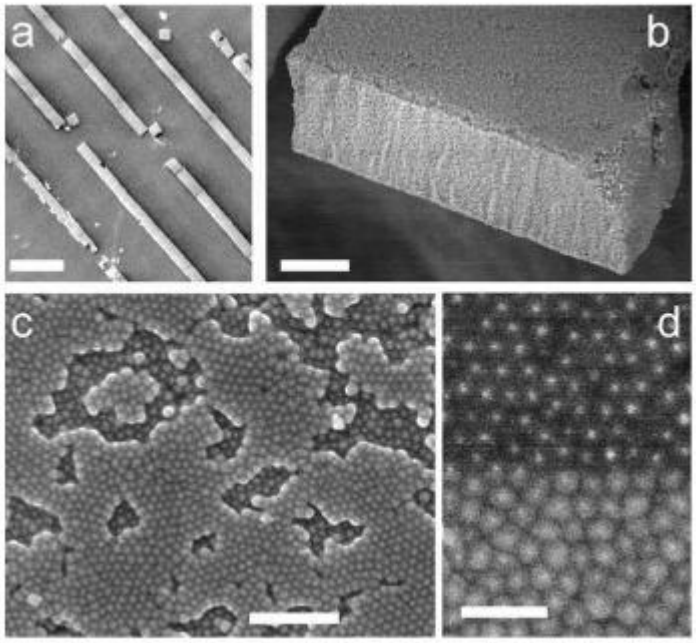

Figure 3.12: SEM characterization of the 3D nanoparticles assemblies after removal of the membrane. The dense material is stuck onto a SEM substrate and imaged at several degree of magnification (a) far view of the 3D Ag@SiO2 nanoparticles networks; scale bar =100 μm. (b) Scale bar = 10 μm. (c) Top-view of the surface of the dense material. Scale bar = 1 μm. (d) Composite SEM image in back-scattering (top) and direct (bottom) imaging modes showing the silver cores. Scale bar = 0.1 μm

direct imaging (Fig. 3.12d, bottom) strongly suggests that the silica shell underwent some faceting during the concentration process and/or during the final stage of drying.

The structural characterization of the lattice was investigated by calculating the pair correlation function (data now shown, see Ref. [30]). The analysis demonstrates that the nanoparticles underwent some degree of compression during drying and shows that the lattice is amorphous rather than perfectly crystalline. This could be due to the concentration process that is rapid and may prevent crystallization or the size distribution that is slightly polydisperse.

Chapter 4

Microfluidic-induced growth and shape-up of three-dimensional extended arrays of densely packed nanoparticles

In the present chapter, I *paste* a publication that has been accepted during my thesis in ACS Nano [32]. The present paper presents in details microfluidic evaporation experiments to engineer various densely packed 3D arrays of NPs, as for the case of $Ag@SiO_2$ detailed in the previous chapter. We indeed successfully fabricate dense arrays of different NPs: gold nanoparticles stabilized by a PEG corona (15 nm and 60 nm in diameter), monodisperse SiO_2 spheres (80 nm), gold nanorods, mixtures, and even nanoraspberries $SiO_2@Ag@SiO_2$. All these experiments have been done by Julie Angly and myself at LOF, and the various dispersions were synthesized by the partners of the METACHEM consortium.

My main contributions for the present work are the following. (i) Manufacturing of specific microfluidic evaporators, especially with very long L_0 ($>$ cm) to concentrate very dilute dispersions, and 3D microevaporators as the one shown Fig. 5(g-h); (ii) I performed and monitored several of the experiments reported. (iii) I performed some of the SEM analysis when we successfully engineered a micromaterial. (iv) For very dilute dispersions (and/or with a low stability threshold), I develop a new method to get rid of the ionic species, see Fig. 7. Briefly, I first concentrate a dense array of latex beads (200 nm diameter) of approx 2 mm at the tip of the evaporator. Then, I concentrate the targeted NPs in the same evaporator. As the latex assembly is porous, all the ionic species get concentrated inside the latex bed at the tip of the channel, and a dense array of the targeted NPs grows in a low salt environment. This is a microfluidic equivalent of a *filtration* process

The present paper also reports briefly the theoretical description given in the previous chapter, as well as the discussion concerning the stability criterion. this paper also reports the growth process in the case of core-corona NPs (such as Au@PEG), for which the growth process is radically different. We indeed observe in such cases, a slowing down of the growth rate of the dense array, which is easily explained by the fact that the dense array is not porous, and thus stops the evaporation.

Microfluidic-Induced Growth and Shape-Up of Three-Dimensional Extended Arrays of Densely Packed Nanoparticles

Julie Angly,[†] Antonio Iazzolino,[†] Jean-Baptiste Salmon,[†] Jacques Leng,[†,*] Sivasankaran Prathap Chandran,[‡,¶] Virginie Ponsinet,[‡] Anthony Désert,[§] Aurélie Le Beulze,[§] Stéphane Mornet,[§] Mona Tréguer-Delapierre,[§] and Miguel A. Correa-Duarte[⊥]

[†]Laboratoire du Futur, Université de Bordeaux, UMR 5258, F-33600 Pessac, France, CNRS, Laboratoire du Futur, UMR 5258, F-33600 Pessac, France, and RHODIA, Laboratoire du Futur, UMR 5258, F-33600 Pessac, France, [‡]Centre de Recherche Paul-Pascal, Université de Bordeaux, UPR 8641, F-33600 Pessac, France, and CNRS, Centre de Recherche Paul-Pascal, UPR 8641, F-33600 Pessac, France, [¶]Department of Chemistry, Sri Sathya Sai Institute of Higher Learning, Prasanthi Nilayam Campus, Puttaparthi, Anantapur district, Andhra Pradesh - 515134, India, [§]Institut de Chimie de la Matière Condensée, Université de Bordeaux, UPR 9048, F-33600 Pessac, France, and CNRS, Institut de Chimie de la Matière Condensée, UPR 9048, F-33600 Pessac, France, and [⊥]Departamento de Quimica Fisica, Universidad de Vigo, 36310 Vigo, Spain

ABSTRACT We use evaporation within a microfluidic device to extract the solvent of a (possibly very dilute) dispersion of nanoparticles and concentrate the dispersion until a solid made of densely packed nanoparticles grows and totally invades the microfluidic geometry. The growth process can be rationalized as an interplay between evaporation-induced flow and kinetic and thermodynamic coefficients which are system-dependent; this yields limitations to the growth process illustrated here on two main cases: evaporation- and transport-limited growth. Importantly, we also quantify how colloidal stability may hinder the growth and show that care must be taken as to the composition of the initial dispersion, especially regarding traces of ionic species that can destabilize the suspension upon concentration. We define a stability chart, which, when fulfilled, permits us to grow and shape-up solids, including superlattices and extended and thick arrays of nanoparticles made of unary and binary dispersions, composites, and heterojunctions between distinct types of nanoparticles. In all cases, the geometry of the final solid is imparted by that of the microfluidic device.

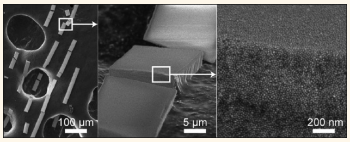

KEYWORDS: densley packed nanoparticles · microfluidic-induced growth · extended arrays

Clusters, crystals, or extended arrays of nanoparticles (NPs) display promising properties which, upon integration into devices, will promote the development of new technologies[1] and already pave the way to new paradigms.[2,3] Among many possible structures, crystals of nanocrystals (superlattices, SLs) are currently attracting an ever increasing research effort. SLs can be solution-processed, which is a key point for industrial up-scaling. They display crystalline structures which overcome by far their atomic analogues with, for instance, lattices that have no equivalent in nature.[4] Their existing or emerging properties range from magnetism, electronics, optics, energy conversion, catalysis, sensing, *etc.*[1,5−11] Eventually, they offer an important extension to the fundamental knowledge of colloidal science with new interactions between nano-objects, more morphologies, tunability, higher versatility, *etc.*

The main routes for SL fabrication fall into two categories: *equilibrium* and *out-of-equilibrium* processes, which are sometimes interwoven. The equilibrium route takes full advantage of thermodynamics applied to colloidal physical chemistry to nucleate SLs from bulk[6,12] or at an interface (liquid/solid or liquid/gas).[13,14] The classical interactions between colloids (electrostatics, steric, depletion, van der Waals) are enriched at nanoscale by a set of specific interactions such as facet-selective or reconfigurable ligands,[15−18] morphology-dependent forces,[19,20] size-tunable dipolar interactions,[21] and solvent-mediated interactions.[22] Astonishing crystalline morphologies have been obtained[23−25] with new structures and properties. In this fabrication route, the typical coherence length of the resultant material

* Address correspondence to jacques.leng-exterieur@solvay.com.

Received for review April 10, 2013 and accepted July 31, 2013.

Published online July 31, 2013
10.1021/nn401764r

is rather modest—on the order of 1−100 μm—and due to the fabrication process, neither shaping-up nor integration seems straightforward.

The out-of-equilibrium routes nonexhaustively include sedimentation,[26] dielectrophoresis,[27] spin- or dip-coating,[28,29] and drying.[30] The latter method is by far the most often used for the fabrication of SLs[6] and is quite versatile, for example, drop casting, evaporation-induced self-assembly (EISA), evaporative coating, *etc.* Well known, quantified, and exploited at the microscale to engineer deposits or functional materials (sessile drop,[31] jet printing,[32] coatings,[33,34] EISA[35]), it basically relies on a local increase of the concentration upon solvent extraction to generate colloidal crystals and often takes advantage of capillary effects to guide microparticles. Transport phenomena, crucial in this matter, make the process rather complex: the flow induced by evaporation (including free-surface effects) transports the colloids, and both transport coefficients as well as evaporation itself may be concentration-dependent. The full process therefore results in an interplay between kinetics and thermodynamics. In the field of SLs, the drying-based driven assembly seems so far based on empirical and educated guesses[36] which nevertheless turn out extremely successful in terms of fabrication procedures.

Whatever their fabrication route, the integration of SLs in functional devices offers a promising prospect: the merging between microscaled *top-down* architectures and nanoscaled *bottom-up* assemblies.[37] Recent examples include the use of microfluidics to characterize[38] or optimize[39] the structure and growth of SLs, micromolding for the deposition of large and thick areas of SLs,[40] localization of SLs upon drying into patterned substrates,[41] transfer and nanoengineering of self-standing nanosheets,[42,43] *etc.*

Here we use *microevaporation*,[44−49] a microfluidic technique based on evaporation, that permits us to *grow and shape-up* extended, three-dimensional thick lattices of densely packed NPs (typical size of the final material 10 μm × 50 μm × 1 cm) with a fine control as to the positioning and composition of the array. The technique takes advantage of the selective permeability of an integrated membrane to extract the solvent of a dispersion but *not* the NPs. The latter get accumulated in a microchannel whose geometry is neatly defined by lithographic techniques, and upon sufficient accumulation, a dense state grows to eventually totally fill the channel (Figure 1). Importantly, the present microfluidic approach is fairly general and does not rely on a specific type of NPs, as long as they feature sufficient colloidal stability as we shall see latter, and actually works for a large set of solutes, from molecules to large colloids.

Microevaporation shares similarities with other evaporation-based techniques but has also its own spectrum of specificities. It takes from EISA[35] the driving

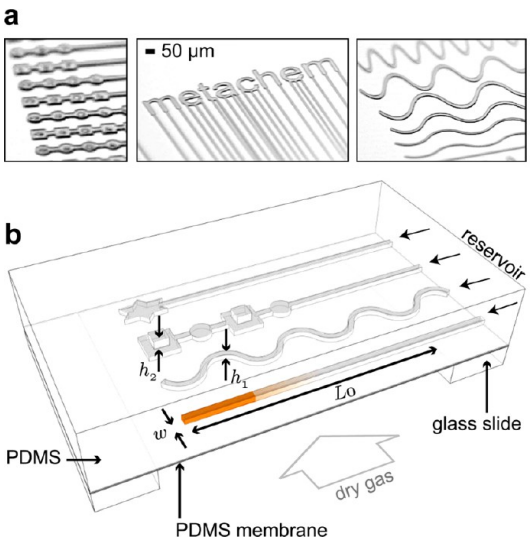

Figure 1. (a) Images of several resist-on-silicon patterns used for the fabrication of microfluidic devices. (b) Evaporation-based cell used for guided assembly of nanoparticles (NPs); evaporation proceeds across the thin PDMS membrane and induces a concentration mechanism that fills the channels with a solid made of densely packed NPs (orders of magnitude: $h_i \approx 5-20$ μm, $w \approx 20-100$ μm, $L_0 \approx 1-10$ mm; PDMS membrane thickness $e \approx 10-30$ μm).

force of evaporation but *suppresses all capillary effects* and works for *all solutes* (*i.e.*, from molecules to large colloids). It takes from micromolding (MIMIC[50]) the capability of casting a shape thanks to a PDMS mold; however, unlike MIMIC, it works *continuously* with the molding capillary connected to a reservoir *and* the evaporation permanently driven across a membrane, actually one wall of the capillary. Hence, the final material is not just a concentrated lump of the initial liquid present in the mold but can be continuously grown with time. As detailed later in the text, this continuous aspect of the process permitted us to fabricate a microscaled heterojunction between distinct arrays of NPs, which appears relevant in terms of device engineering.[51] More importantly, the tool is quite suitable to the quantification of the processes at work during the build-up of a solid at microscale. First, the evaporation is extremely well-controlled by design and imparts a definite pace to the concentration process. Then, *in situ* techniques such as Raman microimaging, on-chip small-angle X-ray scattering, optical microscopy and microspectroscopy, *etc.* help unveil the spatiotemporal features of the concentration dynamics and the coupled roles of concentration- and system-dependent evaporation and transport phenomena.

Here, we focus on aqueous dispersions of NPs and show how it is possible to grow solids owing a set of conditions regarding the stability of the dispersion; the latter must be very stable against precipitation in order to reach a compact state. Indeed, as dispersions of engineered NPs can be rather dilute to start

with (volume fraction $\sim 10^{-6}$ to 10^{-4}, or about 10^{15} particles/L), any trace of pollutant may act as a precipitant upon concentration. On the basis of our specific process, we work out some general conditions that ensure the growth of a solid out of the dilute dispersion. In this framework, we evidence that the growth dynamics of the solid is chiefly governed by the physical chemistry of the dispersion (*e.g.*, the type of ligand on the NPs). All these results are assessed with simple theoretical arguments which yield a robust roadmap for growing micromaterials made of NPs. We illustrate the procedure with a series of solids—including SLs and composites—grown out of a variety of NPs with different shapes, chemistry, and functionality. Eventually, we take full advantage of the open-access reservoir of the microfluidic device to illustrate how to engineer heterojunctions and how to grow solids out of dispersions which are otherwise prone to precipitation.

RESULTS: CONTROL OF THE SOLID GROWTH

The device illustrated in Figure 1b works by extraction of the solvent from a channel in contact with a thin PDMS membrane ($\approx 10-30\ \mu$m). We focus here on the linear and planar geometry of Figure 1b, but the very same principle applies for all possible shapes of the channel. The latter can be nonplanar (*i.e.*, real 3D geometries) due to multilevel photolithography (Figure 1a). Due to the assumption of *local thermodynamic equilibrium*,[52] any concentration process can be rationalized on the basis of two coefficients, one of thermodynamic nature, the chemical activity a that expresses how the evaporation is altered by the presence of a solute, and one of kinetic nature, the collective diffusion coefficient D that describes the transport properties of the dispersion/solution. Using a basic scaling analysis of the concentration process given below, we design microevaporators which are capable of concentrating extremely dilute suspensions and grow and shape-up a solid of NPs in a controlled manner in a matter of hours.

Concentration Mechanism. *Conservation Laws.* For linear geometries, the evaporation flow rate Q_e is a key parameter and it is measured using an *ad hoc* calibration ($Q_e = \mathcal{O}(1-100$ nL/h)[48]); for convenience, we introduce the lineic evaporation rate $q_e = Q_e/L_0$. The extracted solvent is replaced by a compensation flux coming from the reservoir, and this is the very basic mechanism which drives the solute from the reservoir toward the tip of the evaporation channel (as in suction pumps in plants[53,54]), where it accumulates. Such an evaporation-driven flux is induced by the difference of water chemical activity (or potential) across the membrane $a(\phi) - h_e$, where $a(\phi)$ is the concentration-dependent activity of water in the dispersion at solute volume fraction ϕ and h_e the humidity of the gas blown on the other side of the membrane (Figure 1b). This driving force induces permeation which translates into a local velocity $v(x)$ as expressed directly through the following local conservation equation:

$$hw\partial_x v = -(a(\phi) - h_e)q_e \quad (1)$$

where h and w are the transverse dimensions of the channel (Figure 1) and L_0 is the evaporation length of the channel exposed to the membrane. In the rest, we make sure that $h_e = 0$ in all cases. In eq 1, $v(x)$ is the width- and height-averaged volume velocity in the channel,[52] x the long axis of the channel. Global mass conservation ensures that all the solvent that evaporates is replenished by a flux that comes in from the reservoir at a flow rate $Q_0 = V_0 wh = q_e L_0$. Therefore, the natural scale for the velocity follows $V_0 = q_e L_0/wh$, where the evaporation time $\tau_e = wh/q_e$ emerges. It is the natural time scale of the process and corresponds to the time needed to empty one volume of channel. We notice here a benefit of miniaturization with the factor L_0/wh which amplifies the surface effect of evaporation and makes V_0 significant essentially because surface-to-volume effects are majored in these micrometer-sized devices. When pure water evaporates ($a = 1$), the evaporation-induced velocity profile simply reads $v(x) = -x/\tau_e$. Note that the above-mentioned conservation arguments simplify considerably in the geometrical limit of very flat channels ($h \ll w$) in contact with an ultrathin membrane ($e \ll w$) for which evaporation proceeds *across the membrane only*; therefore, $q_e = wv_e$, with v_e the evaporation velocity of water solubilized in the membrane well-described using a Fickean approach.

The induced flow drives solutes toward the tip of the microchannel and traps them only if the induced velocity dominates diffusion over the length of the channel L_0, as expressed by the Péclet number: $Pe = L_0 V_0/D$. The solute—which does not evaporate—is conserved in the channel, and the kinetics of the concentration process $\phi(x,t)$ results from a convection−diffusion competition:

$$\partial_t \phi = -\partial_x[\phi v - D(\phi)\partial_x \phi] \quad (2)$$

where $D(\phi)$ is the *collective diffusion coefficient*, a transport coefficient that describes how the solution/dispersion relaxes concentration gradients. In colloidal science, $D(\phi)$ is generally expressed as an interplay between osmotic compressibility and viscous drag in a dispersion.[55] Refs 48 and 49 give a detailed and practical use of these quantities in the present case of microfluidic evaporation.

Orders of Magnitude and Scaling Analysis. It is worth stressing again the benefits of the microfluidic format in the context of dispersions of NPs. Due to the neat control of the geometrical design and operation parameters, all physical scales of the process are precisely known: the thickness of the PDMS membrane and the dimensions of the channel altogether define the evaporation time τ_e ($=10^2-10^3$ s typically); the length L_0 of

the channel and the evaporation time τ_e define the evaporation-induced velocity everywhere and, in particular, the entrance velocity $V_0 = L_0/\tau_e$.

Additionally, the knowledge of two coefficients $a(\phi)$ and $D(\phi)$ permits us to predict the exact spatiotemporal kinetics of the concentration process. In the case of ideal solutions [$a \equiv 1$ and $D \equiv D_0 = kT/6\pi\eta R$ from Stokes–Einstein relation, $D_0 = \mathcal{O}(10^{-12}–10^{-11}$ m^2/s) for NPs], the competition between convection and diffusion defines a length $p = (D_0\tau_e)^{1/2}$, which delineates the convection-dominated zone ($x > p$) and the diffusion-dominated zone ($x < p$). The concentration process is efficient only if $p < L_0$, that is, for a Péclet number $Pe = L_0V_0/D_0 = (L_0/p)^2 > 1$. For suspended nano-objects, $p \sim 100$ μm, which sets the minimal size of evaporators to be efficient.

For $Pe \gg 1$, the scaling analysis of the transport eq 2 shows that the diffusion-dominated region is permanently fed with NPs with an incoming flux ϕ_0V_0 with ϕ_0 the volume fraction of NPs in the reservoir, leading to a local ($x < p$) increase of the concentration: $\Delta\phi/\Delta t \sim \phi_0L_0/p\tau_e$. Working with extremely dilute suspensions therefore imposes strong constraints as to the design of our microevaporator; we indeed require the time Δt to concentrate a dilute suspension ($\phi_0 = 10^{-6}–10^{-4}$) into a dense state ($\phi_d \approx 0.5$) to be reasonable, that is, as most of order of hours. As $\Delta t \sim (\tau_e/\phi_0)(p/L_0)$, we design the device in order to maximize the length L_0 (up to centimeters) while scaling down the product $\tau_e p \sim \tau_e^{3/2}$, which we achieve by making very thin devices ($\tau_e \sim h/v_e$), which evaporate very efficiently (high v_e) due to very thin membranes ($v_e \sim 1/e$). Evaporation is further sped up for small channel width w and well-separated channels.[53] Typical values are $e \approx 10$ μm and $h \approx 5$ μm (these are the values we use for the rest of this work), leading to $\tau_e \approx 50$ s. The latter value is actually obtained within % with a dedicated calibration method described previously.[48] It is worth mentioning that the scaling analysis strictly holds for dilute suspensions only, but in all cases we studied so far, it works well up to fairly concentrated regimes and thus remains a valuable tool for designing the evaporation devices.

Having designed, fabricated, and calibrated such evaporators, we can concentrate in a reasonable amount of time (order of hour) the initially dilute suspension until the nucleation and growth of a dense state occurs.

Transport- or Evaporation-Limited Growth. For $Pe \gg 1$, the NPs are trapped in the thin linear channel and get accumulated at its tip over time while permanently fed by a steady flux of solutes from the reservoir. Eventually, upon sufficient accumulation, nucleation of a dense state at $t = t_N$ may occur, followed by a growth kinetics. Figure 2a shows such a kinetics observed under a microscope and characterized using the (image-processed) position $x_d(t)$ of the front.

We display in Figure 2b,c two main limiting cases for the growth kinetics, which are actually fully tuned by the physical chemistry of the suspensions: *transport-* and *evaporation-limited growth*. Figure 2b shows the case of sterically stabilized NPs (Au@PEG, after the [core material]@[shell or corona material] nomenclature) for which the trajectory of the dense front slows down over time (whatever L_0, Figure 2b left); scaling the front with the respective lengths L_0 of the channels in which the fronts grow (Figure 2b right) and the time from nucleation with the natural evaporation time τ_e shows a good collapse which is well-described by a single exponential (solid black line). Inversely, the case of charge-stabilized NPs ($Ag@SiO_2$) shows a linear growth kinetics which also rescales well with the same dimensionless variables (Figure 2c right).

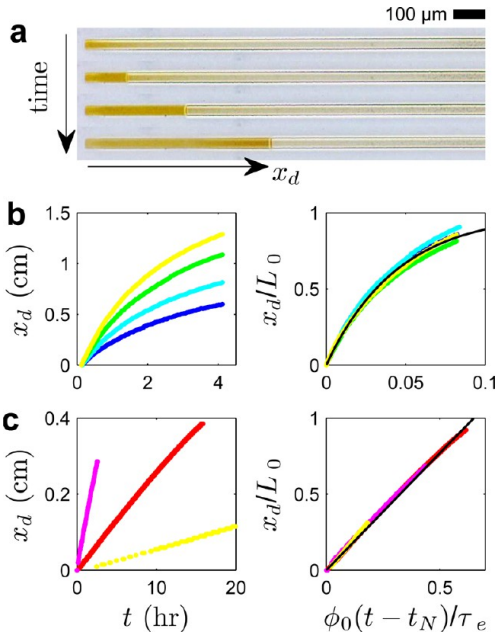

Figure 2. (a) Typical series of images acquired during the growth of a dense state made of NPs (here $Ag@SiO_2$). The temporal analysis of the growth kinetics leads to two limiting cases: (b) limited by the chemical activity yielding an exponential slowing down (Au@PEG in water with $\phi_0 = (3.3 \pm 0.1) \times 10^{-4}$ and $\tau_e = 56 \pm 2$ s, NPs with a core diameter $\approx$15 nm; one concentration ϕ_0 only and different L_0); (c) limited by the transport coefficient yielding a linear growth ($Ag@SiO_2$ in water with $\phi_0 = (2.3 \pm 0.3) \times 10^{-2}$ and $\tau_e = 480 \pm 20$ s; NPs with a silver core diameter of 20 nm and a silica shell 35 nm thick; one length L_0 only and different concentration ϕ_0).

We rationalize these results on the basis of a simple conservation law which balances the volume growth rate of the dense with the flux of incoming particles: $\phi_d\dot{x}_d \approx \phi_0\tilde{V}_0$, with $\tilde{V}_0$ specifying that the incoming flux is possibly altered by the presence of a dense state within the channel. Note also that we neglect here the concentration just before the front as it is very small in our present studies but may be significant in other cases.[48] Making dimensionless all the variables [with $X_d = x_d/L_0$, $T = (t - t_N)/\tau_e$, and $\Phi = \phi/\phi_0$], calling Φ^* the packing fraction of the growing solid, and introducing

some specificity as to the physical chemistry of the system under study, we obtain two limiting cases for the growth rate:

•*Transport-limited growth* when the water evaporates as pure water independently of the colloid concentration: $\Phi^*\dot{X}_d \approx 1$; it holds whenever the water activity is barely altered by the presence of colloids such as, for instance, not-too-small silica-based colloids (with no grafted polymer), requiring actually a modest modification of the chemical potential of water with colloids. This modification scales like $\Delta\mu_w \sim k_BTv_s/v_c$, with k_BT the thermal energy, v_s the volume of the solvent molecules, and v_c that of colloids;[48] $\Delta\mu_w \ll k_BT$ even for small NPs. As a consequence, water evaporates as if it were pure, colloids get concentrated and pile-up into the dense state at a *constant rate* = $1/\Phi^*$; the growth actually stems from the diverging part of the osmotic compressibility of the diffusion coefficient $D(\phi)$ which prevents concentration gradients to be sustained: a dense state grows simply because it cannot be concentrated anymore. In such a case, there is always evaporation below the packed bed, a flow inside it, and *a flux of water into the solid* at the level of the front. In turn, the constant growth rate $1/\Phi^* = \phi_0/\phi_d$ justifies our choice to also include the initial concentration for rescaling the front position ($t \rightarrow \phi_0 t/\tau_e$): in this choice of units (Figure 2c right), the growth rate $\sim 1/\phi_d$ directly leads to the packing fraction of the dense state. Here, we find $\phi_d = 0.6 \pm 0.1$, which gives a first insight as to the structure of the dense state.

•*Evaporation-limited growth*, when, on the contrary, concentrated colloids modify significantly the water activity. It is the case of polymer-coated NPs where the polymer, here a PEG (Figure 2b left), dominates at very high concentration in lowering the water activity down to 0. In this case, we simply assume that water does not evaporate *at all* anymore above the dense state [$a = 0$ for $x < x_d$ and $a = 1$ otherwise], and the evaporation-induced velocity drops with the ever increasing dense state $\tilde{V}_0(x_d) = (L_0 - x_d)/\tau_e$ as a consequence of a diminished effective length of evaporation $L_0 \rightarrow L_0 - x_d$. This is the exponentially slowing-down mechanism of growth. Indeed, the growth kinetics reads $\Phi^*\dot{X}_d \approx 1 - X_d$, which admits an exponential solution $X_d = 1 - \exp(-T/\phi^*)$, fitting well our data, Figure 1b right. In this figure, ϕ_0 stands for the volume fraction of gold only (*i.e.*, the cores of the NPs), and we find $\phi_d \approx 0.10$. At this stage, the final composite is made of 10% gold NPs, the rest being (probably hydrated) polymer.

The nature of the growth kinetics, that is, linear or exponential, thus tells about the interplay between the way water evaporates in the dense state and how concentration gradients are sustained. We just saw two limiting cases where the growth is driven by (i) a diverging diffusion coefficient or (ii) stopped evaporation, but there are of course intermediate regimes between these two limiting cases. It is, for instance, the case of NPs strongly interacting *via* electrostatics[47] for which the basic conservation law must be modified to account for interaction-dependent transport coefficient or surfactant molecules[49] for which both the evaporation and the transport phenomena are mesophase-dependent. It remains that the knowledge of basic kinetic and thermodynamic data (a and D) permits us to predict the growth kinetics, and that its image-processed inspection (Figure 2) yields an estimate of the packing fraction in the dense phase.

Stability Issue. The previous scenarios hold only if no "accident" such as precipitation or aggregation occurs en route toward high concentration. The depiction of a binary system with NPs in water *only* is actually somewhat utopistic; we cannot elude the presence of pollutants solubilized in water which may play the role of destabilizing agent. Indeed, our evaporation-based device leads to an increase of the concentration of *all species*—although at different rates—and the localized increase of pollutant may well induce the aggregation of the dispersion. As we are working with extremely dilute dispersions of NPs, what matters is how much pollutant is present in the initial dispersion because even traces might play a significant role upon concentration.

For the sake of illustration, we consider here a specific case of traces of salt present in the dispersion of silica NPs in water. It could also be the case of solubilized PEG oligomers acting as depleting agents. We model the stability of the dispersion at the lowest level using a binary stability ratio W (the ratio of the aggregation rate at a given salt concentration to the one of an unstable dispersion[55]): $W \rightarrow \infty$ below a critical salt concentration c_s leading to a stable dispersion, and $W = 1$ above with near immediate aggregation. Then, assuming that in the dilute regime $a \equiv 1$ and $D \equiv$ const. (D_c for colloids and D_s for salt) in eqs 1 and 2, we solve the dynamics of the concentration process for both the colloids and the salt assuming they are independent, which is reasonable in the dilute regime only. In dimensionless variables, the control parameters are the salt concentration $C = c/c_0$ (c_0 is the salt concentration in the reservoir), the volume fraction of colloids $\Phi = \phi/\phi_0$ (ϕ_0 is the volume fraction of NPs in the reservoir), the Péclet number of salt Pe and that of colloids Pe_c. We gave elsewhere analytical solutions[46] for the full concentration process $C(X,T)$ and $\Phi(X,T)$ in the dilute regime, which we recall in the Supporting Information, and we examine here the issue of the coupled dynamics regarding the stability of the dispersion. We do not discriminate between heterogeneous (on the wall) or homogeneous aggregation (between particles) and just assume that the dispersion may become unstable above C_s. We identify two limiting cases for which there is either *precipitation only* or *growth only*. In brief (all details in the Supporting Information), if the concentration of salt in the reservoir

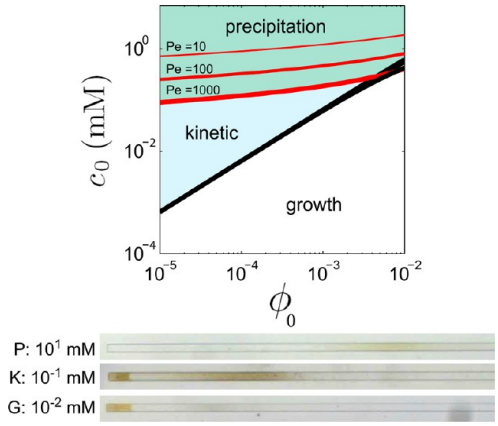

Figure 3. Top: stability chart giving the outcome of the concentration process (*growth* of a solid, *precipitation* of NPs, and mixed *kinetic* regime; see text) depending on the volume fraction ϕ_0 of NPs and the concentration c_0 of an electrolyte *in the reservoir* (or, equivalently, in the stock dispersion). The present chart is calculated for charge-stabilized NPs, which become unstable above a critical salt concentration; *Pe* in the figure stands for the Péclet number of the salt, the one of the NPs being considered nearly infinite (all details of the calculation are given in the Supporting Information). Bottom: examples of the three states described in the stability chart (P: precipitation, K: kinetic, G: growth), induced here with the amount of added salt (NaCl) indicated on the figure (and $\phi_0 = 2.3\%$); the width of the channel is 40 μm and pictures taken about 3 h after the beginning of the concentration process.

is too high, the salt concentration at the tip of the evaporator will overcome C_s before the NPs get sufficient time to nucleate a dense state (*precipitation regime*); conversely, when the concentration of salt is low enough in the reservoir, nucleation may occur and the growth will be fast enough to escape the region where the salt gets accumulated (*growth regime*).

We summarize these calculations on a stability chart (Figure 3) which delineates these two limiting cases as a function of the volume fraction ϕ_0 of the dispersion and the concentration of salt c_0 both taken *in the reservoir*, that is, in the native dispersion. We also evidence an intermediate regime (*kinetic regime*) in which the two kinetics are so close that interwoven events may occur such as precipitation followed by growth or even re-entrant transition as growth/precipitation/growth. All these states have been observed experimentally and are illustrated in Figure 3 where we concentrated a dispersion of Ag@SiO_2 NPs with a *controlled* amount of added salt.

Importantly, we find that the growth-only upper boundary does not depend on the Péclet number of colloids and reads $\Phi^* \ll C_s$ in dimensionless units, or with dimensions simply

$$\frac{c_0}{c_s} \ll \frac{\phi_0}{\phi_d} \qquad (3)$$

where we recall that ϕ_d is the volume fraction of the dense state ($\mathcal{O}(1)$), ϕ_0 and c_0 the concentrations of NPs and salt in the reservoir, respectively, and c_s the concentration at which the dispersion becomes unstable ($c_s \approx 10-100$ mM for typical charge-stabilized systems). It thus permits us to rapidly estimate whether a dispersion can be grown into a dense state or will precipitate.

As a rule of thumb, we notice that charge-stabilized NPs are prone to aggregation especially when working at low concentration. For a typical sol–gel-processed silica coating on the NPs (*e.g.*, with a zeta-potential on the order of −40 mV at pH 5–7), traces of salt on the order of 1–10 μM are sufficient to prevent growth of a suspension with $\phi_0 \approx 10^{-6}-10^{-5}$. Increasing ϕ_0 by a factor of 10 to 100, for instance, is sufficient to escape the stability trap, and silica then becomes a very good stabilizer against aggregation for moderately diluted dispersions. We will discuss in the last section of this article another way of escaping the stability trap by the use of a microfilter.

Alternatively, sterically stabilized NPs with a grafted polymer are especially stable assuming there is no depleting agent in the dispersion (such as nongrafted polymers) that would be deleterious to the growth process. Here, we used several polymers but present mostly results concerning PEG-grafted NPs for which a thorough wash of the dispersion is required to eliminate unattached polymers and prevent depletion between NPs or between the particles and the wall of the microfluidic cell.

DISCUSSION: SHAPING BULK MATERIALS MADE OF NPS

Growing a material out of a dispersion of nano-objects thus requires colloidal stability. Assuming this or designing the NPs for this purpose, we demonstrate below that all sorts of dispersions can be assembled into dense, real 3D materials. A quantitative analysis of the structure on a specific case (15 nm diameter spherical Au@PEG NPs) using X-ray scattering shows that the particles crystallize into SLs, yet with small-size crystallites ($\approx\mu$m). Experimentally, we also evidence that the order of these superlattices could be drastically improved with more calibrated dispersions. Anisotropic particles and mixtures of NPs can also readily be assembled thanks to microevaporation. Eventually, we show that heterostructures can be engineered by growing side-by-side materials made of different types of particles.

Structure. We start with Au@PEG and Au@SiO_2 NPs dispersed in water (same core, 15 nm diameter, spherical, and liganded with a 5 kDa PEG or capped with a 20 nm thick silica shell) which we concentrated until a dense state grew over several millimeters (Figure 2 and Figure 4a using an optimized chip with a thickness of 5 μm and a volume fraction of NPs larger than $\phi_0 = 10^{-4}$ in order to prevent precipitation in the case of Au@SiO_2 NPs). The growth kinetics of such a micromaterial is best quantified in the linear geometry of Figure 2;

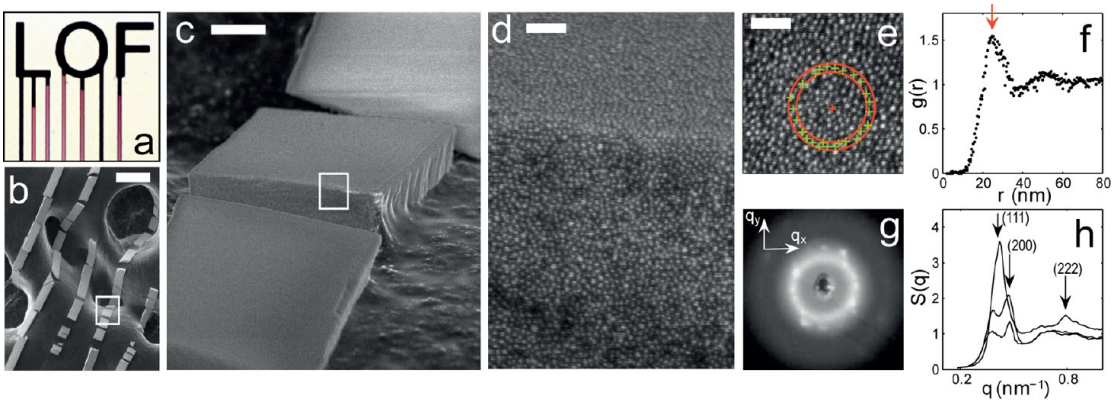

Figure 4. Images and structure of solids densely packed with NPs: (a−d) Au@SiO_2 with a 15 nm diameter core and a silica shell 20 nm thick, (e−h) Au@PEG with a 15 nm diameter core and a corona made of 5 kDa PEG grafted with thiols. (a) Tip of a tailor evaporation-based cell seen under a microscope and where the NP suspension undergoes a nucleation/growth kinetics (width of smallest channels 20 μm, height $\approx$ 5 μm). (b−d) Dense state resulting from (a) after drying and stamping onto a SEM substrate observed with SEM at several degrees of magnification (scale bar is 50 μm in b, 5 μm in c, and 150 nm in d). (e,f) SEM high magnification of the surface of the dense material (scale bar 100 nm) and pair correlation function $g(r)$ calculated after particle centers registration. (g,h) *In situ* microfocused small-angle X-ray pattern and angular averaging of various patterns such as (g) yielding the structure factor $S(q)$ *vs* wave vector q indexed in (h) for a fcc structure with lattice parameter of 28 nm, gold volume fraction of 0.27. The presence of Bragg peaks in the pattern of (g), also related to the marked peaks in the angular averagings presented in (h), demonstrates the local crystalline order of the NPs.

however, other geometries can be designed using soft lithography, including "device-oriented" shapes in which the growth takes place in the very same fashion (Figure 1 and Figure 4a).

We demonstrate that the micromaterial is made of densely packed NPs by monitoring its structure under a high-resolution scanning electron microscope (SEM). First, we peel off the membrane of the evaporation microfluidic chip and stamp the micromaterials onto a conductive tape previously stuck on a SEM substrate (a metallic pin). This transfer process is very efficient but somewhat brutal, and the structure sometimes breaks at places (Figure 4b); in this figure, we recognize the linear aspect of the micromaterial and we take advantage of the alveolar structure of the conductive tape to have some parts of micromaterial exposed to the electron beam with a slanted view. Zooming in such a zone (Figure 4c) evidences a brick-like edifice with neat facets and edges that actually reflect how the microfluidic channel promotes the shaping process. An even higher magnification (Figure 4d) now shows that the material is indeed made of tightly packed NPs, with here no obvious long-range order, and that the upper facet of the material is extremely smooth with a roughness basically set by the size of the NPs. The flatness of the material thus lies well within optical quality (here $\approx\lambda/20$), thanks to the PDMS molding; it is a crucial point for the optical characterization.

The volume fraction occupied by NPs in this composite is on order of 25%, the rest consisting of polymer, as consistently demonstrated using SEM image analysis and *in situ* X-ray scattering. From a SEM image acquired on the upper face of the material with its normal parallel to the electron beam, we construct the pair correlation function $g(r)$. It is achieved by first registering the position of all particles (about 3000 on a typical image) and by then calculating the number of particles at a distance $r + dr$ from a given one (Figure 4e; the red circles and green crosses illustrate the counting procedure). The calculation is repeated for all distances and ensemble-averaged over all particles. The pair correlation function $g(r)$ is normalized to 1 at high distances leading to the surface density of particles $\sigma = (1.37 \pm 0.06) \times 10^{15}$ particles/m^2. The correlation function exhibits an oscillating behavior with a modest peak at $r_m \approx 28$ nm (red arrow, Figure 4f), the mean distance between first neighbors. The shape of $g(r)$ along with the height of the peak suggests that the planar organization of NPs is amorphous, with no long-range order.[56] The surface fraction occupied by the gold cores is $\phi = 4\pi\sigma r_p^2 = 0.25 \pm 0.06$.

Alternatively, we used small-angle X-ray scattering (SAXS) with a microfocused high brilliance beamline (spot diameter $\approx$1.5 μm, ID13, ESRF, Grenoble, France) to probe the structure of the micromaterial.[47] The latter was scanned pointwise directly into the chip, and diffraction patterns (Figure 4g) vary significantly from point to point but always exhibit Bragg spots superimposed to diffuse rings. From the measured form factor of the Au@PEG particles, we calculate the angular-averaged structure factor $S(q)$ of the assembly as shown on Figure 4h for three different locations within the material. A basic analysis suggests that the structures we observe are compatible with face-centered cubic (fcc, indexing in Figure 4h) grains of a typical coherence length $\xi \sim \mu$m, seen under different orientations, with a NP packing fraction $\approx$0.27 and a lattice parameter of 28 nm, which compares well with the SEM image analysis. A refined analysis is made quite complex by the fact that the powder-averaging is actually poor due to the small coherence of the crystalline lattice ($\xi/r_m \approx 30$ where r_m is the distance between

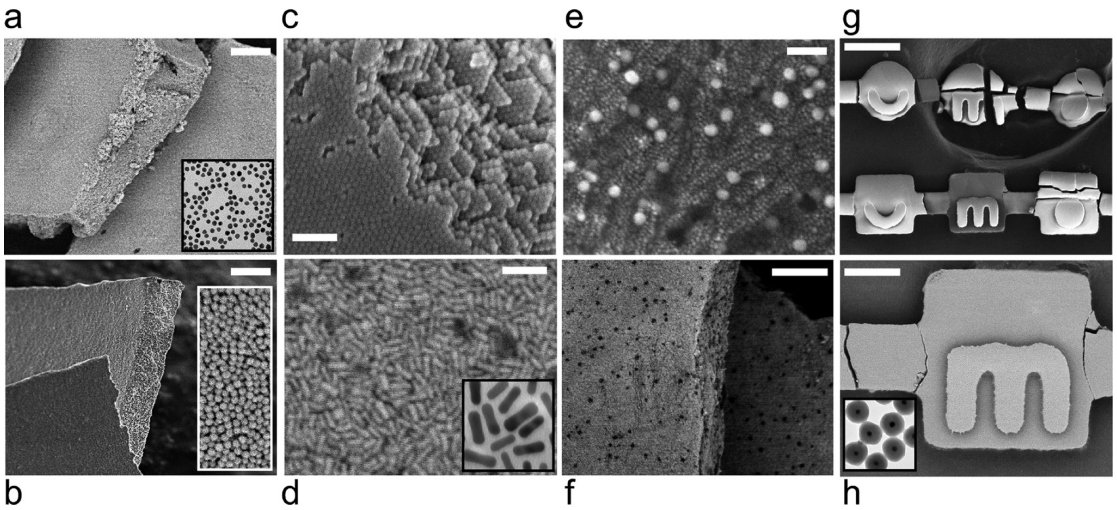

Figure 5. Catalog of dense structures generated with microevaporation and observed with a SEM: (a) Au@PEG 15 nm diameter (bar is 1 μm, inset is a TEM picture of native particles); (b) Au@PEG 60 nm diameter (bar is 1 μm, inset is a SEM picture of the surface of the material); (c) 80 nm diameter silica NPs (bar is 500 nm); (d) Au@PEG nanorods (bar is 100 nm, inset is a TEM picture of nanorods); (e) mixture of Au@PEG 15 and 60 nm (bar is 200 nm); (f) mixture of 15 nm Au@PEG and 80 nm silica NPs (bar is 1 μm); (g) Ag@SiO_2 NPs in 3D channels (bar is 50 μm); (h) same sample seen at higher magnification (bar is 10 μm, inset is a TEM view of native core−shell NPs).

first neighbors) and few grains only in the thickness of the cell ($h/\xi \approx 5$).[57,58] The presence of Bragg spots (Figure 4g) is however a definite proof of SLs, but with a limited spatial extent; it may be due either to the non-negligible size dispersity of the native gold NPs or to the rate at which the solid is built.[59] We leave open this question but nevertheless evidence below that, with very monodisperse NPs, long-range crystallization is obvious even from a SEM image.

Eventually, we notice that the volume fraction obtained from structural analysis (≈0.3) is higher than the one estimated directly by monitoring the growth rate of the solid (≈0.1) (while for other cases, such as large colloids, both analyses coincide[48]). We believe it comes from the fact that samples were dehydrated or left in a dry atmosphere before structural analysis.

From Simple Materials to Tailor Composites. We now turn to a description of a few structures we could build (Figure 5) and emphasize some of their features. First, we notice that the micromaterials we fabricate are very planar, basically *self-standing thick films*; depending on their type, they can be brittle and fragile but it is possible to extract millimeters of them out of the chip. Au@PEG materials are especially easy to grow (we achieved materials with 15 and 60 nm core diameter, Figure 5a,b) and mixtures thereof (Figure 5e) but exhibit little surface order, although we know from above that the surface inspection may hide the bulk organization. For comparison, commercial silica NPs (80 ± 5 nm diameter, polydispersity assessed from SAXS analysis) grow under obvious, hexagonal-like crystalline habits (Figure 5c).

Anisotropic particles assemble as well into close-packed assemblies, and we could grow dense materials of nanorods (Figure 5d), nanocubes, and nanodisks (not shown), all stabilized by polymers. In the present case of Au@PEG nanorods (long axis 37 ± 7 nm, small axis 11 ± 2 nm), it was somewhat expected[12] that these particles did not get oriented at all; it is indeed known that aligning such modest aspect ratio rods (≈2−3) rather requires a thermodynamic approach with a fine-tuning of the interaction parameters between the rods.[60−62]

Mixtures of small and large NPs readily assemble (Figure 5e,f), but some care must be taken as to the mutual interactions between small and large colloids. For instance, mixtures of Au@PEG small particles with larger SiO_2 NPs are unstable at high concentration for most of the mixture ratios we examined, probably due to hydrogen bonding between the PEG and the silica surfaces likely to generate aggregates en route toward high concentrations. We illustrate in Figure 6 a robust formulation for the fabrication of composite binary solids made of large SiO_2 NPs and small Au@SiO_2 NPs, here characterized by a ratio in number R (large-to-small). The final materials are quite homogeneous at the macroscopic level (Figure 6, top right) and absorb light in relation to the amount of gold inclusions (up to opaque samples for $R \to \infty$, *i.e.*, only small gold NPs) but appear somewhat heterogeneous at the nanoscale. Interestingly, for $R = 1$. the large silica NPs crystallize at places but not everywhere (Figure 6, bottom left) and the disorganized zones seem correlated to a larger local amount of small inclusions. For higher ratios, it becomes possible to decorate the large NPs with a large number of small satellites (Figure 6, bottom right) and to reach structures with a connected network of plasmonic inclusions embedded in a dielectric substrate. These structures resemble much the ones manufactured with preassembled nanoclusters, such as in Figure 7, bottom right. The "binary" route hence turns

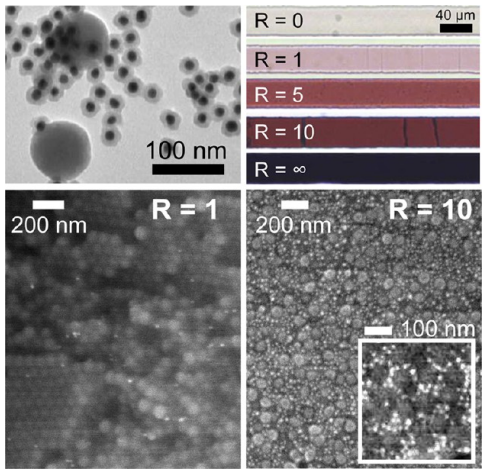

Figure 6. Top left: TEM picture of a binary mixture of large silica NPs (80 nm diameter) and small Au@SiO_2 NPs (15 nm core diameter, 10 nm thick silica shell). Top right: micromaterials obtained from binary dispersions with different ratio in number R of large-to-small particles. Bottom left: SEM pictures in backscattering mode for $R = 1$. Bottom right: SEM picture for $R = 10$, with the inset showing the same structure in backscattering mode.

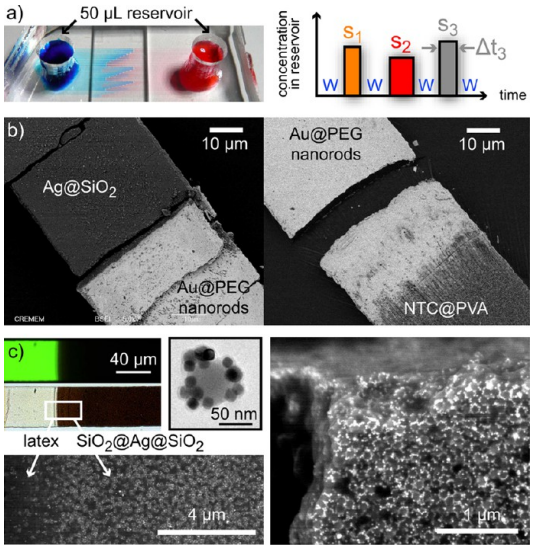

Figure 7. Protocol for building heterojunctions at the nanoliter scale. (a) The chip we use possesses a 50 μL open-access reservoir in which we can pipet sequentially several dispersions or solutions during a known lapse of time (top right for the pipetting workflow). It enables us to build a sequential solid, here illustrated with (b) a double junction made of Ag@SiO_2 next to Au@PEG nanorods next to carbon nanotubes CTN@PVA or (c) a simple junction between large latexes and engineered nanoraspberries SiO_2@Ag@SiO_2, the bed of latexes acting as a filter for salt; see text.

out useful to simplify the fabrication process of advanced assemblies.

Eventually, we grew dense materials of core−shell Ag@SiO_2 NPs into 3D cavities (Figure 5g,h, silver core diameter 20 nm, silica shell thickness 35 nm) and the bottom-up-assembled final material nicely replicates the top-down-designed microfluidic chambers, with details fixed by the soft lithography technique used here (*i.e.*, order of μm). Here again, the structure of the colloidal assembly (detailed elsewhere[63]) is not ordered at long-range as probably limited by the size dispersity of core−shell Ag@SiO_2 NPs, and some faceting of the NPs is observed in the final solid.[63]

Active Control of Growth: Heterostructures. Heterostructures based on NPs can be built by taking advantage of a *sequential-filling approach*. Microevaporation chips can be engineered with a 50 μL open-access reservoir (Figure 7a) which permits us to tune *in time* the solution to be concentrated. By sequentially filling the reservoir with different dispersions, we accumulate different NPs and grow dense states in a sequential manner, which results in a layered material.

Figure 7a (right) also illustrates the corresponding protocol during which the reservoir is initially filled with pure water (W); at a given time, the water in the reservoir is replaced with dispersion or solution S_1 at concentration ϕ_0^1 which is left to concentrate for a lapse of time Δt_1; the dispersion is then replaced with pure water again. In linear geometries, solute conservation ensures that the particles driven inside the chip by evaporation contribute to build a linear dense state with a growth rate $\dot{L}_1$ (system-dependent, Figure 2). The total length of material $L_1 \approx \dot{L}_1 \Delta t_1$ is thus controllable by simply playing with the lapse of time Δt_1 and the concentration in the reservoir ϕ_0^1. Then, the reservoir is flushed with pure water, and after a delay time that permits the dense state to equilibrate, water is replaced by the second solution S_2 during Δt_2 and flushed again with water to build a second material of length L_2 next to the first one. The pipetting operation can be iterated as often as required and even automated with a liquid-handling robot to build tailor heterostructures.[48]

Figure 7b shows such a heterostructure obtained by sequential filling with Ag@SiO_2 followed by Au@PEG nanorods and then CNT@PVA (surfactant-stabilized carbon nanotubes mixed with a polymer, polyvinyl alcohol, in water). The respective lengths of different segments are on the order of millimeters, and we observe that the junction between the successive dense states extends on a length on the order of a few micrometers (1−10 μm) and depends on the nature of the materials that grew before. Beside the SEM images of Figure 7b, we also used a higher-energy electron beam to probe at the level of the junction the depth of the material (not shown) and the spatial extent of the composition gradient. It is quite obvious in Figure 7b that the Ag@SiO_2/Au@PEG nanorod junction is much neater (extent ~1 μm) than the Au@PEG/CNT@PVA one (~10 μm). It stems from the nature of the first material of the junction: for Ag@SiO_2, evaporation still proceeds above the packed bed (*i.e.*, the activity is not reduced by the presence of colloids) which drains water but not colloids into the packed

bed and forces a condition of *nonvanishing flux of water* at the level of the edge of the first material; newly coming particles of the second type will be dragged by the flow toward the interstices of the first material,[64,65] which blocks them and the second material builds up; as such, it represents an interesting option for studying the controlled hepitaxial growth of colloidal heterostructures. On the contrary, when evaporation stops in the first material (as for Au@PEG nanorods due to the presence of the polymer), the interface of the junction is smooth and the boundary condition is of *no flux*. Therefore, a composition gradient may occur on a spatial extend of order of $p \sim (D\tau_e)^{1/2}$, with D the diffusion coefficient of the colloids, which gives here $p \sim 10\ \mu$m for 50 nm colloids and $\tau_e = 50$ s.

Eventually, we also evidence here a way to grow dispersion for which the stability chart suggests it would not be possible directly in the microevaporator, for instance, because the ratio of colloids over traces of destabilizing agent is not favorable (Figure 3). This is the case of engineered raspberry-like nanoclusters (SiO_2@Ag@SiO_2, Figure 7c) which consist of a 86 nm silica core with 30 nm cubes grafted on the periphery and coated with a thin silica shell (≈5 nm). These clusters are meant to exhibit a specific plasmonic behavior[66] and their assemblies to possess exciting optical features. However, due to the high constraints required for their synthesis, their volume fraction is small, $\mathcal{O}(10^{-6})$, and they do not fulfill the growth condition of stability chart (Figure 3). To bypass this limitation, we construct a heterostructure based first on a millimeter-long colloidal crystal of 200 nm diameter polystyrene beads (tagged with fluorescein; see Figure 7c, top left) which acts as a packed bed; upon injection of the nanoraspberries, a dense state of the latter can be grown because the packed bed (pore size ≈10 nm) is permeable to water but not to NPs. Water along with traces of salt can flow inside the colloidal filter which retains the NPs, forcing them to pack and grow at a constant salinity, unlike the case of simple microevaporation which leads here to precipitation as both salt and NPs get concentrated. The resulting heterostructure can be extracted and observed with SEM, which effectively reveals that after the junction (size $\sim\mu$m) with the colloidal filter, the nanoraspberries form a tightly packed state with extended dimensions and an overall shape that reflects that of the microfluidic channel. In particular, the relatively flat faces of the material are quite appealing for the optical characterization (such as microellipsometry) we intend to carry on these 3D samples.

CONCLUSION

Evaporation has become a standard route for the guided assembly of nano- to microparticles. Here, we demonstrated that evaporation within dedicated microfluidic devices permits us to grow and shape-up solids made of NPs. As the microfluidic tool gives both a fine control over the kinetics of concentration and an easy observation in a model geometry, we could rationalize in which conditions the suspensions of NPs are likely to be turned into a solid by solvent extraction. The first criterion holds on the colloidal stability of the dilute suspension: we need to prevent precipitation before growth by carefully checking the amount of precipitant present in the initial stock solution. There is then virtually no limit to the growth and shape-up of all sorts of micromaterials made of NPs, as illustrated here for unary and binary spherical NPs, nanorods, *etc.* While we evidenced the presence of SLs, the coherence length of the latter remains small ($\sim\mu$m) probably due either to a too-high polydispersity of the NPs or to the rate at which the solid is grown (which may overcome the natural rate of crystal growth). This issue is quite promising in terms of crystallinity, especially because we can redesign the microevaporator in order to slow the growth rate of the solid. Indeed, by tuning the humidity outside the device and the thickness of the channel, we can slow by a factor 10^2–10^3 the concentration kinetics and, hopefully, tune the way the material grows.

We also evidenced that the growth rate has intrinsic limits and illustrated two main limiting cases—evaporation- or transport-limited growth—which ultimately couple the physical chemistry of the dispersion to the concentration process. In all cases, it is possible to tune in time the dispersion to be concentrated in order to build tailor solids: we constructed heterojunctions between different types of NPs and colloidal filters that can retain dispersions that would precipitate otherwise.

We believe that the good control and rationalization of the growth process, along with the top-down/bottom-up combination offered by microfluidic evaporation, is promising; it could be useful in terms of fundamental understanding of the growth condition of a solid made of NPs and could also be device-oriented by controlling the placement of lumps or arrays of NPs in order to create new and functional microscale materials.

MATERIALS AND METHODS

Dispersions of NPs. *Gold Spherical NPs.* Tetrachloroauric acid ($HAuCl_4 \cdot 3H_2O$), tetraethylorthosilicate (TEOS), and NH_4OH (29%) were purchased from Aldrich, and sodium citrate ($C_6H_5O_7Na_3 \cdot 2H_2O$) was from Sigma. Cetyltrimethylammonium bromide (CTAB) and *O*-[2-(3-mercaptopropionylamino)ethyl]-*O*′-methylpoly(ethylene glycol) (mPEG-SH, M_w 5000) were provided by Fluka. Pure-grade ethanol and Milli-Q-grade water

were used in all preparations. Unless otherwise stated, all of the chemicals were used without further purification.

Citrate-stabilized Au nanospheres (15 nm) were synthesized as described elsewhere.[67] mPEG-SH functionalization was carried out by dropwise addition of 1 mL of an aqueous solution 1.4×10^{-4} M mPEG-SH to 10 mL of as-synthesized 15 nm spheres ([Au] = 5×10^{-4} M). The mixture was allowed to react for 30 min and was cleaned by two centrifugation−redispersion cycles with ethanol.

Gold Nanorods. PEG-coated Au nanorods (NRs) were synthesized in two steps by modifying reported procedures. Initially, CTAB-coated Au nanorods were synthesized by adapting the protocol reported by Jana.[68] Subsequently, CTAB surfactants bound to the surface of Au nanorods were completely replaced by 5 kg/mol PEG-SH units following the procedure reported by Thierry *et al.*[69] The PEG-functionalized nanorods were characterized using TEM and UV−visible spectroscopy before use in our experiments; for more details, see Supporting Information.

Raspberry-like NPs. L-Arginine (99%), cyclohexane (=99.7%), TEOS (99%), sodium hydrosulfide (NaHS), poly(vinylpyrrolidone) (PVP; M_w = 55 000 g/mol), *N*-[3-(trimethoxysilyl)propyl]ethylenediamine (EDPS; 97%), and silver nitrate ($AgNO_3$; 99.9%) were purchased from Sigma-Aldrich. Ethylene glycol (EG) and ammonium hydroxide solution (27−30 wt %) were obtained from J.T. Baker. Absolute ethanol was purchased from Scharlau. All reagents and solvents are used without further purification.

The silica NPs were prepared using a seed-mediated method.[70] Initially, silica "preseeds" were obtained as follows: 345 mL of an aqueous solution containing 7.5 mM of L-arginine was introduced in a 500 mL rounded beaker; 22.5 mL of cyclohexane was added, and the mixture was heated at 60 °C. When the mixture reached 60 °C, 37.5 mL of TEOS was introduced. The stirring was maintained for 24 h. Then, the mixture was passed to a rotavapor at 50 °C under vacuum to eliminate the cyclohexane. The concentration in silica seeds was determined by dry extract. These seeds were then grown in hydroalcoholic medium containing ammonia and wherein the TEOS was slowly and continuously introduced. Typically, 50 mL of ethanol, 5 mL of ammonium hydroxide corresponding to $[NH_3]$ = 1 M, then 5 mL of silica seed aqueous suspension were mixed in a 150 mL round beaker. The concentration in silica beads was determined by dry extract. A volume of 765 μL of EDPS aqueous solution corresponding to an excess of 20 compared with the grafting density of EDPS was quickly added into the previous silica suspension under magnetic stirring. The reaction mixture was stirred overnight. Then the mixture was washed by centrifugation at 15 000*g* for 20 min. The supernatant containing ethanol and oligomers of silanes was removed, and the bottom containing the modified particles was redispersed in absolute ethanol by sonication. This washing step was repeated five times. After removal of the last supernatant, the bottom was redispersed in 100 mL of deionized water and the pH of the solution was adjusted to 5.

The Ag NPs were synthesized by using a previously reported method.[63] First, a solution of NaHS (30 mM) and a solution of PVP (30 mg/L) in EG were prepared separately. The two solutions were left to age for 4 h under stirring. A 60 mL sample of EG was then introduced in a rounded flask mounted with a reflux condenser and heated at 150 °C for 2.5 h under stirring. Two hours later, argon flow was introduced. After 30 min, 35 μL of the aged NaHS solution and 15 mL of the PVP solution were injected in the reaction medium. Then, 5 mL of a $AgNO_3$ solution (0.16 M) in EG was quickly introduced. The solution turned yellow immediately. After 7 min, the reaction was quenched by quickly cooling the reaction flask in an ice bath. Finally, the Ag NPs were washed by centrifugation at 40 000*g* for 2 h and redispersed in ethanol. This centrifugation cycle was repeated twice. The mass concentration of silver NPs was determined by ICP-OES.

Typically, 0.2 mL of a diluted suspension of silica beads was dropwise introduced into 1 mL of the Ag nanoparticle solution. The silica bead solution was diluted such that the ratio concentration [SiO_2 beads]/[Ag] was about 1/100. The mixture was stirred overnight. Then the solution was diluted in 30 mL of an aqueous PVP solution (0.5 g/L). After 2 h, the mixture was washed three times by centrifugation at 3000*g* for 20 min and redispersed in water. The resulting SiO_2@Ag nanostructures were once again centrifuged at 3000*g* for 20 min and redispersed in ethanol. Typically, 60 μL of ammonia was added to 5 mL of the SiO_2@Ag suspension. Under stirring, 100 μL of a TEOS solution diluted in ethanol (1 vol %) was slowly added with an automatic syringe pump. The addition rate was fixed at 0.5 mL/h. The reaction mixture was stirred for 12 h at ≈20 °C. Upon completion of the growth of the silica shell, the particles were washed twice by centrifugation with ethanol.

Ag@SiO_2 Core−Shell NPs. The previously synthesized Ag nanoparticles were coated with silica by using a previously reported method.[63] Typically 3.75 mL of the Ag nanoparticle dispersion was mixed under continuous magnetic stirring with a solution of deionized water and ammonia, at a volume ratio of 93.8/5/1.2 for absolute ethanol, water, and ammonia, respectively. Then, 70 μL of TEOS was added, and the reaction mixture was stirred for 12 h at 20 °C. Upon completion of the growth of silica shell, the particles were washed by centrifugation with ethanol and finally redispersed in water.

Microfluidic Evaporation Cell. All structures were created using standard soft photolithography techniques. A master template was made with a photocurable resist which was then molded in PDMS and cured at high temperature. This elastomeric core was peeled off the template and punched to create an opening for the reservoir, either a polyethylene tubing or simply a large opening of 4 mm diameter; the body of the chip was then sealed with a thin PDMS membrane of thickness $e \approx 1020$ mm, and either the gradient technique or plasma activation was used to firmly bind the two elements. We used microscope slides to cover specific areas of the membrane where we wanted to suppress permeation and thus define the length L_0.[48]

Conflict of Interest: The authors declare no competing financial interest.

Acknowledgment. We are grateful to P. Barois, A. Aradian, A. Veltri, M. Albani, A. Grigorenko, and P. Maestro for fruitful comments and permanent enthusiasm, and to P. Poulin for kindly providing us with dispersions of carbon nanotubes. This work has been done within Long-Term-Project SC2267 at ESRF (European Synchrotron Radiation Facility, Grenoble, France) and received fundings from the European Union's Seventh Framework Programme (FP7/2008) under Grant Agreement No. 228762 and from Région Aquitaine.

Supporting Information Available: Simplified model accouting for the competition between evaporation-induced concentration and precipitation kinetics. Details concerning the synthesis of gold nanorods. This material is available free of charge *via* the Internet at http://pubs.acs.org.

REFERENCES AND NOTES

1. Talapin, D. V.; Lee, J. S.; Kovalenko, M. V.; Shevchenko, E. V. Prospects of Colloidal Nanocrystals for Electronic and Optoelectronic Applications. *Chem. Rev.* **2010**, *110*, 389–458.
2. Guerrero-Martinez, A.; Grzelczak, M.; Liz-Marzan, L. M. Molecular Thinking for Nanoplasmonic Design. *ACS Nano* **2012**, *6*, 3655–3662.
3. Engheta, N.; Salandrino, A.; Alú, A. Circuit Elements at Optical Frequencies: Nanoinductors, Nanocapacitors, and Nanoresistors. *Phys. Rev. Lett.* **2005**, *95*, 095504.
4. Boneschanscher, M. P.; Evers, W. H.; Qi, W.; Meeldijk, J. D.; Dijkstra, M.; Vanmaekelbergh, D. Electron Tomography Resolves a Novel Crystal Structure in a Binary Nanocrystal Superlattice. *Nano Lett.* **2013**, *13*, 1312–1316.
5. Nie, Z.; Petukhova, A.; Kumacheva, E. Properties and Emerging Applications of Self-Assembled Structures Made from Inorganic Nanoparticles. *Nat. Nanotechnol.* **2010**, *5*, 15–25.
6. Vanmaekelbergh, D. Self-Assembly of Colloidal Nanocrystals as Route to Novel Classes of Nanostructured Materials. *Nano Today* **2011**, *6*, 419–437.
7. Majetich, S.; Wen, T.; Booth, R. Functional Magnetic Nanoparticle Assemblies: Formation, Collective Behavior, and Future Directions. *ACS Nano* **2011**, *5*, 6081–6084.

8. Bao, N.; Gupta, A. Self-Assembly of Superparamagnetic Nanoparticles. *J. Mater. Res.* **2011**, *26*, 111–121.
9. Labastide, J. A.; Baghgar, M.; Dujovne, I.; Yang, Y.; Dinsmore, A. D.; Sumpter, B. G.; Venkataraman, D.; Barnes, M. D. Polymer Nanoparticle Super Lattices for Organic Photovoltaic Applications. *J. Phys. Chem. Lett.* **2011**, *2*, 3085–3091.
10. Gong, J.; Li, G.; Tang, Z. Self-Assembly of Noble Metal Nanocrystals: Fabrication, Optical Property, and Application. *Nano Today* **2012**, *7*, 564–585.
11. Grzelczak, M.; Liz-Marzan, L. M. Colloidal Nanoplasmonics: From Building Blocks to Sensing Devices. *Langmuir* **2013**, *29*, 4652–4663.
12. Bishop, K. J.; Wilmer, C. E.; Soh, S.; Grzybowski, B. A. Nanoscale Forces and Their Uses in Self-Assembly. *Small* **2009**, *5*, 1600–1630.
13. Shevchenko, E. V.; Talapin, D. V.; Kotov, N. A.; O'Brien, S.; Murray, C. B. Structural Diversity in Binary Nanoparticle Superlattices. *Nature* **2006**, *439*, 55–59.
14. Kimura, K.; Pradeep, T. Functional Noble Metal Nanoparticle Superlattices Grown at Interfaces. *Phys. Chem. Chem. Phys.* **2011**, *13*, 19214–19225.
15. Jones, M. R.; Macfarlane, R. J.; Lee, B.; Zhang, J.; Young, K. L.; Senesi, A. J.; Mirkin, C. A. DNA-Nanoparticle Superlattices Formed from Anisotropic Building Blocks. *Nat. Mater.* **2010**, *9*, 913–917.
16. Wang, Y.; Dai, Q.; Wang, L.; Zou, B.; Cui, T.; Liu, B.; Yu, W. W.; Hu, M. Z.; Zou, G. Mutual Transformation between Random Nanoparticles and Their Superlattices: The Configuration of Capping Ligand Chains. *J. Phys. Chem. C* **2010**, *114*, 11425–11429.
17. Feng, W.; Sun, L. D.; Yan, C. H. Role of Surface Ligands in the Nanoparticle Assemblies: A Case Study of Regularly Shaped Colloidal Crystals Composed of Sodium Rare Earth Fluoride. *Langmuir* **2011**, *27*, 3343–3347.
18. Coppel, Y.; Spataro, G.; Colliere, V.; Chaudret, B.; Mingotaud, C.; Maisonnat, A.; Kahn, M. L. Self-Assembly of ZnO Nanoparticles—An NMR Spectroscopic Study. *Eur. J. Inorg. Chem.* **2012**, *2012*, 2691–2699.
19. Walker, D. A.; Browne, K. P.; Kowalczyk, B.; Grzybowski, B. A. Self-Assembly of Nano-Triangle Superlattices Facilitated by Repulsive Electrostatic Interactions. *Angew. Chem., Int. Ed.* **2010**, *49*, 6760–6763.
20. Young, K. L.; Jones, M. R.; Zhang, J.; Macfarlane, R. J.; Esquivel-Sirvent, R.; Nap, R. J.; Wu, J.; Schatz, G. C.; Lee, B.; Mirkin, C. A. Assembly of Reconfigurable One-Dimensional Colloidal Superlattices Due to a Synergy of Fundamental Nanoscale Forces. *Proc. Natl. Acad. Sci. U.S.A.* **2012**, *109*, 2240–2245.
21. Rupich, S. M.; Shevchenko, E. V.; Bodnarchuk, M. I.; Lee, B.; Talapin, D. V. Size-Dependent Multiple Twinning in Nanocrystal Superlattices. *J. Am. Chem. Soc.* **2010**, *132*, 289–296.
22. Goubet, N.; Richardi, J.; Albouy, P. A.; Pileni, M. P. Which Forces Control Supracrystal Nucleation in Organic Media? *Adv. Funct. Mater.* **2011**, *21*, 2693–2704.
23. Kalsin, A. M.; Fialkowski, M.; Paszewski, M.; Smoukov, S. K.; Bishop, K. J. M.; Grzybowski, B. A. Electrostatic Self-Assembly of Binary Nanoparticle Crystals with a Diamond-like Lattice. *Science* **2006**, *312*, 420–424.
24. Talapin, D. V.; Shevchenko, E. V.; Bodnarchuk, M. I.; Ye, X.; Chen, J.; Murray, C. B. Quasicrystalline Order in Self-Assembled Binary Nanoparticle Superlattices. *Nature* **2009**, *461*, 964–967.
25. Cheng, W.; Campolongo, M. J.; Tan, S. J.; Luo, D. Free-standing Ultrathin Nano-Membranes *via* Self-Assembly. *Nano Today* **2009**, *4*, 482–493.
26. Henzie, J.; Grunwald, M.; Widmer-Cooper, A.; Geissler, P. L.; Yang, P. Self-Assembly of Uniform Polyhedral Silver Nanocrystals into Densest Packings and Exotic Superlattices. *Nat. Mater.* **2012**, *11*, 131–137.
27. Martin, A.; Schopf, C.; Pescaglini, A.; O'Riordan, A.; Iacopino, D. Synthesis, Optical Properties and Self-Assembly of Gold Nanorods. *J. Exp. Nanosci.* **2012**, *7*, 688–702.
28. Hanrath, T.; Choi, J. J.; Smilgies, D. M. Structure/Processing Relationships of Highly Ordered Lead Salt Nanocrystal Superlattices. *ACS Nano* **2009**, *3*, 2975–2988.
29. Huang, T.; Zhao, Q.; Xiao, J.; Qi, L. Controllable Self-Assembly of PbS Nanostars into Ordered Structures: Close-Packed Arrays and Patterned Arrays. *ACS Nano* **2010**, *4*, 4707–4716.
30. Grzelczak, M.; Vermant, J.; Furst, E. M.; Liz-Marzan, L. M. Directed Self-Assembly of Nanoparticles. *ACS Nano* **2010**, *4*, 3591–3605.
31. Deegan, R. D.; Bakajin, O.; Dupont, T. F.; Huber, G.; Nagel, S. R.; Witten, T. A. Capillary Flow as the Cause of Ring Stains from Dried Liquid Drops. *Nature* **1997**, *389*, 827–829.
32. Tekin, E.; Smith, P. J.; Schubert, U. S. Inkjet Printing as a Deposition and Patterning Tool for Polymers and Inorganic Particles. *Soft Matter* **2008**, *4*, 703–713.
33. Prevo, B. G.; Kuncicky, D. M.; Velev, O. D. Engineered Deposition of Coatings from Nano- and Micro-Particles: A Brief Review of Convective Assembly at High Volume Fraction. *Colloids Surf., A* **2007**, *311*, 2–10.
34. Kumnorkaew, P.; Ee, Y. K.; Tansu, N.; Gilchrist, J. F. Investigation of the Deposition of Microsphere Monolayers for Fabrication of Microlens Arrays. *Langmuir* **2008**, *24*, 12150–12157.
35. Yang, S. M.; Miguez, H.; Ozin, G. A. Opal Circuits of Light Planarized Microphotonic Crystal Chips. *Adv. Funct. Mater.* **2002**, *12*, 425–431.
36. Podsiadlo, P.; Krylova, G. V.; Demortiere, A.; Shevchenko, E. V. Multicomponent Periodic Nanoparticle Superlattices. *J. Nanopart. Res.* **2011**, *13*, 15–32.
37. Curri, M. L.; Comparelli, R.; Striccoli, M.; Agostiano, A. Emerging Methods for Fabricating Functional Structures by Patterning and Assembling Engineered Nanocrystals. *Phys. Chem. Chem. Phys.* **2010**, *12*, 11197–11207.
38. Taheri, S. M.; Fischer, S.; Trebbin, M.; With, S.; Schroeder, J. H.; Perlich, J.; Roth, S. V.; Foerster, S. Lyotropic Phase Behavior of Polymer-Coated Iron Oxide Nanoparticles. *Soft Matter* **2012**, *8*, 12124–12131.
39. Bodnarchuk, M. I.; Li, L.; Fok, A.; Nachtergaele, S.; Ismagilov, R. F.; Talapin, D. V. Three-Dimensional Nanocrystal Superlattices Grown in Nanoliter Microfluidic Plugs. *J. Am. Chem. Soc.* **2011**, *133*, 8956–8960.
40. Akey, A.; Lu, C.; Yang, L.; Herman, I. Formation of Thick, Large-Area Nanoparticle Superlattices in Lithographically Defined Geometries. *Nano Lett.* **2010**, *10*, 1517–1521.
41. Chattopadhyay, S.; Mukherjee, R.; Datta, A.; Saha, A.; Sharma, A.; Kulkarni, G. U. Self-Assembly of a Two-Dimensional Au-Nanocluster Superlattice and Its Photoluminescence Spectra. *J. Nanosci. Nanotechnol.* **2009**, *9*, 190–194.
42. Cheng, W.; Campolongo, M. J.; Cha, J. J.; Tan, S. J.; Umbach, C. C.; Muller, D. A.; Luo, D. Free-Standing Nanoparticle Superlattice Sheets Controlled by DNA. *Nat. Mater.* **2009**, *8*, 519–525.
43. Chen, Y.; Fu, J.; Ng, K. C.; Tang, Y.; Cheng, W. Free-Standing Polymer-Nanoparticle Superlattice Sheets Self-Assembled at the Air Liquid Interface. *Cryst. Growth Des.* **2011**, *11*, 4742–4746.
44. Leng, J.; Lonetti, B.; Tabeling, P.; Joanicot, M.; Ajdari, A. Microevaporators for Kinetic Exploration of Phase Diagrams. *Phys. Rev. Lett.* **2006**, *96*, 084503.
45. Leng, J.; Salmon, J.-B. Microfluidic Crystallization. *Lab Chip* **2009**, *9*, 24–34.
46. Salmon, J.-B.; Leng, J. Detailed Functioning of Microevaporators and of Their Application to the Dynamic Exploration of Phase Diagram. *J. Appl. Phys.* **2010**, 084905.
47. Merlin, A.; Angly, J.; Daubersies, L.; Madeira, C.; Schoeder, S.; Leng, J.; Salmon, J.-B. Time-Resolved Microfocused Small-Angle X-ray Scattering Investigation of the Microfluidic Concentration of Charged Nanoparticles. *Eur. Phys. J. E* **2011**, *34*, 58.
48. Merlin, A.; Salmon, J.-B.; Leng, J. Microfluidic-Assisted Growth of Colloidal Crystals. *Soft Matter* **2012**, *8*, 3526–3537.
49. Daubersies, L.; Leng, J.; Salmon, J.-B. Steady and Out-of-Equilibrium Phase Diagram of a Complex Fluid at the Nanoliter Scale: Combining Microevaporation, Confocal Raman Imaging and Small Angle X-ray Scattering. *Lab Chip* **2012**, *13*, 910–919.

50. Kim, E.; Xia, Y. N.; Whitesides, G. M. Two- and Three-Dimensional Crystallization of Polymeric Microspheres by Micromolding in Capillaries. *Adv. Mater.* **1996**, *8*, 245.
51. Shiu, J. Y.; Kuo, C. W.; Chen, P. Actively Controlled Self-Assembly of Colloidal Crystals in Microfluidic Networks by Electrocapillary Forces. *J. Am. Chem. Soc.* **2004**, *126*, 8096–8097.
52. Schindler, M.; Ajdari, A. Modeling Phase Behavior for Quantifying Micro-Pervaporation Experiments. *Eur. Phys. J. E* **2009**, *28*, 27–45.
53. Noblin, X.; Mahadevan, L.; Coomaraswamy, I. A.; Weitz, D. A.; Holbrook, N. M.; Zwieniecki, M. A. Optimal Vein Density in Artificial and Real Leaves. *Proc. Natl. Acad. Sci. U.S.A.* **2008**, 9140–9144.
54. Wheeler, T. D.; Stroock, A. D. The Transpiration of Water at Negative Pressures in a Synthetic Tree. *Nature* **2008**, *455*, 208–212.
55. Russel, W. B.; Saville, D. A.; Schowalter, W. R. *Colloidal Dispersions*; Cambridge University Press: Cambridge, UK, 1992.
56. Sirota, E. B.; Ou-Yang, H. D.; Sinha, S. K.; Chaikin, P. M.; Axe, J. D.; Fujii, Y. Complete Phase Diagram of a Charged Colloidal System: A Synchrotron X-ray Scattering Study. *Phys. Rev. Lett.* **1989**, *62*, 1524.
57. Forster, S.; Timmann, A.; Konrad, M.; Schellbach, C.; Meyer, A.; Funari, S. S.; Mulvaney, P.; Knott, R. Scattering Curves of Ordered Mesoscopic Materials. *J. Phys. Chem. B* **2005**, *109*, 1347–1360.
58. Forster, S.; Timmann, A.; Schellbach, C.; Fromsdorf, A.; Kornowski, A.; Weller, H.; Roth, S. V.; Lindner, P. Order Causes Secondary Bragg Peaks in Soft Materials. *Nat. Mater.* **2007**, *6*, 888–893.
59. Davis, K. E.; Russel, W. B.; Glantschnig, W. J. Settling Suspensions of Colloidal Silica: Observations and X-ray Measurements. *J. Chem. Soc., Faraday Trans.* **1991**, *87*, 411–424.
60. Hung, A. M.; Konopliv, N. A.; Cha, J. N. Solvent-Based Assembly of CdSe Nanorods in Solution. *Langmuir* **2011**, 12322–12328.
61. Xie, Y.; Guo, S.; Ji, Y.; Guo, C.; Liu, X.; Chen, Z.; Wu, X.; Liu, Q. Self-Assembly of Gold Nanorods into Symmetric Superlattices Directed by OH-Terminated Hexa(ethylene glycol) Alkanethiol. *Langmuir* **2011**, 11394–11400.
62. Hamon, C.; Postic, M.; Mazari, E.; Bizien, T.; Dupuis, C.; Even-Hernandez, P.; Jimenez, A.; Courbin, L.; Gosse, C.; Artzner, F.; *et al.* Three-Dimensional Self-Assembling of Gold Nanorods with Controlled Macroscopic Shape and Local Smectic B Order. *ACS Nano* **2012**, *6*, 4137–4146.
63. Massé, P.; Mornet, S.; Duguet, E.; Tréguer-Delapierre, M.; Ravaine, S.; Iazzolino, A.; Salmon, J.-B.; Leng, J. Synthesis of Size-Monodisperse Spherical Ag@SiO_2 Nanoparticles and 3D Assembly Assisted by Microfluidics. *Langmuir* **2013**, *29*, 1790–1795.
64. Brewer, D. D.; Allen, J.; Miller, M. R.; de Santos, J. M.; Kumar, S.; Norris, D. J.; Tsapatsis, M.; Scriven, L. E. Mechanistic Principles of Colloidal Crystal Growth by Evaporation-Induced Convective Steering. *Langmuir* **2008**, *24*, 13683–13693.
65. Gasperino, D.; Meng, L.; Norris, D. J.; Derby, J. J. The Role of Fluid Flow and Convective Steering during the Assembly of Colloidal Crystals. *J. Cryst. Growth* **2008**, *310*, 131–139.
66. Muehlig, S.; Cunningham, A.; Scheeler, S.; Pacholski, C.; Buergi, T.; Rockstuhl, C.; Lederer, F. Self-Assembled Plasmonic Core−Shell Clusters with an Isotropic Magnetic Dipole Response in the Visible Range. *ACS Nano* **2011**, *5*, 6586–6592.
67. Enustun, B.; Turkevich, J. Coagulation of Colloidal Gold. *J. Am. Chem. Soc.* **1963**, *85*, 3317.
68. Jana, N. Gram-Scale Synthesis of Soluble, Near-Monodisperse Gold Nanorods and Other Anisotropic Nanoparticles. *Small* **2005**, *1*, 875–882.
69. Thierry, B.; Ng, J.; Krieg, T.; Griesser, H. A Robust Procedure for the Functionalization of Gold Nanorods and Noble Metal Nanoparticles. *Chem. Commun.* **2009**, 1724–1726.
70. Désert, A.; Chaduc, I.; Fouilloux, S.; Taveau, J.-C.; Lambert, O.; Lansalot, M.; Bourgeat-Lami, E.; Thill, A.; Spalla, O.; Ravaine, S.; *et al.* High-Yield Preparation of Polystyrene/Silica Clusters of Controlled Morphology. *Polym. Chem.* **2012**, *3*, 1130–1132.

Chapter 5

Bulk optical metamaterials assembled by microfluidic evaporation

We saw in the previous chapters that for given conditions, we can build solids made of densely packed NPs. As the goal of the METACHEM project is to demonstrate that these materials have interesting optical properties, a complete characterization should be performed. In this chapter, I introduce the technique we used (microspot ellipsometry) in close collaboration with V. Kravets and A. Grigorenko (University of Manchester) and with A. Aradian, P. Barois, A. Baron, K. Ehrhardt (CRPP, Pessac). More specifically, I describe the constraints that emerge from the coupling between the small size of our materials and the optical requirements; the analysis and interpretation of the ellipsometry experiments were performed by our collaborators.

Having optimized the experimental conditions in order to be able to measure a refractive index after growth, we grew and analyzed two main types of materials: solids made of metallics NPs capped with a polymer or covered with silica. The main difference in the final solid comes from the volume fraction occupied by the metal. For the most concentrated samples where electrical coupling exists between the NPs, the materials display an extremely high refractive index in the near infra-red regime and might be interesting candidates for optical composites. The analysis and the optical results are discussed in the paper pasted at the end of this chapter.

5.1 Design of a chip for ellipsometry

In an ellipsometry experiment, a beam of white ligth shines the sample and one measures the change of polarisation of the reflected light. The size of the ligth spot must be smaller than the one of the channel in which we want to perform measurements. For microspots, the diameter of the beam (Fig. 5.1) is $w_s = 80\mu$m which imposes channels with a minimal width of $w \approx 100\,\mu$m; the fingerprint of the beam on the substrate is $l_s = w_s/\cos\theta \approx 230\,\mu$m at 70°. Together, w_s and l_s impose the minimum spatial extent of the sample.

The width of the channel also fixes the height we can manufacture because PDMS

is soft, especially the thin membrane of the devices, and we can build channels with an aspect ratio $w/h \sim 10$, thus $h \approx 10\,\mu$m. It makes evaporation slow (the thicker the slower, $t_e = h/v_e$, where v_e is fixed by the thickness of the membrane). As we work with dilute dispersions but still wish to build materials out of them, we want to drive as much of the dispersion inside the channel, and we compensate the relatively slow evaporation rate with a *very* long evaporation channel: we used here $L_0 = 11\,$cm.

To fit this long channel on a small surface, we bend it as a serpentine and leave its tip far from the rest of the chip (Fig. 1.27, page 33) in order not have influence of the rest of the geometry during optical experiments.

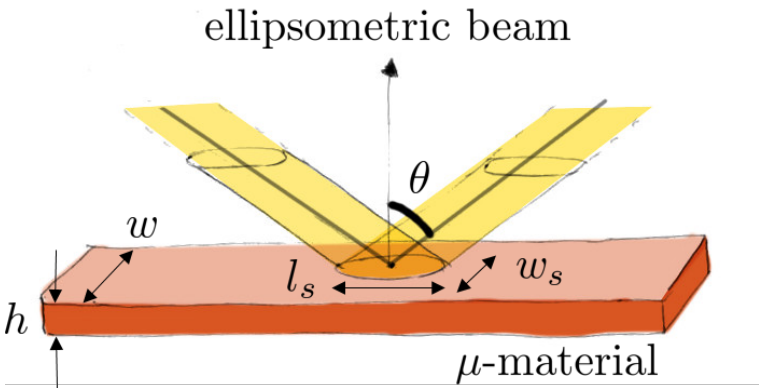

Figure 5.1: Schematic view of the ellipsometric beam impinging a micromaterial (drawing J. Leng). The size of the spot w_s fixes the minimum width w of the channel which in turn imposes a given height h because of microfabrication constraints.

5.2 Measurement of refractive index

Ellipsometry measures the change of polarization of a beam which impinges a surface, which is reflected and also transmitted. The transmitted beam may be reflected onto the bottom face of the sample and recombine with the first reflected one. It leads to interferences and makes the analysis of the experiments numerical only; if the sample is semi-infinite (no secondary beam), there is an analytical solution which leads to a direct measurement of the refractive index of the material [37].

Our materials are not semi-infinite but they absorb light, which may also suppress the secondary beam. A simple way to estimate whether the transmited light is totally attenuated or not is to define the penetration length $\xi = \lambda/(2\pi k)$ where k is the imaginary part of the refractive index. We want to have $h/\xi \gg 1$, so $k \gg (h/\lambda)2\pi$. At $\lambda = 500\,$nm and for $h = 10\,\mu$m, we get $k \gg 0.01$ in order to satisfy the semi-infinite medium assumption. We will see that it is nearly allways the case as k ranges around $0.1 - 4$.

5.3 Materials

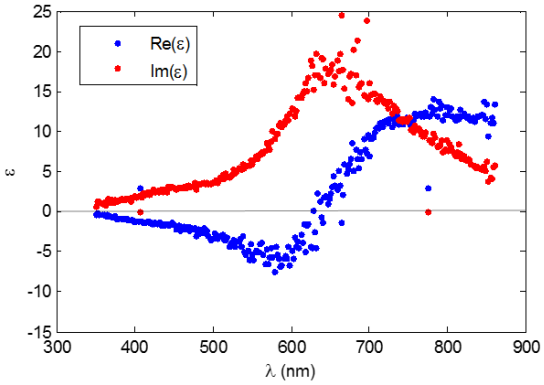

Figure 5.2: Relative permittivity of a material made of densely packed SiO_2@PVP nanocubes.

We fabricated dense states of NPs of two natures: silica and polymer protected metallic NPs. The number of particles per height of channel is $h/a \approx 200 - 600$, which is considerable, among the thickest materials produced artificially in the frame of metamaterials, and they are thus considered as quite bulky. Their upper face is flat enough and we do not consider their surface roughness in ellipsometry.

For silica based NPs, we assume that the total filling fraction is ≈ 0.6 but the metal volume fraction is diminished by a factor $(R_i/R_o)^3$ with the inner (core) and outer (core + shell) radii, which gives typically $\phi_{metal} \approx 0.5 - 1\%$ depending on the NPs; the load of metal in the final material is thus very small. The spacing between cores is given by the silica shell and is of order of the core diameters. Nps are thus too far apart to interact strongly and the final material should behave only as weakly concentrated NPs, which we observe indeed. Fig. 2 b and d of the article shows the refractive index of these materials where the plasmon band (for k) is exactly at the same position as for the dispersion (no electrical coupling) and for which the theory of Maxwell-Garnett should apply well. The fit is actually a phenomenological analysis for resonating structures.

For polymer based NPs, SEM image analysis shows that the final volume fraction is much higher $\approx 0.3 - 0.4$. Because the polymer shell is thin, the distance between NPs is small, a few nm only, and the NPs are strongly coupled. We show in the article that there is still a plasmon band for these materials and it is significantly red-shifted ($\Delta\lambda = 200\,\text{nm}$) because of the coupling (Fig. 2 a and c). This absorption band remains fairly peaked which suggests that a well defined collective mode exists.

Interestingly, the refractive index in the near infra-red band is really high ($n = 3 - 4$), actually among the highest we could find. However, attenuation is also significant, which means that as bulk materials, they are not usable for optics. However, we can think of them as really usefull as thin coatings [38], and also maybe for the fabrication of photonic

crystals where large colloids could be assembled to form a lattice then infiltrated with the NP dispersion in order to boost the index contrast, which is required for having interesting properties such as band gaps [39].

5.4 Perspectives

The composite materials we can fabricate and characterize are promising. We can obtain very densely packed arrays of NPs and we can characterize their optical properties. Here, the most concentrated systems display a plasmonic resonance with a very high refractive index in the near infra-red regime. Before the resonance, we expect to have $\epsilon < 0$: we thus calculate the permittivity $\epsilon = n^2$ assuming that their is no permeability ($\mu = 1$). The corresponding values for the SiO_2@PVP nanocubes material shows that the material indeed has a negative permittivity below resonance (Fig. 5.2), that is here for $\lambda < 600\,\text{nm}$. It stems from the metallic properties of NPs and provides a control over one part of the refractive index. It could be interesting to build a composite material with a tunable concentration of NPs (by adding more polymer) in order to better design ϵ. In order to reach $n < 0$, of course one should control μ. It is meant to be possible by using raspberry-like NPs and we evidenced that it is possible to make dense solids out of these particles. The next step will be to extract the refractive index of these materials, to evidence with ellipsometry that $\mu \neq 1$, and eventually to combine the raspberries with metallic NPs to get a full control over n.

Bulk optical metamaterials assembled by microfluidic evaporation

Alexandre Baron,[1,2,*] Antonio Iazzolino,[3] Kévin Ehrhardt,[1,2] Jean-Baptiste Salmon,[3] Ashod Aradian,[1,2] Vasyl Kravets,[4] Alexander N. Grigorenko,[4] Jacques Leng,[3] Aurélie Le Beulze,[5] Mona Tréguer-Delapierre,[5] Miguel A. Correa-Duarte,[6] and Philippe Barois[1,2]

[1]*CNRS, CRPP, UPR8641, F-33600, Pessac, France*
[2]*Univ. Bordeaux, CRPP, UPR8641, F-33600, Pessac, France*
[3]*CNRS, University of Bordeaux, RHODIA, LOF, UMR5258, F-33600, Pessac, France*
[4]*University of Manchester, School of Physics and Astronomy, Manchester, United Kingdom*
[5]*CNRS, ICMCB, UPR9048, F-33600, Pessac, France*
[6]*Departamento de Quimica Fisica, Universidad de Vigo,36310, Vigo, Spain*
[*]*baron@crpp-bordeaux.cnrs.fr*

Abstract: We present high refractive index optical metamaterials assembled via a microfluidic evaporation technique. This technique enables fabrication of truly three-dimensional bulk samples from a suspension of nanoparticles with a number of layers well in excess of 600, surpassing rival techniques by at least an order of magnitude. In addition to their large dimensions, the assembled metamaterials show a high degree of homogeneity and warrant an easy and rapid optical characterization using spectroscopic ellipsometry. We believe that the suggested inexpensive method considerably reduces the complexity in assembling optical metamaterials and opens new avenues in engineering bulk optical devices by choice of nanoparticle composition and geometry.

OCIS codes: (160.0160) Materials; (160.3918) Metamaterials; (160.4236) Nanomaterials; (240.2130) Ellipsometry and polarimetry.

References and links

1. C. M. Soukoulis, and M. Wegener, "Past achievements and future challenges in the development of three-dimensional photonic metamaterials," Nature Photon. **5**, 523-530 (2011).
2. N. Liu, H. Guo, L. Fu, S. Kaiser, H. Schweizer, and H. Giessen, "Three-dimensional photonic metamaterials at optical frequencies," Nature Mater. **7**, 31-37 (2008).
3. J. K. Gansel, M. Thiel, M. S. Rill, M. Decker, K. Bade, V. Saile, G. v. Freymann, S. Linden, M. Wegener, "Gold helix photonic metamaterial as broadband circular polarizer," Science **325**, 1513-1515 (2009).
4. J. Valentine, S. Zhang, T. Zentgraf, E. Ulin-Avila, D. A. Genov, G. Bartal , and X. Zhang, "Three-dimensional optical metamaterial with a negative refractive index," Nature **455**, 376-379 (2008).
5. T. Xu, A. Agrawal, M. Abashin, K. J. Chau, and H. Lezec, "All-negative refraction and active flat lensing of ultraviolet light," Nature **497**, 470-474 (2013).
6. S. Mühlig, c. Rockstuhl, V. Yannopapas, T. Bürgi, N. Shalkevich, and F. Lederer, "Optical properties of fabricated self-assembled bottom-up bulk metamaterial," Opt. Express **19**, 9607-9616 (2011).
7. L. Malassis, P. Massé, M. Tréguer-Delapierre, S. Mornet, P. Weisbecker, V. Kravets, A. Grigorenko, and P. Barois, "Bottom-up fabrication and optical characterization of dense films of meta-atoms made of core-shell plasmonic nanoparticles," Langmuir **29**, 1551-1561 (2013).
8. A. Merlin, J.-B. Salmon, and J. Leng, "Microfluidic-assisted growth of colloidal crystals," Soft Matter **8**, 3526-3537 (2012).
9. T. Nakamura, H. Fuji, N. Juni, and N. Tsutsumi, "Enhanced coupling of light from organic electroluminescent device using diffusive particle dispersed high refractive index resin substrate," Opt. Rev. **13**, 104-110 (2006).
10. D. W. Mosley, K. Auld, D. Conner, J. Gregory, X. Q. Liu, A. Pedicini, D. Thorsen, M. Wills, G. Khanarian, and E. S. Simon, "High-performance encapsulants for ultra high-brightness LEDs," Proc. SPIE **6910**, 691017 (2008).
11. K. C. Krogman, T. Druffel, and M. K. Sunkara, "Anti-reflective optical coatings incorporating nanoparticles," Nanotechnology **16**, S338-S343 (2005).

12. J. L. Regolini, D. Benoit, and P. Morin, "Passivation issues in active pixel CMOS image sensors," Microelectron. Reliab. **47**, 739-742 (2007).
13. P. Massé, S. Mornet, E. Duguet, M. Treguer-Delapierre, S. Ravaine, A. Iazzolino, J.-B. Salmon, and J. Leng, "Synthesis of size-monodisperse spherical Ag@SiO2 nanoparticles and 3-D assembly assisted by microfluidics," Langmuir **29**, 1790-1795 (2013).
14. C. Fernandez-Lopez, C. Mateo-Mateo, R. A. Alvarez-Puebla, J. Perez-Juste, I. Pastoriza-Santos, and L. M. Liz-Marzan, "Highly controlled silica coating of PEG-capped metal nanoparticles and preparation of SERS-encoded particles," Langmuir **25**, 13894-13899 (2009).
15. H. Fujiwara, Spectroscopic Ellipsometry: Principles and Applications, John Wiley and Sons Inc (2007).
16. G.E. Jellison, F. A. Modine, "Parametrization of the optical functions of amorphous materials in the interband region," Appl. Phys. Lett. **69**, 371-373 (1996).
17. J. Tauc, R. Grigorov, A. Vancu, "Optical properties and electronic structures of amorphous germanium," Phyic. Status Solidi **15**, 627-637 (1966).

1. Introduction

The demand for specific and peculiar optical properties that do not necessarily exist in natural materials arises in various domains that involve advanced optoelectronics. Optical metamaterials (OMMs) provide an excellent opportunity to tackle this demand by addressing their design at two different scales. On the one hand, the microscopic response of metamaterials can be tailored by carefully selecting and arranging individual nanostructures at the sub-wavelength scale. On the other hand, by organizing the individual resonators into a specific patterned layer and by subsequently stacking these layers together, the metamaterials reach a macroscopic regime. In this regime, the assembled medium can unambiguously be considered as homogeneous and thus exhibits an effective index of refraction. It is worth noting that in order for the assembled structures to qualify as homogeneous optical materials, two important conditions have to be met. First, the typical size a of the elementary cell needs to be smaller than the operating wavelength λ to justify homogenization. Second, the structure must have a thickness h that is large enough for it to be considered as bulk. *Soukoulis et al*. [1] provided an interesting discussion on how large a sample should be to reach the 3D-regime. It was argued that the bulk limit for a metamaterial is reached when the retrieved effective parameters extracted from optical measurements no longer depend on h. In 2008, OMMs made a firm transition from mere metasurfaces to actual bulk materials [2] and the ratios λ/a, which characterizes homogeneity, and h/a, which characterizes bulkiness, may be regarded as two important figures of merit (FOM) that should be as large as possible to assess OMMs.

The top-down fabrication platforms are well suited to precisely control the subwalength dimensions of the individual building blocks of the OMMs. However, they seem to be ill-adapted to reach large h/a values. Up to now, most achievements rarely exceed $h/a \sim 10$ and $\lambda/a \sim 5$ [2-5]. Moreover, most of these metamaterials operate in the near infrared with rare exceptions, such as *Xu et al*. [5] who built a device earlier this year, that demonstrates an all-angle negative refraction of ultraviolet light with modest $h/a \sim 3$ and $\lambda/a \sim 2.3$. Bottom-up fabrication, which combines chemical synthesis and self-assembly, offers an interesting alternative to build bulk OMMs [6,7]. In contrast to the top-down, bottom up procedures allow one to achieve a considerable improvement in the bulkiness ratio without compromising the elementary cell structure.

Here we present bulk OMMs assembled by a recently developed microfluidic evaporation scheme [8] which improves the bulkiness FOM by at least one order of magnitude reaching $h/a > 600$. Moreover, the homogeneity FOM achieved with our best assembled material is $\lambda/a \sim 40$. These OMMs are composed of gold or silver nanoparticles of cubic or spherical shapes as well as metal-dielectric core-shells. The localized surface plasmon resonance of these nanoobjects produces a strongly dispersive effective medium response when they are assembled. The geometry, size, metal-type and volume fraction of metal in the assembled medium all matter and constitute degrees of freedom to engineer the desired index of refraction. The fabricated OMMs demonstrate high refractive index values with low

absorption at the red-end of the visible spectrum and in the near-infrared. This property could be of interest for several applications such as high light-extraction substrates and encapsulants for ultra-bright OLEDs [9,10], sensors, telecom devices, antireflective coatings for advanced optical applications [11] or even micro-lens components for CCD, CMOS and CIS devices [12]. Furthermore, an important feature of our fabrication technique is that the resulting OMMs are conveniently contained in microfluidic channels and are ready to be used for fabrication of bulk optical devices. In addition, the high quality of the surfaces of the fabricated OMMs allows an easy optical characterization using spectroscopic ellipsometry.

2. Synthesis and assembly

We synthesize four types of nanoparticles: silver nanocubes (Ag-CU), Ag@SiO_2 cores-shells (Ag-CS), gold nanospheres (Au-SP) and Au@SiO_2 core-shells (Au-CS). For details on the synthesis of the nanoparticles, readers should refer to Ref. [13] for the Ag-CU particles and to Ref. [14] for the gold particles. The Ag-CS nanoparticles were purchased from NanoComposix and the size data are provided by the manufacturer. Figure 1(a-d) provides pictures of all the nanoparticles in solution. The Ag-CUs are 30 ± 1 nm in size. The Ag-CSs have a 50 nm ± 5 nm cored diameter with a silica shell thickness of 25 ± 5 nm. The Au-SPs are 13.5 ± 1 nm in diameter and are capped with a 5 kDa thiol-PEG ligand. The Au-CS have a 15.2 ± 2 nm core-diameter and a silica shell thickness of 8.5 ± 1 nm.

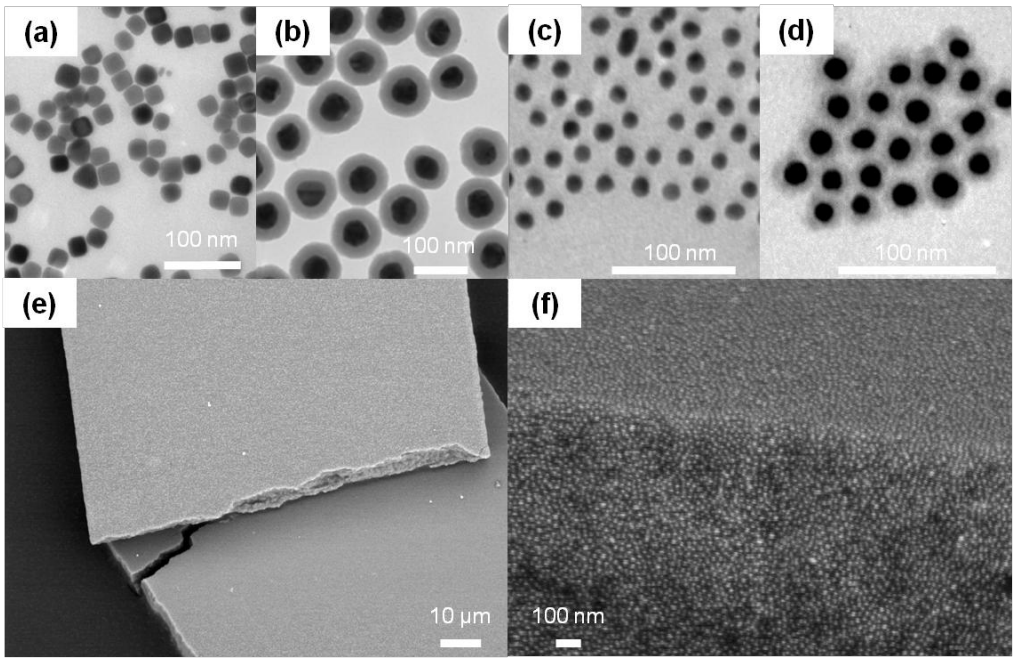

Fig. 1. Images of the nanoparticles and bulk optical metamaterials. TEM images of the individual metallic nanoresonators: (a) Ag cubes, (b) Ag core-shells (©Nanocomposix), (c) Au spheres and (d) Au core-shells. Typical SEM images of the metamaterials assembled via microfluidic evaporation: (e) slab of Ag core-shells and (f) close-up side-view of the edge of a slab of the assembled Au spheres.

The assembly technique we use is based on microfluidic evaporation and is described in length elsewhere [13]. In brief, using standard soft lithography, we fabricate a 10 µm × 100 µm × 10 mm rectangular microchannel. The channel is put in contact with a semi-permeable membrane and is connected to a reservoir (10-50 µL) containing the dilute dispersion. The solvent we use – in this work water – can evaporate across the membrane while the nanoparticles do not and therefore become trapped. As a result, the nanoparticles accumulate

in the microchannel. Upon sufficient accumulation time, a dense state of nanoparticles nucleates and invades the channel as it is continuously fed with from the reservoir. Interestingly, the solid adopts the *exact* shape of the microchannel in which it grows and thus exhibits flat interfaces and at least one long dimension. Typical pictures of the assembled OMMs are shown on Fig. 1(e,d). They have channel dimensions: a width of 100 μm, a depth h = 10 μm and are several millimeters long. As can be seen, the fabricated OMMs show very little surface roughness. A structural analysis using micro-focused X-ray scattering (not shown) demonstrates a limited local order. Therefore, we assume that the assembly is randomly close-packed so that the inter-particle distance is very small compared to the wavelength. In addition, if we consider an operation wavelength of λ = 600 nm which coincides (see section 4) with the localized plasmon resonances of the assembled Ag-CUs and Au-SPs, we find that the homogeneity FOM for our OMMs is equal to $\lambda/a \sim 20$ in the case of Ag-CUs. The same ratio is equal to 10 for the Ag-CS sample and reaches an impressive value of 40 for the case of the Au-SP and Au-CS nanoparticles. Furthermore these OMMs have a high degree of bulkiness with the ratio $h/a \sim 300$ for the Ag-CUs, $h/a \sim 200$ for the Ag-CSs and $h/a \sim 600$ for the gold samples. The large dimensions of the OMMs make them easy to characterize with spectroscopic ellipsometry.

3. Ellipsometric characterization

The optical measurements for the silver nanonoparticle OMMs are made using a Horiba Scientific ellipsometer at two incident angles θ = 60° and 70° in the 350-860 nm wavelength range. The incoming spot size is 80 μm. For the gold nanoparticle OMMs, the measurements are made with a J.A. Woollam ellipsometer in the 240-1000 nm wavelength range with a spot size of 30 μm. Each time, we acquire the spectrum of the complex ellipsometric quantity $\rho = r_p/r_s = \tan(\psi)\exp(-i\Delta)$ where r_p and r_s are the reflection coefficients for p- and s-polarized light, respectively, and (ψ, Δ) are the ellipsometric angles.

For light reflected by a bulk semi-infinite homogeneous and isotropic material, r_p and r_s are simply given by the Fresnel coefficients and the optical index $N = n + ik$ is expressed as a function of ρ. In this case the retrieval of N is immediate and the solution is unique. Therefore, when the incident medium is air, N is unambiguously given by:

$$N = \sin\theta \left\{ 1 + \left(\frac{1-\rho}{1+\rho} \right)^2 \tan^2\theta \right\}^{1/2}, \qquad (1)$$

where θ is the angle of incidence [15].

As was discussed in section 2, each sample is made of nanoparticles assembled in random close-packing order, so that the dimensions of the nanoresonators and their spacing are very small compared to the wavelength and the material is highly homogeneous. For each sample, we proceed in the same manner. The microchannels are 10 μm deep and the underlying medium is a semi-infinite PDMS substrate for which the optical properties are measured independently. First, we perform a numerical inversion using a multi-layer model containing the 10 μm OMM on top of the PDMS substrate and make sure that the retrieved N is identical to that found using Eq. (1). The fact that both indices of refraction coincide indicates that the OMM is indeed an optically semi-infinite medium. As a result, measuring ρ and using Eq. (1) can be regarded as a direct measurement of $n(\lambda)$ and $k(\lambda)$. The measured spectra $n(\lambda)$ and $k(\lambda)$ are represented by blue and red dots respectively in Fig. 2. Second, to check that our measured N are physical, we fit the ellipsometric parameters (ψ, Δ) using two Lorentz-oscillators (LO) to describe the dielectric constant ε of our MM. The dispersion relation given by the LO model classically describes the collective electron oscillations of localized surface plasmon resonances that occur in metallic nanoparticles embedded in a dielectric host medium. Since

the vicinity of each resonator is slightly different from one particle to another because of the randomness of the fabrication technique, so are the width and position of the individual responses. For this reason, a single LO may be insufficient to accurately fit the experimental data. For each medium the model used for the ω-frequency dependence of ε is

$$\varepsilon(\omega) = \varepsilon_{\infty} + \sum_{j=1}^{2} \frac{f_j \omega_{0j}^2}{\omega_{0j}^2 - \omega^2 + i\gamma_j \omega}, \qquad (2)$$

where f_j, ω_{0j} and γ_j are the oscillator strength, resonance frequency and damping constant. ε_{∞} is a constant. As the UV frequencies are approached, this classical model decreases in accuracy because of the interband transitions in the metal. For this reason, we append a Tauc-Lorentz oscillator (TLO) to Eq. (2), which was initially proposed by Jellison and Modine [16] and is accurate in describing the interband absorption. The Tauc-Lorentz model consists in multiplying the imaginary part of the dielectric function obtained from the Lorentz equation by the Tauc joint density of states [17]. Even though it was originally proposed to describe amorphous semiconductors, we observe empirically that it provides a reasonable fit to optical properties of metallic nanocomposites at the UV end of the visible spectrum. The data are fitted by using the χ^2-test. The fitted curves are represented by continuous lines in Fig 2.

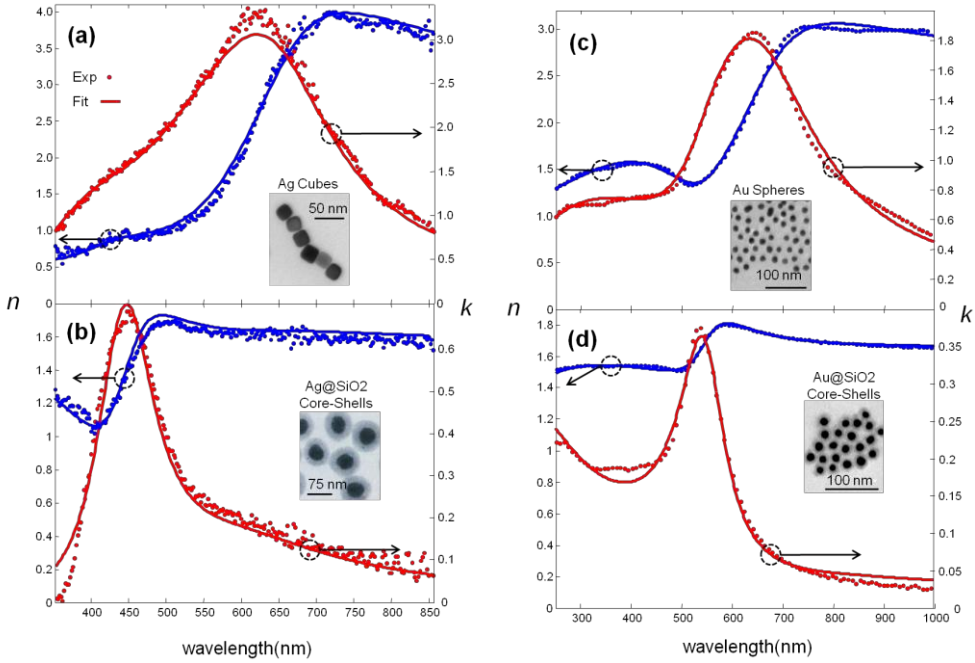

Fig. 2. Optical Properties of the bulk optical metamaterials. Each graph shows the spectral evolution of the measured real (blue) and imaginary (red) part of the optical index $N = n + ik$ for assembled (a) Ag cubes, (b) Ag core-shells, (c) Au spheres and (d) Au core-shells. Dots represent the values obtained by measuring $\rho(\lambda)$. The continuous lines represent the fits using the Lorentz-oscillator models for the dielectric constant of the metamaterial.

4. Results

Figure 2 shows the typical optical properties of the fabricated OMMs and compares the optical index N retrieved from Eq.(1) (dots) with the fitted models (continuous line) for the four types of nanoparticles. We can see that the agreement between the model and the retrieval data is excellent for all types of nanoparticles. Table 1 summarizes the converged fitting parameters for each OMM. The TLO parameters are described using the notations

given in Ref. [16]. From Table 1 we conclude that the main plasmon resonance of the assembled silver cubes and core-shells is observed at $\lambda_{Ag\text{-}CU}$ = 616 nm and $\lambda_{Ag\text{-}CS}$ = 450 nm with full-widths at half-maximum $\Delta\lambda_{Ag\text{-}CU}$ ~ 290 nm and $\Delta\lambda_{Ag\text{-}CS}$ ~ 160 nm respectively (see Fig. 2). It is interesting to note that the Ag-CU sample sees its resonance red-shifted and broadened by larger amounts compared to the resonance of unassembled Ag-CU nanoparticles when they are in solution ($\lambda'_{Ag\text{-}CU}$ = 412 nm, $\Delta\lambda'_{Ag\text{-}CU} \sim \Delta\lambda_{Ag\text{-}CU}/2.5$ = 116 nm). Such significant changes of the resonance properties come from the strong inter-particle coupling which is large due to the random close-packing of the nanocubes in the OMM. At the same time, the Ag-CS sample has its resonance at exactly the same position as that of individual nanoparticles and the broadening of the resonance induced by inter-particle interactions is relatively small ($\lambda'_{Ag\text{-}CU} = \lambda_{Ag\text{-}CU}$, $\Delta\lambda_{Ag\text{-}CU} \sim \Delta\lambda_{Ag\text{-}CS}/1.5$ = 107 nm). This can be explained by the fact that, contrary to the Ag-CU samples, the inter-particle coupling in core-shell OMMs is weak due to the presence of a sizable silica shell which has a thickness almost equal to the silver core radius and keeps the silver cores apart. The gold samples exhibit similar behavior. These observations suggest a relatively simple way in which, by controlling particle sizes and inter-particle separation, it is possible to engineer the dispersion of an OMM. The core-shell samples have a refractive index which rises rapidly from $n_{Ag\text{-}CS}$ = 1.2 to $n_{Ag\text{-}CS}$ = 1.6 in the 400-500 nm band for Ag-CSs and from $n_{Au\text{-}CS}$ = 1.5 to $n_{Au\text{-}CS}$ = 1.66 in the 500-600 nm band for the Au-CSs. For higher wavelengths, the value of n ~ 1.6 is maintained across the rest of the visible spectrum and well toward infrared wavelengths, while the absorption slowly decreases reaching impressively low values (e.g. $k_{Au\text{-}CS}$ ~ 0.02). The Ag-CU and Au-SP samples present a similar evolution except that the refractive index n rises across the visible spectrum from low values (0.5 and 1.3 respectively) to very large values (3.7 and 3 respectively) at 700 nm with decreasing absorption above 650 nm well into the IR.

Table 1. OMM Parameters fitted by the spectroscopic model. (Frequencies are given in eV)

Param.	Ag Cubes	Ag Core-Shells	Au Spheres	Au Core-Shells
ε_∞	2.3	1.44	2.18	1.90
N° of LOs	2	2	1	1
(f_j, ω_{0j}, γ_j)	(5.5, 1.88, 0.56) (0.53, 2.89, 1.2)	(0.36, 2.73, 0.49) (0.17, 2.0, 1.12)	(0.23, 2.3, 0.51)	(0.64, 6.19, 5.78)
TLO	No	Yes	Yes	Yes
(E_g, A, E, C)	–	(3.58, 300, 2.41, 0.9)	(1.67, 11.24, 4, 6.23)	(1.56, 4.24, 2.23, 0.43)

5. Conclusion

The combination of nanochemical engineering and microfluidic self-assembly enables us to obtain homogeneous optical metamaterials with a high degree of bulkiness exceeding the state-of-the-art realizations by at least one order of magnitude. Our fabrication technique enables a rapid and easy characterization using spectroscopic ellipsometry and allows one to make optical devices, such as lenses, filters, modulators using suitable thin plastic molds and filling them with nanoparticles. We obtain OMMs that reach high refractive index and low absorption in the deep red and the near-IR. We foresee that the combination of these two techniques will considerably reduce the complexity in the experimental investigations of bulk optical metamaterials, notably in the quest for optical magnetism. This leaves nanochemical synthesis and nanoparticle design at the heart of the study of three-dimensional OMMs.

Acknowledgements

This work was supported by the European FP7 project METACHEM under grant #228762. A. Baron acknowledges the AMADEUS Labex for financial support.

Chapter 6

Conclusion

The bottom-up fabrication of materials made of NPs is currently an active field of research. It is due to the advanced properties these NPs have and also because of forseen applications which result from the collective behavior of NPs. In the case of metamaterials, the constraints for making such composite materials are high: if one targets the visible range, one must incoporate two sets of small NPs (< 100 nm typically) which control the permittivity and the permeability, although controlling the two at the same time seems also possible. Fabricating these NPs is complex. Then, assembling them into a designed structure is also a challenge. The ordering of the particles seems important but disorder in metamaterials is actively debated at the moment, and the concentration of NPs must be high enough to boost the expected effects.

In this work, we used a bottom-up fabrication technique which relies on microfluidic evaporation. The technique permits us to extract the solvent of a dispersion in a very gentle and controlled way. This technique has been used before in order to concentrate surfactant molecules, polymers, etc., and to study their phase diagram. Only recently has it been used to build materials, first with large colloids ($1\,\mu$m) and then with NPs (J. Angly PhD's work also in the frame of METACHEM). It was shown that polymer-based NPs could be concentrated into dense materials.

Here, I extended this work for silica-coated NPs. In order to better quantify the concentration process, I developed a setup for on-chip visible spectroscopy. I quantified the range of absorbance we can measure on chip and also the spatial resolution of the setup: in some favorable cases, we can reach a spot size of about $5\,\mu$m. We could not measure the absorbance spectra of the materials we fabricated because even if they are thin, they absorb so much that we overcome the capability of our setup. However, we used the setup to follow in space and time the concentration field of NPs in the dilute state during the concentration process. We evidenced that precipitation often occurs and prevents the growth of solids. With a systematic analysis, we evidenced that the concentration of the particle in the stock solution is a key parameter, and when they get too dilute, precipitation always takes place. We hypothesized that this is due to ionic impurities that are present in the solution, and even traces of them become important when the number of NPs is too small. With a simple model of simultaneous concentration of NPs and salt, we built a stability

criterion which tells us when it is possible to bypass precipitation.

When the criterion is fullfilled, we can construct several types of materials. They are all characterized by a very high concentration of NPs (volume fraction $\sim 0.4 - 0.6$) and little long range order. We managed to extract these materials and to look at them with X-Rays and electron microscopy. We also managed to perform an ellipsometric characterization and the materials have a very different refractive index depending on the amount of metal inside the structure. These materials are real metamaterials as it is possible to engineer the permittivity with the composition of the material and to get negative values of ϵ. This is the first step toward of full control of the refractive index, and making it negative now requires the control of μ. We showed in this work that it is possible to assemble raspberry-like NPs into a dense solid and we had to imagine a new microfluidic technique to do so (raspberries are very dilute in general): the microfiltration, which is little sensitive to the stability criterion defined above. We have not yet measured the refractive index of the corresponding materials but we hope that the present work will help make it possible soon.

Bibliography

[1] S. Mann. Self-assembly and transformation of hybrid nano-objects and nanostructures under equilibrium and non-equilibrium conditions. *Nat. Mater.*, 8(10):781–792, 2009.

[2] V. G. Veselago. The electrodynamics of substances with simultaneously negative values of ϵ and μ. *Soviet Phys. Uspekhi*, 10:509, 1968.

[3] J. B. Pendry, A. J. Holden, D. J. Robbins, and W. J. Stewart. Magnetism from conductors and enhanced nonlinear phenomena. *IEEE Trans. Microwave Theory Tech.*, 47:2075, 1999.

[4] J. B. Pendry. Negative refraction makes a perfect lens. *Phys. Rev. Lett.*, 85:3966, 2000.

[5] D. R. Smith, Willie J. Padilla, D. C. Vier, S. C. Nemat-Nasser, and S. Schultz. Composite medium with simultaneously negative permeability and permittivity. *Phys. Rev. Lett.*, 84:4184, 2000.

[6] A. Alù, A. Salandrino, and N. Engheta. Nagtive effective permeability and left-handed materials at optical frequencies. *Opt. Exp.*, 14:1557, 2006.

[7] C. R. Simovski and S. A. Tretyakov. Model of isotropic resonant magnetism in the visible range based on core-shell clusters. *Phys. Rev. B*, 79:045111, 2009.

[8] S. Muehlig, A. Cunningham, S. Scheeler, C. Pacholski, T. Buergi, C. Rockstuhl, and F. Lederer. Self-assembled plasmonic core-shell clusters with an isotropic magnetic dipole response in the visible range. *ACS Nano*, 5(8):6586–6592, 2011.

[9] S. N. Sheikholeslami, H. Alaeian, A. L. Koh, and J. A. Dionne. A metafluid exhibiting strong optical magnetism. *Nano Lett.*, 13:4137, 2013.

[10] J. Leng, B. Lonetti, P. Tabeling, M. Joanicot, and A. Ajdari. Microevaporators for kinetic exploration of phase diagrams. *Phys. Rev. Lett.*, 96:084503, 2006.

[11] E. Favre, P. Schaetzel, Q. T. Nguygen, R. Clï£¡ment, and J. Nï£¡el. Sorption, diffusion and vapour permeation of various penetrants through dense poly(dimethylsiloxane membranes : a transport analysis. *Journal of membranes science*, 92:169, 1994.

[12] J.M. Watson and M.G. Baron. The behaviour of water in poly(dimethylsiloxane). *Journal of Membrane Science*, 110: 47–57, 1995.

[13] E. Verneuil, A. Buguin, and P. Silberzan. Permeation-induced flows: Consequences for silicone-based microfluidics. *Europhys. Lett.*, 68:412, 2004.

[14] G. C. Randall and P. S. Doyle. Permeation-driven flow in poly(dimethylsiloxane) microfluidic devices. *Proc. Natl. Acad. Sci. USA*, 102:10813, 2005.

[15] S.R. Quake and A. Scherer. From micro- to nanofabrication with soft materials. *Science*, 290(5496): 1536–1540, 2000.

[16] J. Goulpeau, D. Trouchet, A. Ajdari, and P. Tabeling. Experimental study and modeling of polydimethylsiloxane peristaltic micropumps. *Journal of Applied Physics*, 98: 044914, 2005.

[17] P. Moreau, J. Dehmoune, J.-B. Salmon, and J. Leng. Microevaporators with accumulators for the screening of phase diagrams of aqueous solutions. *Appl. Phys. Lett.*, 95:033108, 2009.

[18] L. Daubersies and J.-B. Salmon. Evaporation of solutions and colloidal dispersions in confined droplets. *Phys. Rev. E*, 84:031406, 2011.

[19] J. Leng, M. Joanicot, and A. Ajdari. Microfluidic exploration of the phase diagram of a surfactant/water binary system. *Langmuir*, 23:2315, 2007.

[20] A. Merlin, J.-B. Salmon, and J. Leng. Microfluidic-assisted growth of colloidal crystals. *Soft Matter*, 8:3526, 2012.

[21] A. Merlin, J. Angly, L. Daubersies, C. Madeira, S. Schöder, J. Leng, and J.-B. Salmon. Time-resolved microfocused small-angle x-ray scattering investigation of the microfluidic concentration of charged nanoparticles. *Eur. Phys. J. E*, 34:58, 2011.

[22] J.-B. Salmon and J. Leng. Application of microevaporators to dynamic exploration of the phase diagram. *J. Appl. Phys.*, 107:084905, 2010.

[23] M. Schindler and A. Ajdari. Modeling phase behavior for quantifying micropervaporation experiments. *Eur. Phys. J E*, 28:27, 2009.

[24] A. Merlin. Cinétiques de concentration de suspensions colloidales par évaporation microfluidique : de la solution diluée aux cristaux colloidaux. *Thèse de l'université Bordeaux-1*, 2010.

[25] J. C. Mcdonald and G. M. Whitesides. Poly(dimethylsiloxane) as a material for fabricating microfluidic devices. *Accounts of chemical research*, 35:491, 2002.

[26] M. A. Unger, H. P. Chou, T. Thorsen, A. Scherer, and S. R. Quake. Monolithic microfabricated valves and pumps by multilayer soft lithography. *Science*, 288:113, 2000.

[27] G. Cristobal, L. Arbouet, F. Sarrazin, D. Talaga, J.-L. Bruneel, M. Joanicot, and L. Servant. On-line laser raman spectroscopic probing of droplets engineered in microfluidic devices. *Lab Chip*, 6:1140, 2006.

[28] F. Sarrazin, J.-B. Salmon, D. Talaga, and L. Servant. Chemical reaction imaging within microfluidic devices using confocal raman spectroscopy: the case of water and deuterium oxide as a model system. *Anal. Chem.*, 80:1689, 2008.

[29] R. Barrett, M. Faucon, J. Lopez, G. Cristobal, F. Destremaut, A. Dodge, P. Guillot, P. Laval, C. Masselon, and J.-B. Salmon. X-ray microfocussing combined with microfluidics for on-chip x-ray scattering measurements. *Lab Chip*, 6:494, 2006.

[30] P. Massé, S. Mornet, E. Duguet, M. Tréguer-Delapierre, S. Ravaine, A. Iazzolino, J.-B. Salmon, and J. Leng. Synthesis of size-monodisperse spherical ag@sio2 nanoparticles and 3-d assembly assisted by microfluidics. *Langmuir*, 29:1790, 2013.

[31] K. L. Kelly, E. Coronado, L. L. Zhao, and G. C. Schatz. The optical properties of metal nanoparticles: The influence of size, shape, and dielectric environment. *J. Phys. Chem. B*, 107:668, 2003.

[32] J. Angly, A. Iazzolino, J. B. Salmon, J. Leng, S. P. Chandran, V. Ponsinet, A. Desert, Beulze A. Le, S. Mornet, M. Tréguer-Delapierre, and M. A. Correa-Duarte. Microfluidic-induced growth and shape-up of three-dimensional extended arrays of densely packed nanoparticles. *ACS Nano*, 7:6465, 2013.

[33] W. B. Russel, D. A. Saville, and W. R. Schowalter. *Colloidal dispersions*. Cambridge University Press, 1989.

[34] F. Clément and J. Leng. Evaporation of liquids and solutions in confined geometry. *Langmuir*, 20:6538, 2004.

[35] R. D. Deegan, M. Balkanski, T. F. Dupont, G. Huber, S. R. Nagel, and T. Witten. Capillary flow as the cause of ring stains fromdried liquid drops. *Nature*, 389:827, 1997.

[36] L. Goehring, W. J. Clegg, and A. F. Routh. Solidification and ordering during directional drying of a colloidal dispersion. *Langmuir*, 26:9269, 2010.

[37] J. Vieaud. *Propriétés optiques effectives de films composites de polymère et de nanoparticules d'or*. PhD thesis, Université de Bordeaux, 2011.

[38] Mikhail A. Kats, Romain Blanchard, Patrice Genevet, and Federico Capasso. Nanometre optical coatings based on strong interference effects in highly absorbing media. *Nat. Mater.*, 12(1):20–24, 2013.

[39] G. A. Ozin, A. C. Arsenault, and L. Cademartiri. *Nanochemistry: a chemical approach to nanomaterials*. RSC Publishing, Cambridge, 2009.

Résumés/Abstracts

1. Microevaporation (keywords:microfluidics, evaporation, lab on-chip)
2. On-chip microspectroscopy (keywords:spectroscopy,microfluidics chip, experimental setup)
3. Role of colloidal stability in the growth of micromaterials (keywords:micromaterials, colloidal stability,Nanoparticles)
4. Microfluidic-induced growth and shape-up of three-dimensional extended arrays of densely packed nano particles(growth of material, experimental data,3d materials)
5. Bulk metamaterials assembled by microfluidic evapration (keywords:ellipsometry, refraction index, metamaterials)

1. La Microevaporation (mots clés:microlfluidique, evaporation, puce microfluidique)
2. Microspectroscopie sur puce microfluidique (mot clés:spectroscopie, puce microfluidique, dispositif expérimental)
3. Le rôle de la stabilité colloïdal dans le croissance de matériaux (mot clés:micromateriaux, stabilité colloïdal,Nanoparticules)
4. Etude de la croissance de matériaux 3d constitue par nanoparticules grâce a la microfluidique (mot clés:croissance de materiaux,donne expérimental, matériaux 3d)
5. Metamateriaux 3d assemblée par une technique microfluidique (mot clés: ellipsometrie, indice de réfraction, metamateriaux)

1 Microevaporation

Microfluidics is the branch of fluid mechanics dedicated to the study of flows in the channel with dimensions between 1 micron and 100 micron. The object of this chapter is to illustrate the basic principles and possible applications of microfluidic chip, called microevaporator. In the first part of the chapter, we present a detailed description of the physics of microevaporators using analytical arguments, and describe some applications. In the second part of the chapter, we present the experimental protocol of engineering of micro evaporator and different type of microfluidics device.

2 On-chip microspectroscopy

The object of this chapter is to illustrate a method to measure absorption spectra during the process of growth of our materials in our microfluidic tools. The aim is to make an optical characterization of our micro materials and to carry-out a spatio-temporal study of kinetic properties of our dispersion under study. This instrumental chapter presents the theoretical basis of the method we used.

3 Role of colloidal stability in the growth of micromaterials

We used combined microspectroscopy and videomicroscopy to follow the nucleation and growth of materials made of core-shell Ag@SiO2 NPs in micro evaporators.
We evidence that the growth is actually not always possible, and instead precipitation may occur during the concentration process. This event is governed by the concentration of dispersion in the reservoir and we assume that its origin come from ionic species that are concentrated all together with the NPs and may alter the colloidal stability en route towards high concentration.

4 Microfluidic-induced growth and shape-up of three-dimensional extended arrays of densely packed nano particles

In this chapter I present in details microfluidic evaporation experiments to engineer various densely packed 3D arrays of NPs.

5 Bulk metamaterials assembled by microfluidic evaporation

In this chapter I introduced the technique we used (microspot ellipsometry) in close collaborations with V.Kravets and A.Grigorenko(University of Manchester) and with A.Aradian, P.Barois, A.Baron, K.Ehrhardt(CRPP, Pessac) to characterized the solids made of densely packed NPs. I describe the constraints that emerge from the coupling between the small size of our materials and the optical requirements, the analysis and interpretation of the ellipsometry experiments show that for the material with high volume fraction of metal exists the strong electrical coupling between the NPs and the materials display an extremely high refraction index in the near infra-red regime.

1 La Microevaporation

La microfluidique est la branche de la mécanique des fluides dédiés à l'étude des flux dans des canaux de dimensions comprises entre 1 micron et 100 microns. L'objet de ce chapitre est d'illustrer les principes de base et les applications possibles de une puce microfluidique, appelés microevaporator. Dans la première partie de ce chapitre, nous présentons une description détaillée de la physique des microevaporators en utilisant des arguments analytiques, et décrivons certaines applications. Dans la deuxième partie de ce chapitre, nous présentons le protocole expérimental de fabrication de un microévaporateur et différents design des dispositifs microfluidic.

2 Microspectroscopie sur puce microfluidique

L'objet de ce chapitre est d'illustrer une méthode pour mesurer les spectres d'absorption au cours du processus de croissance de nos matériaux dans nos outils microfluidiques. L'objectif est de faire une caractérisation optique de nos micro matériaux et de réaliser-une étude spatio-temporelle des propriétés cinétiques de notre dispersion. Ce chapitre présente la base théorique de la méthode expérimental utilisée.

3 Le role de la stabilité colloïdal dans le croissance de matériaux

Nous avons utilisé la microspectroscopie combinée avec la vidéomicroscopie pour suivre la nucléation et la croissance de matériaux à base de nanoparticules Ag@SiO2 dans les micro évaporateurs.
Nous mettons en évidence que la croissance est en fait pas toujours possible, et la précipitations de notre dispersion peuvent se produire pendant le processus de concentration. Cet événement est régi par la concentration de la dispersion dans le réservoir et nous supposons que son origine provient des espèces ioniques qui sont concentrés tous ensemble avec les NPs et peuvent altérer la stabilité colloïdale pour la haute concentration.

4 Etude de la croissance de matériaux 3d constitue par nanoparticules grâce a la microfluidique

Dans ce chapitre, je présente en détail les expériences d'évaporation microfluidiques pour concevoir différents matériaux 3D denses a base de NPs.

5 Characterization de metamateriaux 3d assemblée par une technique microfluidique

Dans ce chapitre, j'ai présenté la technique que nous avons utilisé (microspot ellipsométrie) dans des collaborations étroites avec V.Kravets et A.Grigorenko (Université de Manchester) et A.Aradian, P.Barois, A.Baron, K.Ehrhardt (CRPP, Pessac) pour caractériser les solides a base de NPs. Je décris les contraintes qui émergent du couplage entre la petite taille de nos matériaux et les exigences optiques, l'analyse et l'interprétation des expériences d'ellipsométrie montrent que pour le matériau avec une fraction volumique élevée de métal existe le couplage électrique forte entre les NPs et le matériaux présentent un indice de réfraction extrêmement élevé dans le régime de proche infrarouge.